

**Numerical investigations of contaminant transport  
in permeable rocks: examining the effects of  
discrete flow features in density-dependent and  
density-independent systems**

Megan Louise Sebben  
BSc. Env. Sci. (Hons), Dip. Lang.

School of the Environment  
Faculty of Science and Engineering  
Flinders University

A thesis submitted for the degree of  
*Doctor of Philosophy*  
April, 2016



## **Declaration**

I certify that this thesis does not incorporate without acknowledgment any material previously submitted for a degree or diploma in any other university; and that to the best of my knowledge and belief it does not contain any material previously published or written by another person except where due reference is made in the text.

.....

Megan Sebben

## **Acknowledgements**

I wish to acknowledge my principal supervisor, Professor Adrian Werner, for his scientific guidance and support throughout all aspects of this work. His passion, knowledge and enthusiasm for hydrogeology have been gratefully appreciated. It has been a pleasure working with you.

I would like to thank my Co-Supervisor, Professor Craig Simmons, as well as the National Centre for Groundwater Research and Training (NCGRT), Flinders University, and the Goyder Institute for Water Research for their financial and administrative support. Without this, the work presented here would not have been possible.

My sincere gratitude goes to Professor Thomas Graf for hosting me for 3 months at Leibniz University. The HGS modelling skills I obtained during this time were invaluable. In particular, I wish to thank Katharina Vujević, Jie Yang, and Eugenia Hirthe for their assistance with the model. I am also grateful to Carlos, Jan, Clemens, Alina, Vincent, Daniel and Leo for being part of this invaluable experience.

Many thanks go to Dr Daniel Partington, Dr Perry de Louw and Dr Neville Robinson for their technical support and insightful scientific discussions.

I wish to acknowledge my Flinders University/NCGRT colleagues and office mates (Matt, Cameron, Dan and Michelle) for making the experience an enjoyable one. In particular, I am grateful to Matthew Knowling, for sharing the Ph. D. experience.

My heartfelt thanks go to my family and friends for their ongoing support and encouragement.

## Summary

Discrete flow features (DFFs; e.g. fractures, faults, clay layers) are geological discontinuities of higher or lower permeability than the host rock that are of sufficient extent to impact groundwater flow. DFFs can provide preferential flow pathways (i.e. ‘preferential flow features’ (PFFs), wherein the permeability of the DFF is higher than the matrix), or flow barriers (i.e. ‘barrier flow features’ (BFFs), wherein the permeability of the DFF is lower than the matrix). The study of DFFs has thus far focussed on PFFs in low-permeability rock settings (e.g. granite, basalt), in which the majority of groundwater flow occurs within the PFF. There has been little research into the impact of both PFFs and BFFs on contaminant plume migration in otherwise permeable rocks (e.g. sandstone, limestone), despite that DFFs are widespread in high-yielding, permeable rock aquifers. The aim of this thesis is to examine within a modelling framework how DFFs influence the displacement and spreading of solute plumes, and the accompanying patterns of groundwater discharge, in idealised permeable rock aquifers.

Firstly, the influence of PFFs is investigated in a complex groundwater setting, to evaluate whether PFFs impact solute transport within commonly encountered situations involving seawater-freshwater mixing, such as those found in most coastal aquifers. Aquifers containing single fractures or regularly spaced discrete fracture networks (DFNs) are examined using modified forms of the Henry (1964) seawater intrusion (SWI) benchmark problem. The applicability of equivalent porous media (EPM) models for representing simple DFNs in SWI simulations is also tested. This study demonstrates that fracture effects on SWI are likely to be

mixed, ranging from enhancement to reduction in seawater extent and the width of the mixing zone, depending on such factors as PFF location, orientation and density. EPM models are shown to be inadequate for inferring salinity distributions unless the density of orthogonal fractures is high and appropriate dispersivity values can be determined.

While the study of SWI showed macro-scale plume behaviour, the role of individual PFFs on solute transport was uninterpretable under the complex density-dependent conditions of the Henry problem. Therefore, numerical investigations of solute plumes passing through an individual PFF are performed under simpler conditions, to explore the local-scale PFF effects on plume migration. The numerical modelling results show that individual-PFF impacts on plume displacement and spreading can be considerable. The attenuation of plumes is likely governed by PFFs rather than flow through the matrix, given that a single PFF (representing a medium-sized fracture) produces the equivalent spreading effects of 0.22-7.88 m of plume movement through the matrix only.

Finally, the previous analysis is extended by accounting for DFFs as 2D flow features, and by including BFF situations. A simple analytical expression and numerical modelling are employed to quantify the displacement and spreading of a solute plume as it passes through a DFF. The results demonstrate that the attenuating influence of PFFs in permeable rocks is greater than for BFFs, and that PFFs are likely to have a more significant influence on plume distributions. DFF effects on plumes generally increase with increasing aperture.

## Table of Contents

Declaration .....	i
Acknowledgements .....	ii
Summary .....	iii
Table of Contents .....	v
List of Figures .....	x
List of Tables.....	xiv
1. Introduction .....	1
2. Seawater intrusion in fractured coastal aquifers: A preliminary numerical investigation using a fractured Henry problem .....	5
2.1 Abstract.....	5
2.2 Introduction .....	7
2.3 Methodology.....	12
2.3.1 Previous modelling approaches.....	12
2.3.2 Conceptual model.....	13
2.3.3 Numerical model .....	17
2.3.4 Fractured aquifer cases: Modified Henry problem.....	18
2.3.5 Fractured aquifer cases: Field-scale settings .....	23
2.4 Results .....	25
2.4.1 Single vertical fracture (Case A).....	28
2.4.2 Single horizontal fracture (Case B).....	30
2.4.3 Orthogonal fracture networks (Case C).....	34
2.4.4 Inclined fracture networks (Cases D and E).....	38
2.4.5 Field-scale settings .....	42
2.5 Discussion.....	45
2.6 Conclusions .....	50

3. A modelling investigation of solute transport in permeable porous media containing a discrete preferential flow feature .....	53
3.1 Abstract.....	53
3.2 Introduction .....	54
3.3 Methodology.....	59
3.3.1 Conceptual model.....	59
3.3.2 Numerical model .....	62
3.3.3 Fractured aquifer scenarios .....	64
3.4 Results .....	66
3.4.1 Visual inspection of PFF effects on solute plumes .....	66
3.4.2 Quantification of PFF effects on solute plume characteristics below the PFF .....	75
3.4.3 Quantification of PFF effects on solute plume characteristics above the PFF .....	80
3.5 Discussion.....	82
3.6 Conclusions .....	88
4. On the effects of preferential or barrier flow features on solute plumes in permeable porous media .....	91
4.1 Abstract.....	91
4.2 Introduction .....	92
4.3 Methodology.....	98
4.3.1 Flow line refraction through discrete flow features .....	98
4.3.2 Numerical investigation of dispersive effects on solute transport .	101
4.3.3 Back dispersion effects.....	109
4.4 Results .....	110
4.4.1 Analysis of flow line refraction through discrete flow features.....	110
4.4.2 2D effects of DFFs on solute transport .....	111

4.4.3. Back dispersion .....	129
4.5 Discussion.....	132
4.6 Conclusions .....	137
5. Conclusions .....	140
References .....	145
Declaration .....	i
Acknowledgements .....	ii
Summary .....	iii
Table of Contents .....	v
List of Figures .....	viii
List of Tables.....	xii
1. Introduction .....	1
2. Seawater intrusion in fractured coastal aquifers: A preliminary numerical investigation using a fractured Henry problem .....	5
2.1 Abstract.....	5
2.2 Introduction .....	7
2.3 Methodology.....	12
2.3.1 Previous modelling approaches.....	12
2.3.2 Conceptual model.....	14
2.3.3 Numerical model .....	17
2.3.4 Fractured aquifer cases: Modified Henry problem.....	18
2.3.5 Fractured aquifer cases: Field-scale settings .....	23
2.4 Results .....	25
2.4.1 Single vertical fracture (Case A) .....	28
2.4.2 Single horizontal fracture (Case B) .....	30
2.4.3 Orthogonal fracture networks (Case C).....	34
2.4.4 Inclined fracture networks (Cases D and E).....	38

2.4.5 Field-scale settings .....	42
2.5 Discussion.....	45
2.6 Conclusions .....	50
3. A modelling investigation of solute transport in permeable porous media containing a discrete preferential flow feature.....	53
3.1 Abstract.....	53
3.2 Introduction .....	54
3.3 Methodology.....	59
3.3.1 Conceptual model.....	59
3.3.2 Numerical model .....	62
3.3.3 Fractured aquifer scenarios .....	64
3.4 Results .....	66
3.4.1 Visual inspection of PFF effects on solute plumes .....	66
3.4.2 Quantification of PFF effects on solute plume characteristics below the PFF.....	75
3.4.3 Quantification of PFF effects on solute plume characteristics above the PFF.....	80
3.5 Discussion.....	82
3.6 Conclusions .....	88
4. On the effects of preferential or barrier flow features on solute plumes in permeable porous media .....	91
4.1 Abstract.....	91
4.2 Introduction .....	92
4.3 Methodology.....	98
4.3.1 Flow line refraction through discrete flow features .....	98
4.3.2 Numerical investigation of dispersive effects on solute transport .....	100
4.3.3 Back dispersion effects.....	108

4.4 Results .....	109
4.4.1 Analysis of flow line refraction through discrete flow features .....	109
4.4.2 2D effects of DFFs on solute transport.....	110
4.4.3. Back dispersion .....	127
4.5 Discussion.....	129
4.6 Conclusions .....	135
5. Conclusions .....	138
References .....	143

## List of Figures

Figure 2.1 Problem domain and boundary conditions. ....	14
Figure 2.2 Schematic description of the SWI comparison metrics: (a) the toe location, (b) the flux inflexion point, (c) the centre of mass (COM), and (d) the horizontal and vertical widths of the mixing zone (HMZ and VMZ, respectively). ....	17
Figure 2.3 Fracture network Cases A, B, C, D and E. The letter and number in the top right hand corner of each rectangle correspond to the fracture scenario (A-E) and fracture level (1-5).....	20
Figure 2.4 Steady-state salinity distributions in fractured aquifer Cases A, B, C, D and E. Case F represents the EPM results from corresponding scenarios in Cases D and E. Fractures are shown by white lines. ....	27
Figure 2.5 Influence of Case A fracture location on: (a) toe position, (b) flux inflexion location, (c) COM in the $x$ direction, (d) COM in the $z$ direction, and (e) and (f) mixing zone widths.....	29
Figure 2.6 Influence of Case B fracture location on: (a) toe position, (b) flux inflexion location, (c) COM in the $x$ direction, (d) COM in the $z$ direction, and (e) and (f) mixing zone widths.....	31
Figure 2.7 Distribution of equivalent freshwater hydraulic heads at 0.005 m intervals in Case B.....	33
Figure 2.8 Concentrations relative to seawater (colours), equivalent freshwater hydraulic head contours (black lines), and the direction of velocity vectors (white arrows) for Scenarios B1 and B3. ....	33
Figure 2.9 Influence of Case C fracture spacing on: (a) toe position, (b) flux inflexion location, (c) COM in the $x$ direction, (d) COM in the $z$ direction, and (e) and (f) mixing zone widths.....	35
Figure 2.10 Concentrations relative to seawater (colours), equivalent freshwater hydraulic head contours (black lines), and the direction of velocity vectors (white arrows) for Scenarios C1 and C2. ....	37
Figure 2.11 Scenario C4 relative seawater concentrations (coloured bands). The width of the mixing zone is shown for the Case C EPM (white lines) and Case C EPM with modified transverse and longitudinal dispersivities (black solid and black dashed lines). ....	38

Figure 2.12 Influence of 45° (Case D) and 135° (Case E) fracture inclination and spacing on: (a) toe position, (b) flux inflexion location, (c) COM in the $x$ direction, (d) COM in the $z$ direction, and (e) and (f) mixing zone widths.....	40
Figure 2.13 Distributions of equivalent freshwater hydraulic heads in Cases D2, D5, E2 and E5, and their respective EPMs. ....	42
Figure 2.14 Steady-state salinity distributions in: (a), (c), (e), (g), (i) the field-scale DFN models, and (b), (d), (f), (h), (j) the field-scale EPM models (Cases 1-5, respectively). Fractures are shown by white lines.....	43
Figure 2.15 Influence of Case 1 orthogonal fractures on: (a) toe position, (b) flux inflexion location, (c) COM in the $x$ direction, (d) COM in the $z$ direction, and (e) and (f) mixing zone widths.....	44
Figure 3.1 Conceptual model of the DFN cases, where $H$ is hydraulic head and $f'_m$ is contaminant mass flux. ....	61
Figure 3.2 Schematic description of the peak solute concentration displacement, $D$ . The solid black arrow represents the main plume trajectory in the PMO models. The black dashed arrow represents the plume trajectory at the maximum solute concentration beneath the PFF in the DFN model.....	62
Figure 3.3 Schematic description of the solute plume comparison metrics in: (a) the PMO model, and (b) the DFN model (shown for Scenario A1). Colours represent the solute concentrations. White arrows show the direction of velocity vectors. Black dashed arrows indicate the width of the solute plume. Black crosses highlight the location of maximum solute concentration immediately beneath the PFF. The PFF is shown by the white line.....	67
Figure 3.4 Steady-state salinity distributions in DFN Cases A, B, C, D, E and F. PFFs are shown by white lines. ....	69
Figure 3.5 Comparison of solute concentrations immediately beneath the PFF in the DFN models ( $C_{DFN}$ ) and PMO models ( $C_{PMO}$ ), for all Cases A to F. The 1:1 lines of equality between $C_{DFN}$ and $C_{PMO}$ are shown by the solid black lines. Squares above (below) the 1:1 line indicate that the PFF has caused an increase (decrease) in solute concentration compared to the PMO model.....	71
Figure 3.6 Influence of $K_m/K_f$ on: (a) $D$ , (b) $C_{Dmax}/C_{Pmax}$ below the PFF, (c) $W_{DFN}/W_{PMO}$ , and (d) $W_L/W_R$ , for Cases A to E. ....	76

Figure 3.7 Scenario A2 ( $K_m/K_f = 2.5 \times 10^{-2}$ ) solute concentrations above the PFF in the PMO model (solid black lines) and DFN model (dashed black lines). Solute concentrations are obtained at: (a)  $z = 51.250$  cm, (b)  $z = 50.625$  cm, (c)  $z = 50.413$  cm, and (d)  $z = 50.025$  cm. .... 81

Figure 3.8 Equivalent length of porous media required to reproduce the solute plume widths in Cases A ( $K_m/K_f = 2.5 \times 10^{-2}$ ), B ( $K_m/K_f = 4.9 \times 10^{-3}$ ) and C ( $K_m/K_f = 2.4 \times 10^{-3}$ ). .... 86

Figure 4.1 Schematic description of the flow line displacement,  $D_{PT}$ . The solid black line represents the groundwater flow trajectory without a DFF. The dashed lines represent the flow line trajectory after refraction at interfaces between the matrix and DFF. .... 99

Figure 4.2 Comparison of solute distributions involving a plume passing through a PFF that is oblique ( $45^\circ$ ) to the groundwater flow direction. PFFs are incorporated in models using the DFN approach (a, c, e) or as a porous media layer (b, d, f). The solid white line in the DFN models represents the discrete PFF.  $2b$  is 0.25 mm in (a) and (b) and 0.5 mm in (c) to (f). The  $K_m/K_f$  ratios for each case are: (a) and (b)  $2.0 \times 10^{-4}$ ; (c) and (d)  $2.4 \times 10^{-3}$ , and (e) and (f)  $2.5 \times 10^{-2}$ . .... 104

Figure 4.3 Conceptual model of a permeable rock matrix containing a DFF (not to scale), where  $H$  is hydraulic head and  $f'_m$  is contaminant mass flux. Adapted from Sebben and Werner (2016). .... 105

Figure 4.4 Schematic description of the solute plume comparison metrics in: (a) the MO model, and (b) the DFF model. Colours represent the solute concentrations. White arrows show the direction of velocity vectors. Black dashed arrows indicate the width of the solute plume. Black crosses highlight the location of maximum solute concentration immediately beneath the DFF. .... 107

Figure 4.5 Schematic description of the displacement of peak solute concentration,  $D_{NM}$ . The solid black line represents the groundwater flow trajectory without a DFF.  $C_{MO}$  is the peak solute concentration without a DFF and  $C_{DFF}$  is the peak solute concentration beneath the DFF.  $D_H$  indicates the horizontal distance between the  $x$ -location of  $C_{MO}$  and  $C_{DFF}$ . .... 108

Figure 4.6 Steady-state salinity distributions for PFF Cases A ( $K_m/K_f = 0.01$ ), B ( $K_m/K_f = 0.1$ ) and C ( $K_m/K_f = 0.5$ ). .... 113

Figure 4.7 Influence of  $K_m/K_f$  (cases) and  $2b$  (scenarios) on  $D_{NM}$  in PFF cases. 114

Figure 4.8 Comparisons of $D_{NM}$ and $D_{PT}$ for Cases A, B and C. Scenarios 1, 2, 3 and 4 are indicated by black, red, blue and green markers, respectively. Note that the marker for Scenario 1 is obscured by Scenario 2 in each case. The 1:1 line is illustrated in grey. ....	115
Figure 4.9 Influence of $K_m/K_f$ and $2b$ on: (a) $W_{PFF}/W_{MO}$ , (b) $W_L/W_R$ , and (c) $C_{PFF}/C_{MO}$ in PFF cases. ....	118
Figure 4.10 Steady-state salinity distributions for BFF Cases D ( $K_m/K_f = 2$ ), E ( $K_m/K_f = 10$ ) and F ( $K_m/K_f = 100$ ). ....	121
Figure 4.11 Steady-state solute plume for Scenario F4 ( $K_m/K_f = 100$ ). White arrows indicate flow direction. ....	122
Figure 4.12 Influence of $K_m/K_f$ (cases) and $2b$ (scenarios) on $D_{NM}$ in BFF cases. ....	123
Figure 4.13 Comparisons of $D_{NM}$ and $D_{PT}$ for Cases D, E and F. Scenarios 1, 2, 3 and 4 are indicated by black, red, blue and green markers, respectively. Note that the marker for Scenario 1 is obscured by Scenario 2 in Cases D and E. Markers are not illustrated for Scenarios F3 and F4 because $D_{NM}$ has been omitted. The 1:1 line is illustrated in grey. ....	125
Figure 4.14 Influence of $K_m/K_f$ and $2b$ on: (a) $W_{BFF}/W_{MO}$ , (b) $W_L/W_R$ , and (c) $C_{BFF}/C_{MO}$ in BFF cases. ....	127
Figure 4.15 Comparison of solute plume distributions with and without back dispersion in Cases A, B and C (Scenarios 3 and 4 only). Solute concentrations are compared along the top of the PFF in cases with back dispersion (black dashed line) and without back dispersion (solid black line). Solute concentrations in and beneath the PFFs in cases with no back dispersion are indicated by colours. ....	130
Figure 4.16 Schematic description of potential $ D_{PT} $ for solute plumes intercepting a DFF in a steady flow field oblique to the DFF (solid black and white dashed arrows). Dark blue shading indicates a PFF. Red shading indicates a BFF. Blue dashed arrows illustrate potential flow lines for PFF cases. Orange dashed arrows illustrate potential flow lines for BFF cases. Red arrows indicate the maximum $ D_{PT} $ . ....	132

## List of Tables

Table 2.1 Model parameters used in the fractured forms of the Henry problem. .	21
Table 2.2 Model parameters used in the fractured field-scale problems. ....	24
Table 3.1 Model parameters for Cases A to F.....	66
Table 3.2 Root-mean-square errors for solute concentrations beneath the PFF in the DFN models, relative to PMO model values. ....	75
Table 3.3 Solute plume metrics for Scenario C2 with varied PFF orientation. ....	80
Table 4.1 Simulation parameters for Cases A to F. ....	109
Table 4.2 Displacement due to flow line refraction in Cases A to F. ....	111
Table 4.3 Displacement of plume centre of mass for Cases A to F. ....	133

# Chapter 1

## 1. Introduction

Numerous problems of environmental concern (e.g. groundwater contamination, seawater intrusion) involve the transport of solutes in rocks containing discrete flow features (DFFs) such as fractures, faults, sand lenses and clay layers. DFFs can act as either preferential pathways (i.e. ‘preferential flow features’; PFFs) or barriers (i.e. ‘barrier flow features’; BFFs) to fluid flow and solute transport. DFFs are common geologic features in aquifers where the matrix permeability ranges from virtually impermeable (e.g. granite and basalt) to permeable (e.g. sandstone and limestone). Despite this, very little research attention has been given to the transport of solutes in permeable rock aquifers containing PFFs, compared to low-permeability rocks (Rubin et al., 1997; Odling and Roden, 1997). The influence of BFFs has been studied to an even lesser degree than PFFs.

Amongst the various forms of geologic heterogeneity, PFFs that accompany fractured and karst (i.e. PFFs formed by fractures, faults and/or conduits) coastal aquifers present as the most challenging to characterise (e.g. Berkowitz, 2002; Bakalowicz, 2005). Case studies of groundwater contamination from seawater intrusion (SWI) in fractured or karst coastal aquifers include Leve (1983), Bonacci and Roje-Bonacci (1997), and Arfib et al. (2007). Leve (1983) suggested that high chloride concentrations in the Floridan aquifer system likely indicated the presence of faults or fractures that facilitate the upward leakage of saline waters. Bonacci and Roje-Bonacci (1997) and Arfib et al. (2007) investigated the mechanisms of SWI through coastal springs, wherein both studies demonstrated that PFFs can influence

the distribution of seawater in coastal aquifers in comparison to the classical description of a ‘seawater wedge’ in a homogeneous porous medium. Despite this, the relationships between PFF characteristics (e.g. PFF location, orientation and spacing) and the distribution of seawater in coastal aquifers have not been investigated. Therefore, the first objective of this thesis is to explore within a modelling framework, what SWI might look like in coastal aquifers containing networks of discrete PFFs, for a variety of PFF geometries.

The transport of solutes in permeable rocks containing PFFs typically occurs via advection, mechanical dispersion and molecular diffusion in both the PFF and the rock matrix (Birkhölzer et al., 1993a). Previous studies of solute transport in permeable rocks containing PFFs generally consider formations that can be approximated using the equivalent porous media (EPM) approach, wherein individual PFFs are not represented explicitly in numerical models (e.g. Birkhölzer et al., 1993a; 1993b; Rubin and Buddemeier, 1996), or permeable rocks containing naturally occurring PFF geometries (e.g. Odling and Roden, 1997). As such, these studies do not provide insight into the effect of transport processes at the scale of an individual PFF, despite that these local-scale processes can have a dramatic influence on solute transport at larger scales (Grisak and Pickens, 1980). Therefore, the second objective of this thesis is to undertake quantitative analyses of solute plumes that pass through individual PFFs in permeable rocks, to numerically investigate the mechanisms that underlie solute plume behaviours observed in previous matrix-PFF studies.

In some cases, DFFs contain material that is less permeable than the rock matrix, and hence, form BFFs (e.g. Laubach, 2003; Bense and Person, 2006). Previous studies of permeable rocks containing BFFs have typically examined BFF effects on groundwater flow regimes rather than solute transport processes. Nonetheless, several studies of solute transport across BFFs (e.g. Johnson et al., 1989; Zhang and Qiu, 2010) have found that BFFs may not prevent contamination of underlying aquifers, and that the barrier's depth and hydraulic conductivity are likely the key controls on the extent of contaminant migration. However, like the PFFs discussed above, the small-scale solute transport processes at the matrix-BFF interface remain essentially unexplored. Therefore, the third objective of this thesis is to quantify the solute plume changes where BFFs are encountered in otherwise permeable rock aquifers.

In summary, numerical investigations that provide insight into the effects of DFFs on solute transport in permeable rocks (representative of sedimentary aquifers) are carried out. The general aims of this research project are to examine how DFFs influence the displacement and widening (or narrowing) of solute plumes in both density-dependent and density-independent systems.

This thesis consists of five chapters inclusive of the current chapter. Chapter 1 provides a brief background to the research project and summarises the contents of each chapter. Chapters 2, 3 and 4 are based on journal papers that are either published or in the publication process in international journals. A summary of the main conclusions from this research project is given in Chapter 5.

In Chapter 2, discrete fracture network (DFN) models are employed in a preliminary investigation of SWI in aquifers containing a single fracture (i.e. PFF) or networks of regularly spaced fractures. The objectives here are to explore the influence of fracture orientation, location and density on the extent of seawater and accompanying patterns of groundwater discharge in idealised coastal aquifers, and to test the applicability of equivalent porous media (EPM) models for representing simple fracture networks in steady-state simulations of SWI.

Chapter 3 presents a quantitative analysis of solute plumes that pass through a single PFF in permeable rock. Numerical simulations are conducted (using the DFN approach, where PFFs are treated as 1D flow features) to explore the PFF's influence on plume migration, for a variety of matrix-PFF permeability contrasts. The impact of PFFs on both the displacement and spreading of contaminant plumes in permeable rock matrices is ascertained through comparison with associated porous media only (PMO) models.

Chapter 4 extends the analysis presented in Chapter 3 by accounting for DFFs as 2D flow features, and including BFF situations. A simple analytical expression and numerical modelling are used to quantify how a single DFF influences the displacement and widening (or narrowing) of solute plumes in permeable rocks. A variety of matrix-DFF permeability contrasts and DFF apertures are considered. The potential role of 'back dispersion' on predictions of PFF effects on solute transport is also explored.

Chapter 5 presents the main conclusions of this thesis.

## Chapter 2

### 2. Seawater intrusion in fractured coastal aquifers: A preliminary numerical investigation using a fractured Henry problem

*This chapter is based on the following published paper:*

Sebben, M. L., Werner, A. D., Graf, T., 2015. Seawater intrusion in fractured coastal aquifers: A preliminary numerical investigation using a fractured Henry problem. *Adv. Water Resour.* 85, 93-108, doi: 10.1016/j.advwatres.2015.09.013.

#### 2.1 Abstract

Despite that fractured coastal aquifers are widespread, the influence of fracture characteristics on seawater intrusion (SWI) has not been explored in previous studies. This research uses numerical modelling in a first step towards understanding the influence of fracture orientation, location and density on the extent of seawater and accompanying patterns of groundwater discharge in an idealised coastal aquifer. Specifically, aquifers containing single fractures or networks of regularly spaced fractures are studied using modified forms of the Henry SWI benchmark problem. The applicability of equivalent porous media (EPM) models for representing simple fracture networks in steady-state simulations of SWI is tested. The results indicate that the influence of fractures on SWI is likely to be mixed, ranging from enhancement to reduction in seawater extent and the width of the mixing zone. For the conceptual models considered here, vertical fractures in contact with the seawater wedge increase the width of the mixing zone, whereas vertical fractures inland of the wedge have minimal impact on the seawater distribution. Horizontal fractures in the lower part of the aquifer force the wedge

seaward, whereas horizontal fractures located within the zone of freshwater discharge enhance the wedge. Inclined fractures roughly parallel to the seawater-freshwater interface increase the landward extent of seawater and fractures perpendicular to the interface inhibit the wedge. The results show that EPM models are likely inadequate for inferring salinity distributions in most of the fractured cases, although the EPM approach may be suitable for orthogonal fracture networks if fracture density is high and appropriate dispersivity values can be determined.

## 2.2 Introduction

Globally, coastal aquifers are under threat from seawater intrusion (SWI) (Chang and Yeh, 2010). SWI is caused by changes in coastal aquifer conditions resulting from groundwater extraction, climate drivers, sea-level rise, oceanic over-topping events, and land use change (Custodio and Bruggeman, 1987; Yang et al., 2013). Aquifer heterogeneities are also known to significantly influence the nature of SWI (e.g. Dagan and Zeitoun, 1998; Lu et al., 2013). Amongst the various forms of geologic heterogeneity, the preferential flow pathways accompanying fractured and karst coastal aquifers present as the most challenging to characterise (e.g. Berkowitz, 2002; Bakalowicz, 2005). Despite that fractured coastal aquifers are widespread and under increasing stress from extraction and development, the distribution of saltwater and the nature of SWI in fractured coastal systems remains poorly understood, particularly relative to unfractured aquifers (Werner et al., 2013).

In the absence of systematic studies of SWI in fractured rock settings, the findings from analyses of more generalised aquifer heterogeneity offer some preliminary insights into the expected role of fractures in coastal aquifers. Studies of random heterogeneity effects on SWI include the work of Dagan and Zeitoun (1998), Held et al. (2005), Kerrou and Renard (2010), and Lu et al. (2013). Dagan and Zeitoun (1998) examined the impact of horizontal layered heterogeneity on the shape of the seawater-freshwater interface and found that neglecting layered heterogeneity introduced large uncertainty in estimates of the seawater wedge toe position (i.e. the maximum inland extent of seawater). Their study assumed a sharp seawater-

freshwater interface and, as such, did not evaluate the effects of stratified heterogeneity on the width of the mixing zone. Lu et al. (2013) later considered the impact of stratigraphic layers on the width of the steady-state seawater-freshwater mixing zone. Changes in permeability across layer boundaries were found to cause refraction of seawater and the separation of streamlines, resulting in broad mixing zones in the low permeability layers. Conversely, higher permeability layers caused streamlines to converge and produce narrower mixing zones. Dagan and Zeitoun (1998) and Lu et al. (2013) assumed that heterogeneity exists in the form of horizontal layers, reflecting idealised geologic formations in stratified (e.g. sedimentary) coastal aquifers. The effect of high permeability fractures that span a range of orientations embedded within a porous matrix (e.g. fractures within an otherwise porous rock matrix) on the shape of the interface remains unexplored.

Held et al. (2005) employed homogenisation theory to examine upscaling of density-dependent flow in a heterogeneous version of the original (i.e. highly diffusive) Henry (1964) problem. They found that upscaled dispersivity coefficients were not necessary to reproduce SWI in a heterogeneous porous medium. However, Kerrou and Renard (2010) found that, in contradiction to Held et al. (2005), the increase in macrodispersion accompanying the upscaling process needed to be accounted for in a more realistic, dispersive form of the Henry (1964) problem. Their results demonstrated important differences between macrodispersion effects when upscaling SWI in dispersion-dominant versus diffusion-dominant problems. SWI in fractured settings is likely to differ from SWI in aquifers of random heterogeneity due to the high-permeability and low-porosity nature of fractures, and also fractures may act to either enhance fluid flow or form barriers to it (Odling and

Roden, 1997). Further, in fractured rock aquifers, molecular diffusion may dominate solute transport in the rock matrix if the matrix permeability (and hence, fluid velocity) is low, whereas transport within fractures is dominated by advection and dispersion (e.g. Tang et al., 1981; Zhou et al., 2007). Hence, the representation of dispersion in fractured-rock models is likely to influence prediction of SWI in more complex manners than that observed for cases of random heterogeneity.

Case studies of SWI in fractured aquifers include Leve (1983), Spechler (1994), Park et al. (2012) and Lim et al. (2013). Leve (1983) and Spechler (1994) studied the mechanisms of SWI leading to increased chloride concentrations in the karstified Floridan aquifer system. Both authors concluded that high chloride concentrations in the upper zones of the aquifer likely indicate the presence of faults or fractures that breach confining beds within the aquifer and thus enable the upward leakage of saline waters. Park et al. (2012) demonstrated, using flow meter tests, groundwater levels and electrical conductivity measurements, that the extent of SWI in a coastal fractured aquifer in Jeollanam-Do, Korea, is highly dependent on the presence of conductive fractures and their hydraulic connection to pumping wells and the sea. Geochemical and isotopic indicators were used by Lim et al. (2013) to show that SWI through fractured bedrock was contributing to the salinisation of seepage waters around an oil storage cavern in Yeosu, Korea. From these studies, it is clear that fractures can have a significant impact on the extent of SWI in coastal aquifers by providing preferential flow and transport pathways. Despite this, field studies and numerical investigations that explore relationships between fracture network characteristics and the distribution of seawater in coastal aquifers are absent from the literature. Therefore, understanding how the various

structural properties of fracture networks (e.g. fracture location, orientation and spacing) influence density-driven flow and transport processes accompanying the location and movement of seawater in coastal aquifers is of paramount importance (e.g. Allen et al., 2002; Allen et al., 2003).

While there are a lack of generalizable analyses of SWI in fractured systems, studies of top-down density-driven flow and transport in fractured rock, involving both free convection (i.e. caused by unstable density stratification) and mixed convection (i.e. free convection and advection) situations, provide useful insights. For example, Shikaze et al. (1998) numerically modelled solute plume migration under mixed convection in a low-permeability porous medium containing networks of continuous, orthogonal fractures. They found that fracture spacing was a key criterion for determining flow behaviour. Further, dense solute plumes were found to develop in highly complex patterns (relative to those observed in neutral-density simulations) in systems where free convection dominates the transport of solutes. Shikaze et al. (1998) concluded that limited knowledge of fracture characteristics in field settings likely precludes predictions of transport rates under free convection. It is yet to be demonstrated as to whether the capability to predict SWI in fractured systems is equally limited. Graf and Therrien (2005) simulated density-driven (free convective) flow and transport in a single 45°-inclined fracture, embedded in a low-permeability matrix. They demonstrated that free convection in the matrix controls the transport rate in an inclined fracture. Graf and Therrien (2007) later extended the work of Shikaze et al. (1998) by showing that density-driven plume migration is highly sensitive to the geometry of irregular fracture networks and their connectivity to the solute source. Vujević et al. (2014) examined the impact of

fracture network geometry on free convective flow patterns and found that free convection was controlled more so by the fracture network structure, rather than the bulk permeability of the system. Continuous fracture circuits were identified as the most important geometric feature for determining the vigour of free convection (i.e. the ratio between total solute mass flux and diffusive mass flux through a surface, defined by the dimensionless Sherwood number; Graf (2005)). These top-down studies of density-driven transport in fractured systems suggest that the porous matrix is expected to influence the shape of the seawater wedge, even for matrices of low permeability, as will the geometry of fracture networks, including the inter-connectivity between individual fractures.

The purpose of the current study is to explore within a simple modelling framework, what SWI might look like in fractured coastal aquifers. Specifically, the influence of fracture location, orientation and density on the inland extent of seawater will be examined for steady-state groundwater flow and solute transport conditions. A range of simplistic fracture network geometries are added to modified forms of the Henry (1964) SWI benchmark problem. The original Henry (1964) problem considers only highly diffusive solute transport in a homogeneous porous medium. Therefore, we produce variations of the problem that, following the recommendations of Abarca et al. (2007), are less diffusive and include dispersive solute transport, to better reflect real-world conditions. Further, we adopt aquifer properties that more closely represent consolidated geological materials (e.g. limestone, sandstone, dolomite, etc.) in which both preferential flow due to fractures and flow through the matrix are known to occur. These types of settings are chosen because they represent common high-yielding forms of fractured

aquifers. Fracture networks similar to those employed in the free convection analysis of Vujević et al. (2014) are adopted, because these provide a methodical framework for model testing. The simulations presented in this study are the first step towards understanding how the structural properties of fracture networks might control the extent of seawater in fractured aquifers.

## **2.3 Methodology**

### **2.3.1 Previous modelling approaches**

Groundwater flow and solute transport in fractured aquifers have been modelled previously using three alternative approaches: (1) equivalent porous medium (EPM) models, which consider a single continuum using surrogate aquifer properties (e.g. Scanlon et al., 2003); (2) dual-porosity models, which adopt two interacting continua, including the solid rock domain (primary porosity) represented by low permeability and high storage capacity, and the fracture domain (secondary porosity) with high permeability and negligible storage capacity (Barenblatt et al., 1960; e.g. Sudicky 1990); and (3) discrete fracture network (DFN) models, in which individual fractures are incorporated explicitly into an  $n$ -dimensional model as  $(n-1)$ -dimensional features (e.g. Smith and Schwartz, 1984).

Groundwater flow in fractured systems can be approximated adequately using the EPM (i.e. the most straightforward) approach if the representative elementary volume (REV) is large enough to approximate equivalent porous media (Pankow et al., 1986; Scanlon et al., 2003). Regional-scale EPM models have been employed successfully to simulate groundwater flow in fractured geologic media at risk of

SWI (e.g. Langevin, 2003; Giudici et al. 2012), and to quantify the impacts of sea-level rise and changes to groundwater recharge on the extent of SWI (Rasmussen et al., 2013). However, accurate simulation of transport processes, such as those associated with SWI, remains problematic in fractured systems due to difficulties in characterising geologic controls (e.g. fracture spacing and aperture) (Krásný and Sharp, 2007). DFN models have been used in several studies to simulate SWI in a relatively small number of discrete fractures (e.g. Masciopinto, 2006; Barcelona et al., 2006; Dokou and Karatzas, 2012). For example, Dokou and Karatzas (2012) produced a hybrid EPM-DFN model (i.e. a 3D EPM model of the porous matrix combined with a 2D DFN model of the main fracture networks) to examine SWI in a karst coastal aquifer in Crete, Greece. The authors established that the presence of previously unknown fractures was the likely cause of the extremely high chloride concentrations (up to 17,300 mg/L) measured at several observation wells. By modifying the fracture network, the authors were able to obtain an improved match to chloride observations. They concluded that the aquifer under investigation could not be described adequately using an EPM model. Thus, DFN models may be necessary to simulate the density-driven groundwater flow and transport processes accompanying SWI in fractured porous media with reasonable accuracy.

### **2.3.2 Conceptual model**

Fractured aquifer variations of the dispersive Henry (1964) SWI problem (Abarca et al., 2007) were employed in our analysis, using the DFN approach. Henry (1964) described SWI in a  $2 \text{ m} \times 1 \text{ m}$  2D cross section through a homogeneous, isotropic, confined aquifer. Transport in the original Henry (1964) problem occurs via

advection and exaggerated molecular diffusion, resulting in computed salinity isochlors that do not resemble those observed in real coastal aquifers. To address this limitation, Abarca et al. (2007) presented a more realistic and generalizable version of the Henry (1964) problem that included both velocity-dependent dispersion and anisotropy in hydraulic conductivity. We therefore modify the Henry (1964) problem to include more realistic molecular diffusion and dispersion. Flow and transport boundary conditions are shown in Figure 2.1. Various levels of anisotropy are considered, depending on the DFN being simulated. Fractures were then included in the problem to simulate SWI in discretely fractured aquifers.

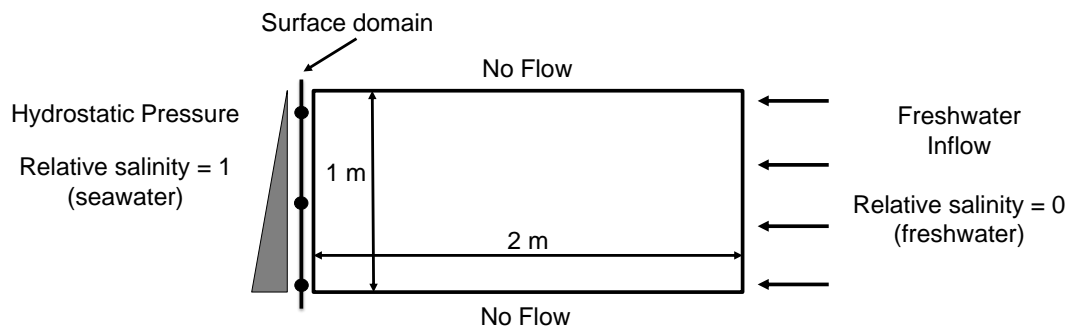


**Figure 2.1** Problem domain and boundary conditions.

The coupled surface-subsurface coastal boundary condition developed by Yang et al. (2013) was applied in our study (see Figure 2.1) to produce more realistic salinity distributions in the upper part of the near-shore aquifer relative to the original Henry (1964) problem. The vertically orientated surface domain at the (left) seaside boundary represents a vertical cross section below the shoreline across which surface-subsurface solute mass and water mass fluxes are calculated (Yang et al., 2013). A hydrostatic pressure distribution is assumed along the (vertical) left surface domain. All surface domain nodes are assigned a constant concentration ( $C$ )

relative to seawater, i.e.  $C = 1$ . Water enters the aquifer at seawater concentration and discharges at the ambient groundwater concentration.

The model domain was discretised into uniform block elements of sizes  $\Delta x = \Delta z = 0.0125$  m and  $\Delta y = 1$  m. The 3D model has a unit width to replicate a 2D domain. We recognise that the grid discretisation employed here is large in comparison to the recommendations offered by Weatherill et al. (2008), who note that even their coarsest grid (100 times greater than the fracture aperture, i.e. 200b) is extremely fine in comparison to most groundwater models. However, a grid convergence test, in which other discretisations (i.e.  $\Delta x = \Delta z = 0.025$  m, 0.0125 m and 0.00625 m) were evaluated, demonstrated that the chosen mesh resolution provides a grid-independent result. Some fracture configurations were more finely discretised ( $\Delta x = \Delta z = 0.00625$  m) to accommodate the higher density of fractures. Computational restrictions (i.e. avoiding excessively long run times) therefore limit our model domain size to small-scale SWI problems (e.g. the Henry problem) if grid-independent results are to be achieved. The chosen grids produced grid Peclet numbers ( $Pe$ ) between 0.125 and 0.2, satisfying the widely accepted stability criterion (Kinzelbach, 1986):

$$Pe = \left( \frac{v\Delta L}{D} \right) \leq 2 \quad (2.1)$$

where  $\Delta L$  (L) is the element length in the direction of flow,  $v$  (L/T) is the average linear velocity and  $D$  (L<sup>2</sup>/T) is the dispersion coefficient.

The simulation period of 69 days was subdivided using adaptive time-stepping based on a maximum 1% change of the salt concentration at any node. Simulations

were run in transient flow and transport mode until steady-state conditions were reached.

We recognise that the various published forms of the Henry (1964) problem (e.g. Henry, 1964; Simpson and Clement, 2004; Abarca et al., 2007) are contrived representations of SWI in natural systems. However, the Henry (1964) problem (and modifications thereof) has been used extensively for analysing SWI processes, and its strengths and limitations are well-documented (see Croucher and O'Sullivan, 1995; Simpson and Clement, 2003). Hence, it serves as a useful basis, with some modification to consider fracture effects, for evaluating potential fracture effects on the extent of seawater in coastal aquifers.

A total of four metrics (Figure 2.2) were analysed to evaluate fracture effects and to identify the key structural properties of fracture networks that influence seawater distribution. These are: (1) the seawater wedge toe location (where the 0.5 isochlor intersects the bottom model boundary, herein referred to as the toe), (2) the seawater-freshwater flux inflexion location at the seaward boundary (seawater flows inland beneath the inflexion point, and freshwater discharges above the inflexion point), (3) the centre of mass in the aquifer, and (4) the width of the mixing zone (the horizontal and vertical distances between the 0.1 and 0.9 isochlors at the bottom and seaward model boundaries, respectively). The impacts of discrete fractures on the equivalent freshwater hydraulic head distributions and flow fields were also evaluated.

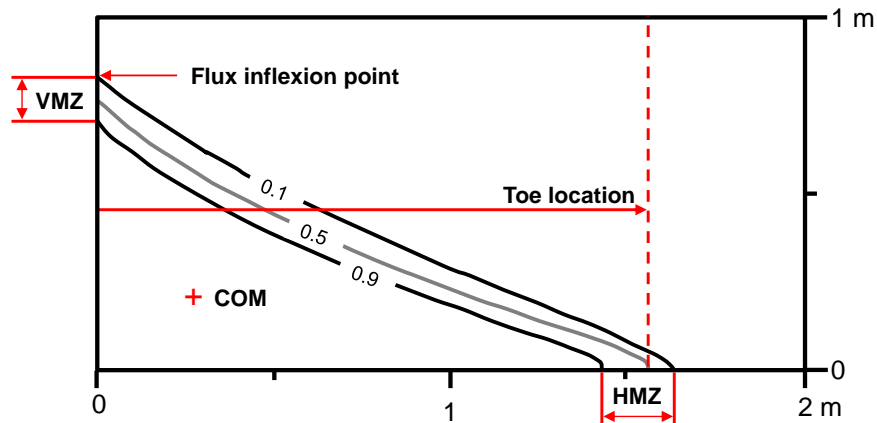


**Figure 2.2** Schematic description of the SWI comparison metrics: (a) the toe location, (b) the flux inflexion point, (c) the centre of mass (COM), and (d) the horizontal and vertical widths of the mixing zone (HMZ and VMZ, respectively).

### 2.3.3 Numerical model

The simulations presented here were conducted using HydroGeoSphere (HGS; Therrien et al., 2010). HGS is a physics-based integrated surface-subsurface hydrogeological model, which solves 3D variable-density flow and solute transport in discretely fractured porous media. HGS has been benchmarked previously against the Elder (1967) salt convection problem (e.g. Therrien et al., 2010) and the Henry (1964) problem (e.g. Yang et al., 2013) for variable-density flow and transport in porous media. The control volume finite-element method is applied to spatially discretise the governing flow and transport equations. Fractures are incorporated in HGS as 2D planes with uniform head across the fracture width (Therrien et al., 2010). The 2D fracture elements are superimposed onto 3D matrix elements in a manner that ensures continuity of the hydraulic heads and solute concentrations at the fracture-matrix interface (Graf and Therrien, 2008). In a fracture, solute transport is only simulated within the 2D plane of the fracture and as such, solute transport perpendicular to the fracture is controlled solely by the

matrix. Detailed descriptions of the governing equations in HGS and the discrete fracture approach are provided elsewhere (e.g. Therrien and Sudicky, 1996; Shikaze et al., 1998; Therrien et al., 2010), and are not repeated here.

#### **2.3.4 Fractured aquifer cases: Modified Henry problem**

Figure 2.3 illustrates the various fractured aquifer cases, which include aquifers containing a single transmissive fracture (Cases A and B; Figure 2.3) or a regular network of transmissive fractures (Cases C, D and E; Figure 2.3). Here, transmissive fractures are more conductive than the surrounding rock matrix. We neglect the situation of fractures that are less transmissive than the surrounding matrix (e.g. sealed fractures; Laubach, 2003), because HGS is presently unable to represent discrete fractures (i.e. where fracture flow is calculated according to the cubic law (Berkowitz, 2002; Graf and Therrien, 2007)) as barriers to flow. The location of a single vertical fracture (Case A) or horizontal fracture (Case B) was modified incrementally by moving the fracture in the horizontal ( $x_{frac}$ ) or vertical ( $z_{frac}$ ) directions ( $x_{frac} = 0.2$  m, 1.0 m and 1.8 m for vertical fractures and  $z_{frac} = 0.2$  m, 0.5 and 0.8 m for horizontal fractures). Cases C, D and E were devised to examine the influence of both fracture spacing and inclination on the inland extent and distribution of seawater, for cases of uniformly distributed and continuous fractures. Case C includes various networks of orthogonal fractures, while Cases D and E involve fractures with inclinations of  $45^\circ$  and  $135^\circ$ , respectively. Level 3 to 5 scenarios are included for completeness (i.e. to provide a wide range of aquifer conditions), albeit the fracture densities are arguably unrealistic compared to field-scale conditions. For each DFN scenario, an EPM model (i.e. a homogenous porous

medium with the same bulk hydraulic conductivity ( $K_b$ ) as the corresponding DFN model) was produced. Parameter values are given in Table 2.1.

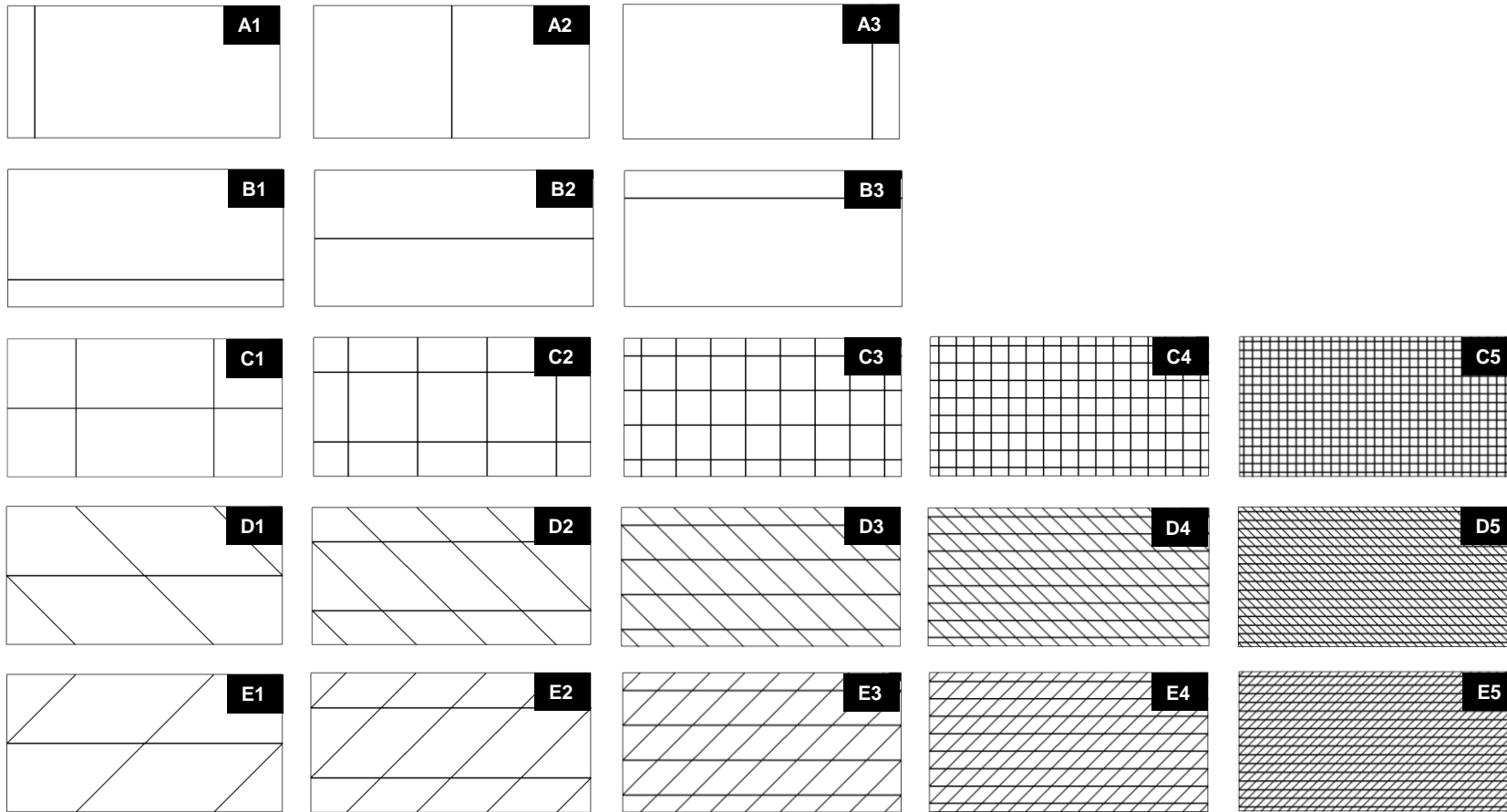


**Figure 2.3** Fracture network Cases A, B, C, D and E. The letter and number in the top right hand corner of each rectangle correspond to the fracture scenario (A-E) and fracture level (1-5).

**Table 2.1** Model parameters used in the fractured forms of the Henry problem.

Parameter	Case A	Case B	Case C, D and E	Case A and B	Case C
				EPM	EPM
Domain length ( $L$ , m)	2	2	2	2	2
Aquifer thickness ( $d$ , m)	1	1	1	1	1
Matrix porosity ( $\theta$ , -)	0.2	0.2	0.2	0.2	0.2
Horizontal hydraulic conductivity ( $K_x$ , m/s)	$10^{-3}$	$2.5 \times 10^{-4}$	$2.5 \times 10^{-4}$	$10^{-3}$	$10^{-3}$
Vertical hydraulic conductivity ( $K_z$ , m/s)	$1.17 \times 10^{-4}$	$2.5 \times 10^{-4}$	$2.5 \times 10^{-4}$	$2.5 \times 10^{-4}$	$10^{-3}$
Free-solution diffusion coefficient ( $D_m$ , m <sup>2</sup> /s)	$10^{-9}$	$10^{-9}$	$10^{-9}$	$10^{-9}$	$10^{-9}$
Freshwater flux ( $q_f$ , m/s)	$6.6 \times 10^{-6}$	$6.6 \times 10^{-6}$	$6.6 \times 10^{-6}$	$6.6 \times 10^{-6}$	$6.6 \times 10^{-6}$
Freshwater density ( $\rho_f$ , kg/m <sup>3</sup> )	1000	1000	1000	1000	1000
Seawater density ( $\rho_s$ , kg/m <sup>3</sup> )	1025	1025	1025	1025	1025
Matrix longitudinal dispersivity ( $\alpha_L$ , m)	0.1	0.1	0.1	0.1	0.1
Matrix transverse dispersivity ( $\alpha_T$ , m)	0.01	0.01	0.01	0.01	0.01
Fracture aperture ( $2b$ , m)	$6.87 \times 10^{-4}$	$9.71 \times 10^{-4}$	$3.85 \times 10^{-4}$ - $9.71 \times 10^{-4}$	-	-
Fracture conductivity ( $K_f$ , m/s)	0.385	0.772	0.122 - 0.772	-	-
Fracture longitudinal dispersivity ( $\alpha_{LF}$ , m)	0.1	0.1	0.1	-	-

The matrix hydraulic properties used in Cases A and B have been set to produce the same EPM models. Conversely, the matrix properties of Cases C, D and E are the same, and therefore produce unique EPM models. An isotropic EPM model (Scenario C6) is representative of all orthogonal fracture network scenarios (C1 to C5), because the fracture aperture ( $2b$ ) was reduced as the fracture spacing ( $2B$ ) decreased to produce an identical  $K_b$  in all models. To achieve this, we used the approach of Vujević et al. (2014), wherein  $K_b$  values were calculated using volumetric fractions of fractures and matrix and their respective hydraulic conductivities ( $K_m$  and  $K_f$ ). That is, the arithmetic and harmonic means were used to determine the aperture of fractures parallel (e.g. Case B) and perpendicular (e.g. Case A) to the primary direction of groundwater flow, respectively. For fracture networks containing fractures both parallel and perpendicular to the primary direction of flow (e.g. Case C),  $K_b$  is given as (Vujević et al., 2014):

$$K_b = \left[ \left( K_m + \frac{(2b)K_f}{(2B)} \right)^{-1} + \frac{(2b)}{K_f(2B)} \right]^{-1} \quad (2.2)$$

A unique, anisotropic EPM model is obtained for all scenarios in Cases D and E due to the different degrees of anisotropy in hydraulic conductivity that results from the inclusion of inclined fractures. For this reason, Equation (2.2) cannot be used to determine  $K_b$  of Cases D and E. The EPM hydraulic properties of Cases D and E were therefore determined numerically by performing Darcy tests to obtain  $K_b$  values in the horizontal and vertical directions. That is, additional simulations were performed wherein a hydraulic head difference ( $\Delta h$ ) was prescribed across the model domain, and directional  $K_b$  values were calculated from the resulting flux rate ( $q_x$ ) using Darcy's law. We note that, for Cases A, B, and C, the Darcy test method results in the same values of  $K_b$  that were obtained using either the

arithmetic and harmonic means, or Equation (2.2) (i.e. for Cases A, B and C, each Darcy model produced  $\Delta h/\Delta x = 0.5$  and  $q_x = 0.0005$  m/s). The applicability of EPM models for approximating the extent of seawater in fractured aquifers was assessed by comparing the DFN model results with those obtained from the corresponding EPM model.

### **2.3.5 Fractured aquifer cases: Field-scale settings**

While the fractured Henry problem provides a useful first step towards identifying the influence of various fracture networks on seawater distributions, the small spatial scale of the problem limits its suitability for examining fracture effects in natural systems. Therefore, models were developed to produce seawater distributions in simplified, field-scale fractured systems with aquifer conditions that are arguably more common than the Henry problem. The  $1000 \text{ m} \times 20 \text{ m}$  2D cross sections represent hypothetical consolidated carbonate aquifers containing regularly spaced, orthogonal fractures (i.e. 5 m horizontal and 10 m vertical spacing). Parameter values are given in Table 2.2.

**Table 2.2** Model parameters used in the fractured field-scale problems.

Parameter	Case 1	Case 2	Case 3	Case 4	Case 5
Domain length ( $L$ , m)	1000	1000	1000	1000	1000
Aquifer thickness ( $d$ , m)	20	20	20	20	20
Matrix porosity ( $\theta$ , -)	0.1	0.1	0.01	0.1	0.2
Horizontal hydraulic conductivity ( $K_x$ , m/s)	$10^{-7}$	$10^{-6}$	$10^{-6}$	$10^{-6}$	$10^{-6}$
Vertical hydraulic conductivity ( $K_z$ , m/s)	$10^{-7}$	$10^{-6}$	$10^{-6}$	$10^{-6}$	$10^{-6}$
Free-solution diffusion coefficient ( $D_m$ , m <sup>2</sup> /s)	$10^{-9}$	$10^{-9}$	$10^{-9}$	$10^{-9}$	$10^{-9}$
Freshwater flux ( $q_f$ , m/s)	$6.6 \times 10^{-9}$				
Freshwater density ( $\rho_f$ , kg/m <sup>3</sup> )	1000	1000	1000	1000	1000
Seawater density ( $\rho_s$ , kg/m <sup>3</sup> )	1025	1025	1025	1025	1025
Matrix longitudinal dispersivity ( $\alpha_L$ , m)	2.0	2.0	2.0	0.2	2.0
Matrix transverse dispersivity ( $\alpha_T$ , m)	0.2	0.2	0.2	0.02	0.2
Fracture aperture ( $2b$ , m)	$2.13 \times 10^{-4}$				
Fracture conductivity ( $K_f$ , m/s)	0.037	0.037	0.037	0.037	0.037
Fracture longitudinal dispersivity ( $\alpha_{LF}$ , m)	2.0	2.0	2.0	0.2	2.0

Boundary conditions were identical to those used in the modified Henry problem (Figure 2.1). We note that due to the scale of the problem, the grid discretisation ( $\Delta x = \Delta z = 2.5$  m) is large compared to the fracture aperture in order to avoid excessively long run times (e.g. halving the cell size to 1.25 m resulted in 138 hour run times for Case 1). Therefore, the results may not be grid-independent. Simulations were run in transient flow and transport mode for a period of 1,900 years (Case 1), 3,150 years (Case 2), 910 years (Case 3), and 6,900 years (Cases 4 and 5), until steady-state conditions were reached. Adaptive time stepping was employed to discretise the simulation time as per the Henry problem variants. Run time for the field-scale DFN models ranged from 15.5 hours to 125.4 hours on a 64-bit Dell Inc. OptiPlex 990. A low matrix porosity simulation (1%, Case 3) is included in Figure 2.14 to extend the range of conditions to situations where a high proportion of the storage occurs within fractures, rather than the matrix.

## **2.4 Results**

Figure 2.4 shows the salinity concentrations relative to seawater in all discretely fractured scenarios and their corresponding EPM models. Case F represents the results of EPM models that correspond to the fractured scenarios of Cases D and E (noting that each scenario in Cases D and E has a unique EPM). The seawater-freshwater interfaces in Scenarios A4 and B4 are compressed relative to Scenarios C6 and F1-F5, demonstrating that the degree of anisotropy in hydraulic conductivity influences the position of the seawater-freshwater interface in the EPM models. In each case, intruding seawater flows inland in the lower half of the aquifer, and subsequently returns to the sea boundary as recirculated groundwater

flowing parallel to the seawater-freshwater transition zone. The recirculation associated with the seawater wedge forces fresh groundwater to discharge through the upper portion of the seaward boundary.

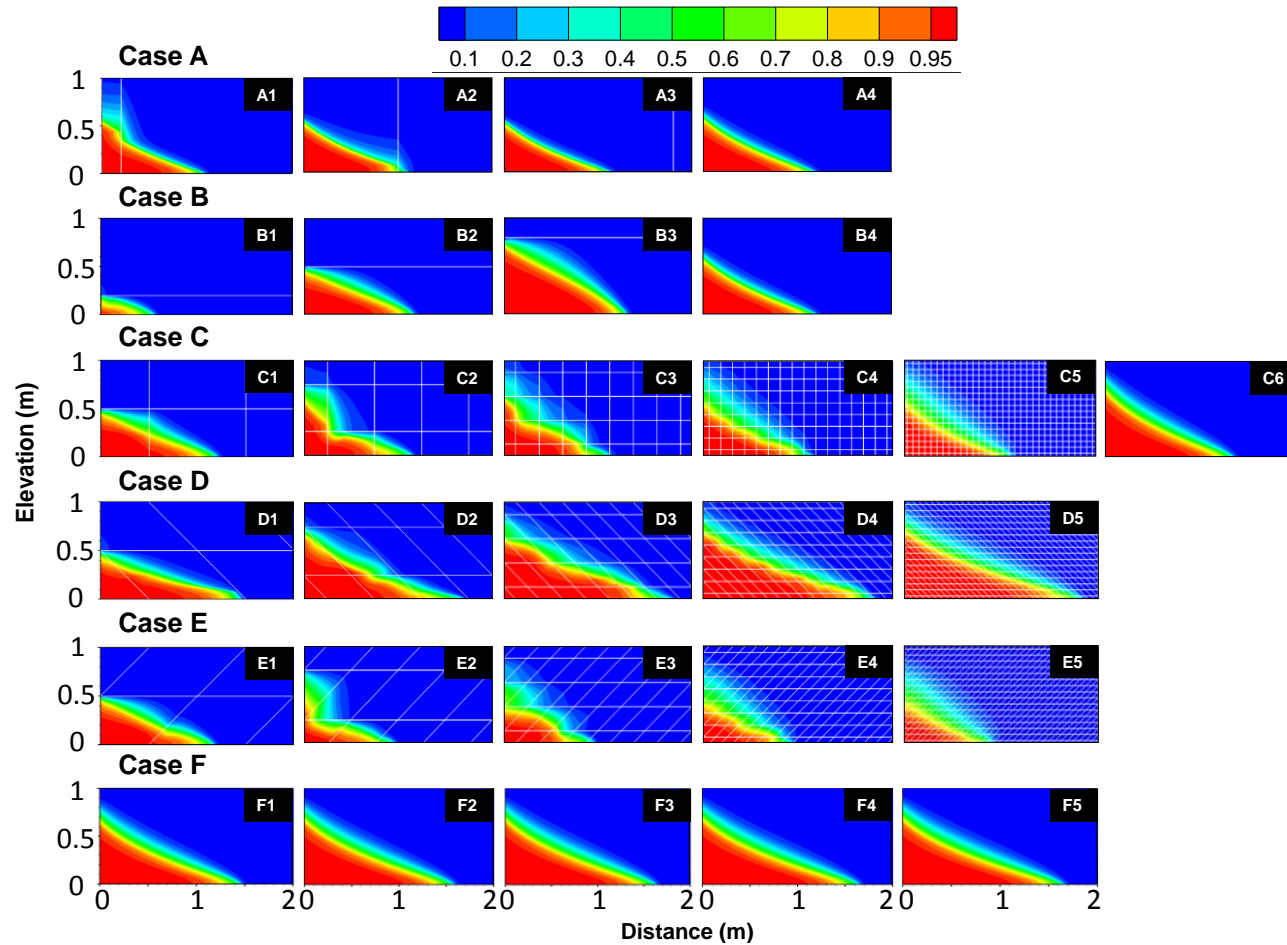


**Figure 2.4** Steady-state salinity distributions in fractured aquifer Cases A, B, C, D and E. Case F represents the EPM results from corresponding scenarios in Cases D and E. Fractures are shown by white lines.

### 2.4.1 Single vertical fracture (Case A)

The influence of adding a single vertical fracture at various locations is illustrated by the Case A salinity distributions shown in Figure 2.4 (A1-A3). The corresponding EPM model is represented by Scenario A4. Figure 2.4 shows that fractures located inside the seawater wedge will have a greater impact on the extent and distribution of seawater in the aquifer.

The seawater wedge metrics for Case A scenarios are given in Figure 2.5. The toe location is shifted landward in the EPM model relative to the DFN models (Figure 2.5a). Overestimation of the toe location by the EPM model is greatest (approximately 11%) when the fracture is positioned within the seawater wedge (Scenario A1) and decreases to approximately 5% (Scenario A3) as the fracture is positioned further inland of the wedge. The EPM model gives reasonable approximations of both the seawater-freshwater flux inflexion location (i.e. within 4% of the DFN model predictions; Figure 2.5b) and the horizontal width of the mixing zone at the bottom boundary (i.e. within 7%; Figure 2.5e), for most DFN model cases. An exception is found in Scenario A2, where the EPM model overestimates the horizontal width of the mixing zone by approximately 10%. The vertical width of the mixing zone at the seaward boundary (Figure 2.5f) is considerably underestimated by the EPM model for Scenario A1, in which the fracture enhances vertical mixing and creates a wider mixing zone near the sea boundary. The vertical fracture in A1 also causes significant modification of the centre of mass (COM), which is approximately 20% further seaward (Figure 2.4c)

and 15% vertically upward (Figure 2.5d) in the EPM model compared to the DFN model.

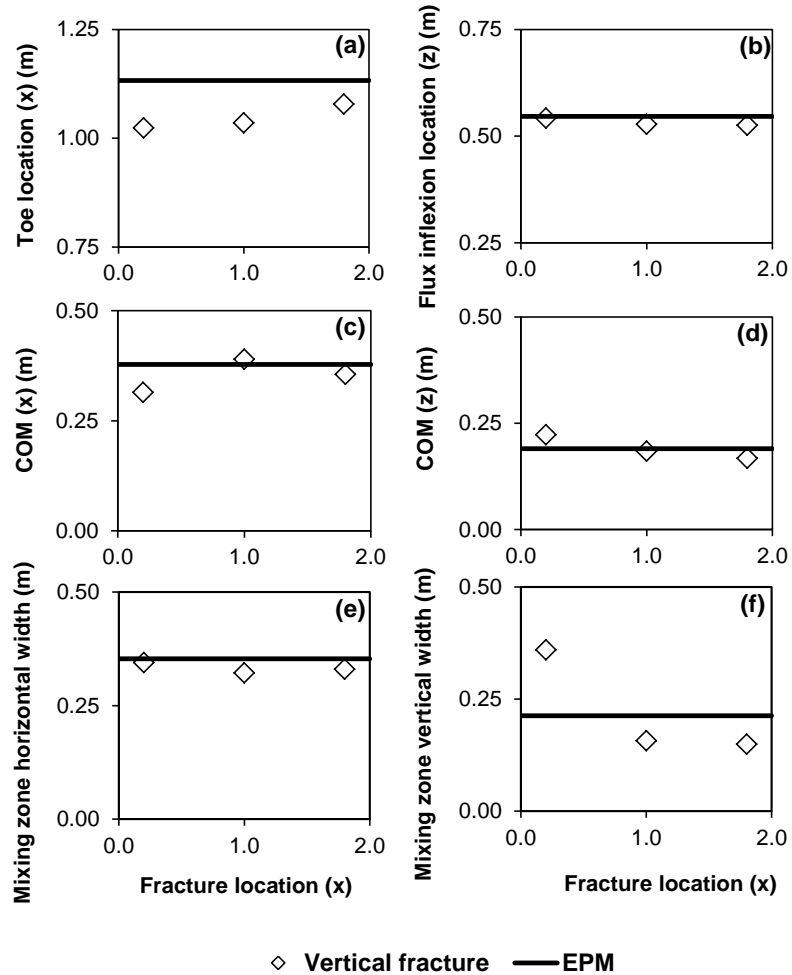


**Figure 2.5** Influence of Case A fracture location on: (a) toe position, (b) flux inflexion location, (c) COM in the  $x$  direction, (d) COM in the  $z$  direction, and (e) and (f) mixing zone widths.

Hydraulic head distributions in Case A scenarios are closely represented by the EPM model (root-mean-square errors of 0.00027 m, 0.00016 m and 0.00015 m for Scenarios A1, A2 and A3, respectively; results not shown for brevity). This result is expected given that flow in the aquifer is predominantly horizontal (i.e. perpendicular to the vertical fractures of Case A).

### **2.4.2 Single horizontal fracture (Case B)**

The Case B salinity distributions depicted in Figure 2.4 (B1-B3) demonstrate the influence of adding a single horizontal fracture at various depths within the aquifer. The corresponding EPM model is represented by Scenario B4. Figure 2.6 illustrates trends in seawater wedge metrics for Case B. The toe location (Figure 2.6a) in the EPM model is further landward (by 140%) relative to the DFN model, whereas the opposite is true for Scenario B3, in which the EPM toe is 11% further seaward than that of the DFN model. Where the fracture is centrally located, proximal to the point of flow inflexion at the coastal boundary (Scenario B2), the fracture has a more subtle influence on the seawater wedge. As such, the EPM and B2 models produce similar (within 3%) toe positions.

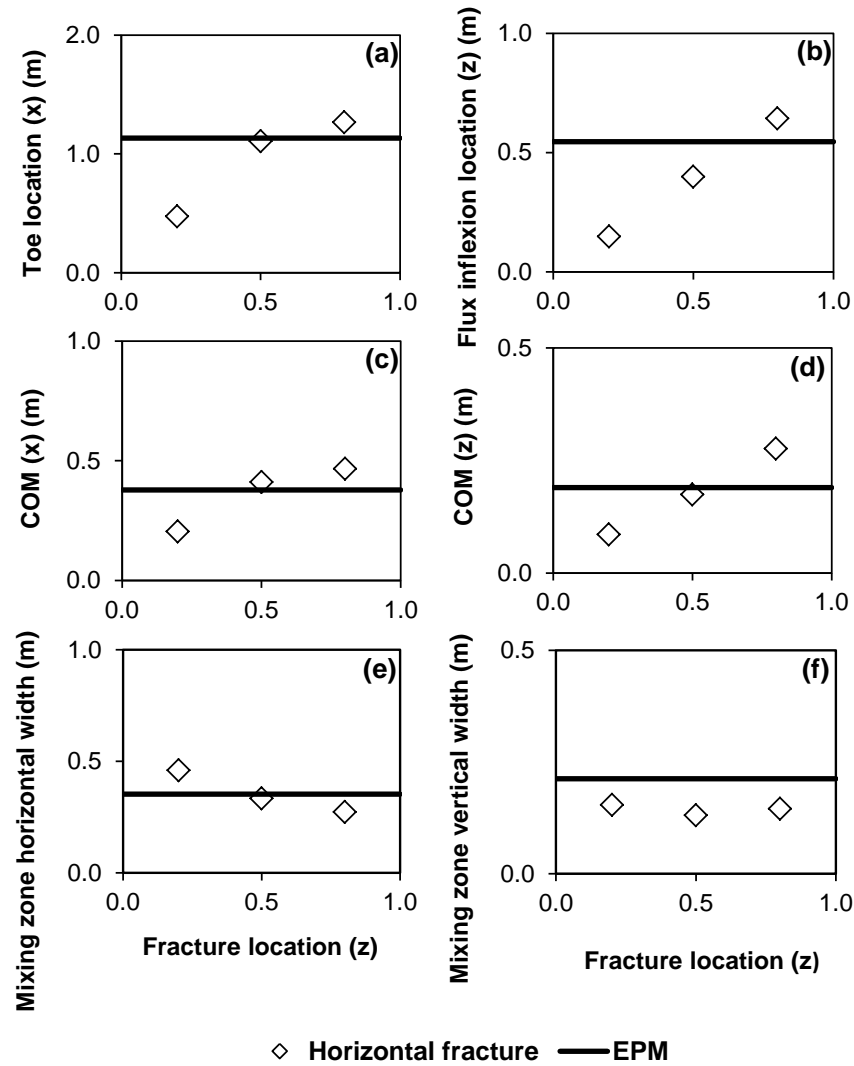


**Figure 2.6** Influence of Case B fracture location on: (a) toe position, (b) flux inflexion location, (c) COM in the  $x$  direction, (d) COM in the  $z$  direction, and (e) and (f) mixing zone widths.

The seawater-freshwater flux inflexion points (Figure 2.6b) from all three fractured rock scenarios of Case B are approximated poorly by the EPM model. Here, discrepancies range from 15% (Scenario B3) to 267% (Scenario B1). The COM of the seawater wedge is shifted corresponding to the position of the fracture – i.e. lower and seaward in Scenario B1, and higher and landward in Scenario B3, compared to the EPM model. The COM is relatively unchanged (< 9% discrepancy) in Scenario B2. The width of the mixing zone at the bottom boundary (Figure 2.6e) is approximated poorly by the EPM model with the exception of Scenario B2. The

width of the mixing zone at the seaward boundary is overestimated (38-63% wider) by the EPM model for all Case B scenarios (Figure 2.6f).

Figure 2.7 shows the significant disturbance to the hydraulic head field caused by the introduction and positioning of a horizontal fracture within the coastal aquifer. Unlike Case A, the hydraulic heads in Case B are represented poorly by the EPM model (root-mean-square errors of 0.0067 m, 0.0020 m and 0.0026 m for Scenarios B1, B2 and B3, respectively). The direction of velocity vectors from Scenarios B1 and B3 are illustrated in Figure 2.8 to highlight the underlying mechanisms behind the considerable influence of horizontal fractures on seawater extent. Regardless of the fracture elevation, there is convergence of freshwater flow towards the fracture in the landward portion of the model domain. This causes freshwater discharge to the sea to occur preferentially through the horizontal fracture, creating a ‘freshwater channelling’ effect. The additional flow through the fracture has distinct influence on the wedge depending on whether freshwater flow within the part of the aquifer containing the wedge is enhanced or reduced by the fracture. When the fracture is located in the bottom half of the aquifer (Scenario B1), the wedge is effectively truncated, whereas freshwater channelling in the upper part of the aquifer (Scenario B3) enhances the extent of seawater due to the reduction in forces (i.e. freshwater discharge) that oppose seawater penetration in the lower domain.

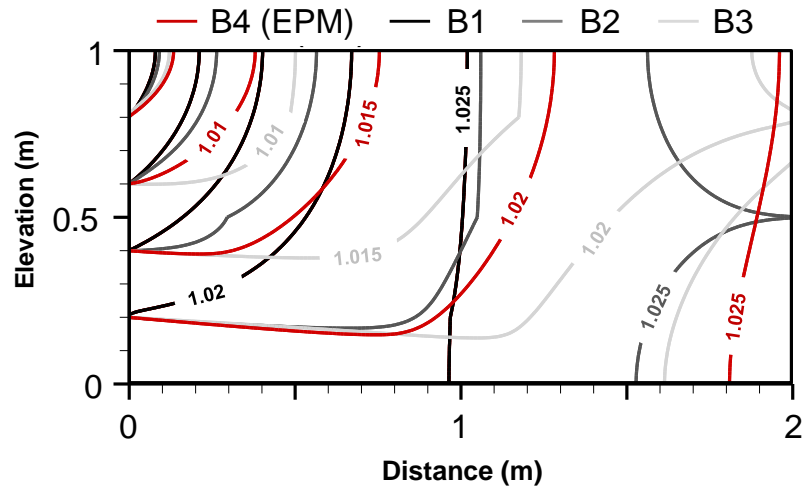


**Figure 2.7** Distribution of equivalent freshwater hydraulic heads at 0.005 m intervals in Case B.

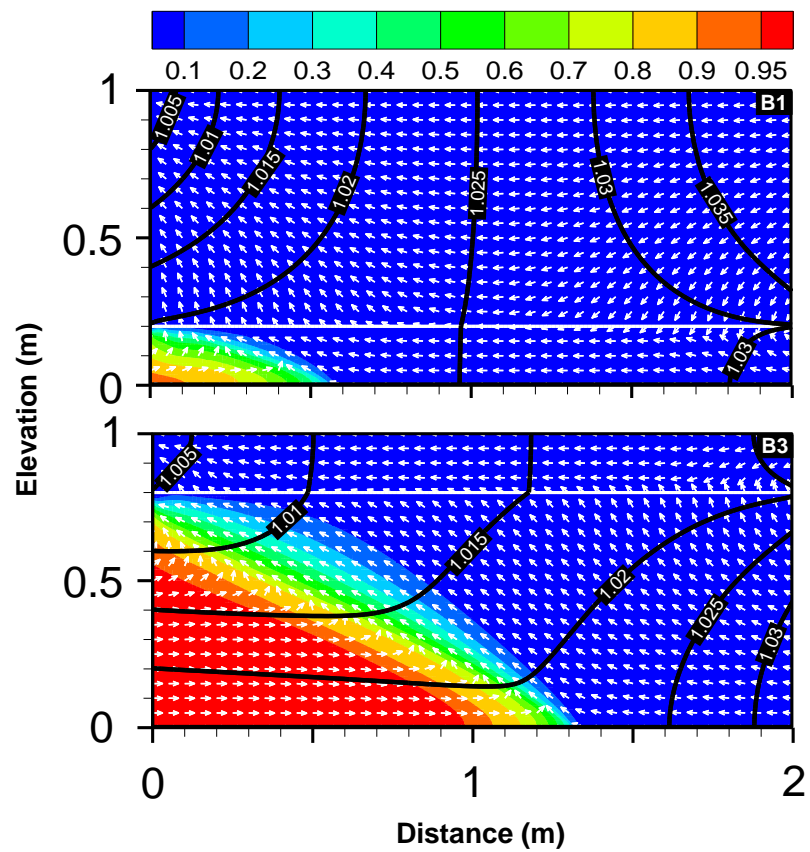


**Figure 2.8** Concentrations relative to seawater (colours), equivalent freshwater hydraulic head contours (black lines), and the direction of velocity vectors (white arrows) for Scenarios B1 and B3.

### **2.4.3 Orthogonal fracture networks (Case C)**

Figure 2.9 illustrates trends in seawater wedge metrics for Case C. The toe location (Figure 2.9a) remains fairly constant for fracture densities greater than Scenario C2 and is consistently overestimated (by approximately 20%) by the EPM model. The horizontal fracture in Scenario C1 has less of an influence on the seawater wedge (i.e. the EPM model overestimates the C1 toe position by 11%) because the fracture is centrally located, coincident with the flow inflexion point at the coastal boundary. A similar effect was also seen in Scenario B2 (refer to Figure 2.4). The seawater-freshwater flux inflexion point (Figure 2.9b) is overestimated by the EPM model in all cases, although as the fracture spacing decreases, the inflexion points produced by the EPM and DFN approaches are in closer agreement.

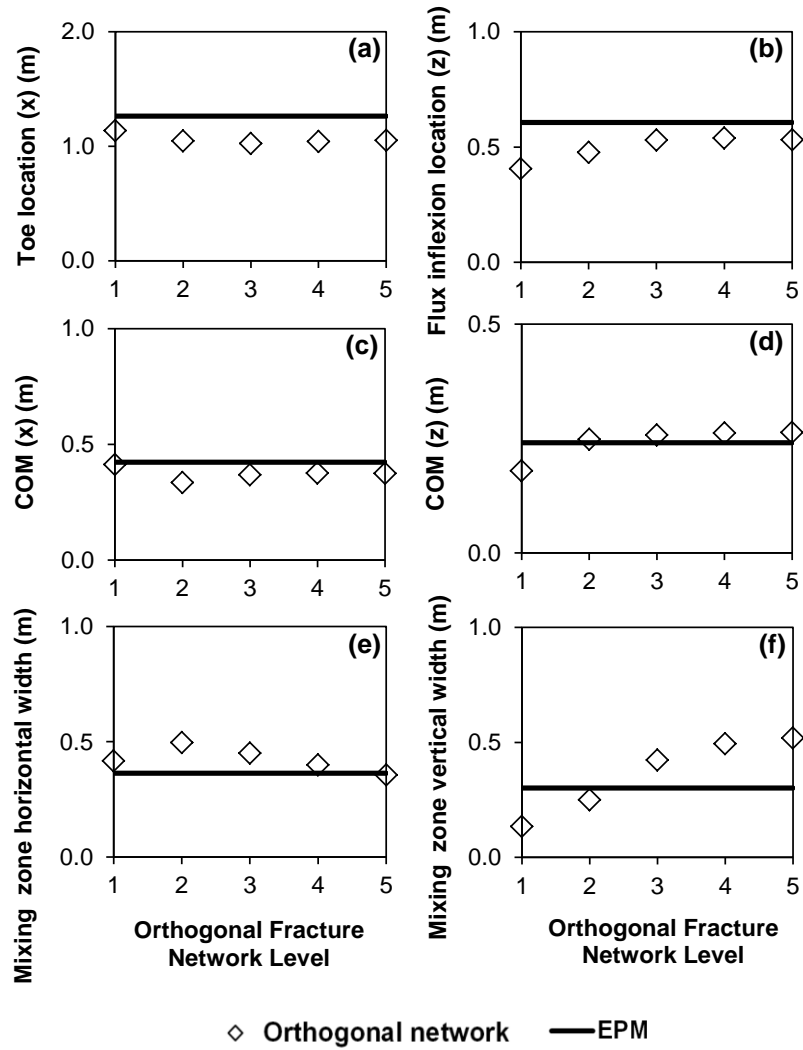


**Figure 2.9** Influence of Case C fracture spacing on: (a) toe position, (b) flux inflexion location, (c) COM in the  $x$  direction, (d) COM in the  $z$  direction, and (e) and (f) mixing zone widths.

The COM of the seawater wedge is shifted landward in the EPM model relative to the DFN models (Figure 2.9c), and the vertical position of the COM is underestimated by the EPM model for Scenarios C2-C5 (Figure 2.9d). As fracture spacing in the DFN models decreases, the COM shifts upwards (Figure 2.9d) and the vertical width of the mixing zone increases (Figure 2.9f).

Figure 2.10 shows the hydraulic head fields, the direction of velocity vectors and the salinity isochlors for Scenarios C1 and C2. The hydraulic heads in Scenarios C1 and C2 are represented poorly by the EPM model (root-mean-square errors of 0.0019 m and 0.00091 m, respectively). However, as the fracture spacing decreases, the hydraulic head distribution can be approximated well by the EPM model (e.g. a root-mean-square error of 0.00033 m for Scenario C4). These results demonstrate that the flow system in the DFN models can be approximated sufficiently well using the EPM approach if fracture density is high. The salinity isochlors for Case C are highly irregular at low fracture levels (e.g. Scenario C1 and C2; Figure 2.10) and become smoother with increasing fracture density, until very little change is observed between Scenarios C4 and C5 (refer to Figure 2.4). However, unlike the groundwater flow system, the EPM model fails to represent adequately the distribution of salt in the aquifer, irrespective of fracture density. This result is expected given that vertical fractures inside the wedge increase dispersive mixing and create a (vertically) wider mixing zone (refer to Case A), and horizontal fractures either enhance or truncate the extent of the seawater wedge, depending on their elevation (refer to Case B). Further, it is well known that heterogeneity tends to enhance mixing effects (Kerrou and Renard, 2010), and hence the dispersiveness of the problem increases with the addition of fractures. The EPM model is unable to capture these processes, at least without modifying the solute transport parameters relative to the DFN cases.

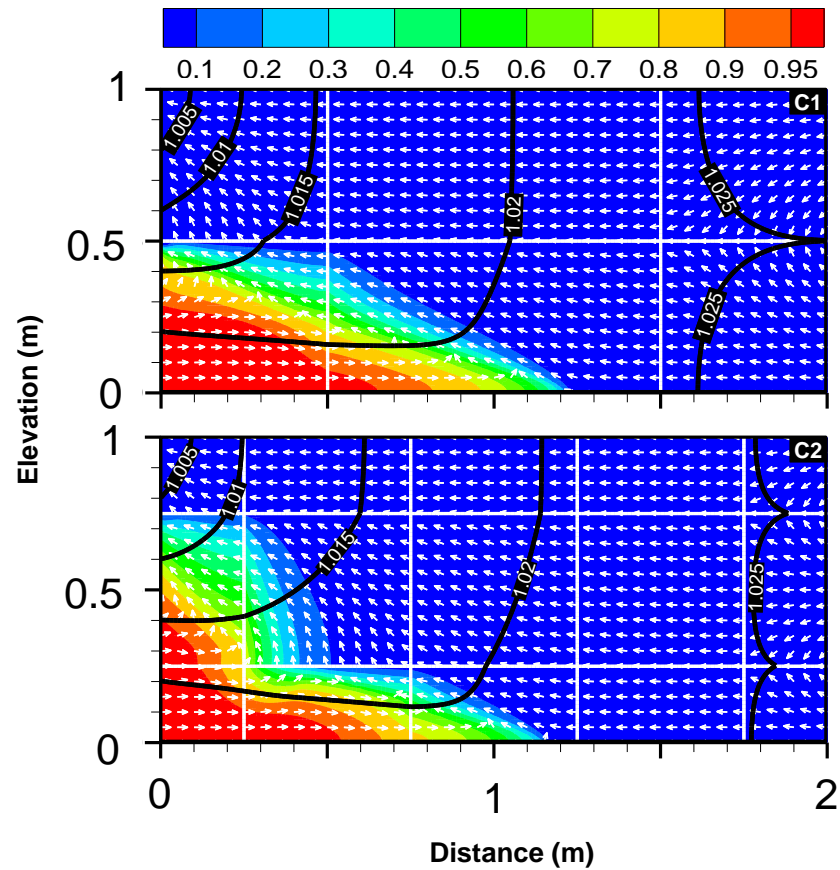


**Figure 2.10** Concentrations relative to seawater (colours), equivalent freshwater hydraulic head contours (black lines), and the direction of velocity vectors (white arrows) for Scenarios C1 and C2.

Figure 2.11 shows the results of a sensitivity analysis evaluating fracture effects on the dispersivity ratio in EPM models of systems containing both vertical and horizontal fractures (Case C). Scenario C4 was chosen for the analysis because the Case C EPM model can replicate sufficiently well the flow field in the DFN model (refer to Section 2.4.3). Figure 2.11 illustrates the distribution of salinity in alternative EPM models for Scenario C4, wherein: (1) the transverse dispersivity is increased from 0.01 m to 0.05 m (solid black line), and (2) the transverse dispersivity is equal to the longitudinal dispersivity (0.05 m, dashed black line). Figure 2.11 demonstrates that by modifying the ratio between transverse and longitudinal dispersivity in the EPM model, a better approximation of the DFN

solution can be achieved. The use of the dispersivity ratio as a calibration parameter may be dependent on whether or not the EPM approach can provide an appropriate representation of the flow field.

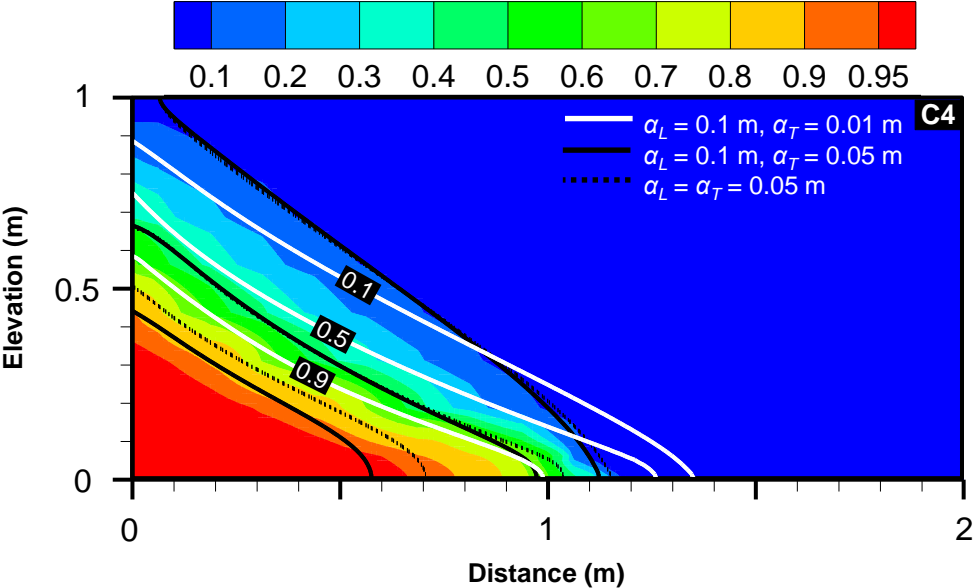


**Figure 2.11** Scenario C4 relative seawater concentrations (coloured bands). The width of the mixing zone is shown for the Case C EPM (white lines) and Case C EPM with modified transverse and longitudinal dispersivities (black solid and black dashed lines).

**2.4.4 Inclined fracture networks (Cases D and E)**

The influence of fracture spacing and inclination on the seawater distribution in regular, inclined fracture networks is shown in Figure 2.4, Cases D and E. The corresponding EPM models for each scenario are illustrated in Figure 2.4, Case F. Figure 2.4 clearly demonstrates that fracture orientation can have a considerable impact on the seawater distribution in fractured aquifers.

Figure 2.12 illustrates trends in seawater wedge metrics for Cases D and E. The toe locations in Case D (Figure 2.12a) are approximated more successfully by the EPM models (variations of < 10%) than the corresponding Case E scenarios (variations of 25-88%). As the fracture spacing in Cases D and E decreases, the EPM approach becomes less appropriate for determining the toe position. The toe location is underestimated by the EPM model when fractures in the DFN model are inclined 45° (Case D), and overestimated when fractures are inclined 135° (Case E). The flux inflexion points are slightly underestimated (2-11%) by the EPM models for Case D (with the exception of Scenario D1, which is overestimated by 32%) and overestimated for Case E (39-86%). The inflexion point in Scenario D1 is considerably lower than D2-D5 because freshwater outflow converges on the single horizontal fracture and creates the same freshwater channelling effect and seawater wedge truncation that was observed in Scenarios B1 and C1.

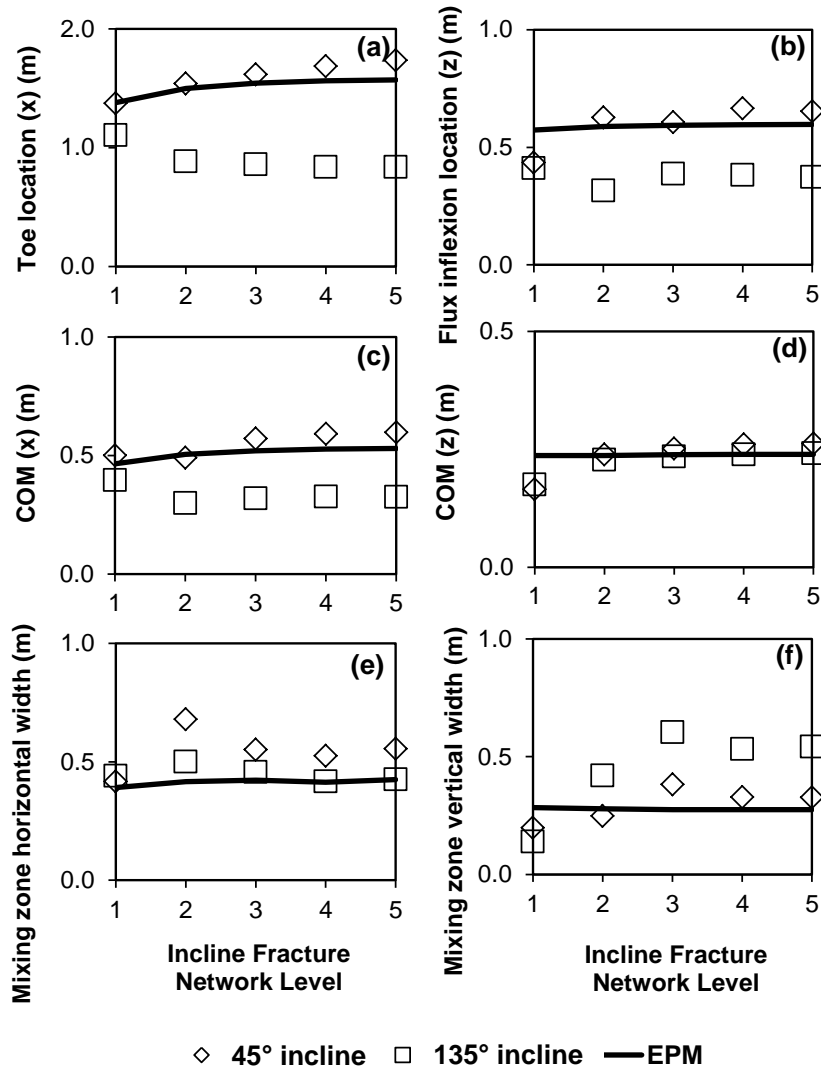


**Figure 2.12** Influence of 45° (Case D) and 135° (Case E) fracture inclination and spacing on: (a) toe position, (b) flux inflexion location, (c) COM in the  $x$  direction, (d) COM in the  $z$  direction, and (e) and (f) mixing zone widths.

The horizontal position of the COM in Case D is underestimated in most cases by the EPM models (Figure 2.12c), although the COM is further seaward in Scenario D2 than in Scenario D1. In contrast, the EPM models of Case E consistently overestimate the horizontal location of the COM. The COM tends to shift further landward as the fracture density increases, with the exception of Scenarios D2 and E2. The vertical location of the COM (Figure 2.12d) is approximated reasonably well by the EPM models (< 9% discrepancies) in most of the Case D and E

scenarios. Only the lowest level DFNs (Scenarios D1 and E1) are overestimated by the EPM models (vertical COM location exceeded by 43% and 35%, respectively). The horizontal width of the mixing zone (Figure 2.12e) is underestimated by the EPM models for all fracture scenarios in Cases D and E. Similarly, the vertical width of the mixing zone (Figure 2.12f) is underestimated by the EPM models for Scenarios D3-D5 and E2-E5. For Scenarios D1 and E1, the vertical widths of the mixing zone are overestimated by the corresponding EPM models because the wedge is compressed beneath the single horizontal fracture in the DFN models.

Figure 2.13 shows the hydraulic head distributions in Scenarios D2 and E2 (Figure 2.13a) and D5 and E5 (Figure 2.13b). Figure 2.13b demonstrates that, unlike in Case C, the hydraulic head field in the higher-density Case D and E scenarios cannot be replicated by the EPM models (Scenario F5). The root-mean-square error for hydraulic head is slightly smaller for Scenario D2 than E2 (0.0011 m and 0.0020 m, respectively), whereas the root-mean-square error for Scenario D4 is an order of magnitude smaller than E4 (0.00094 m and 0.0020 m, respectively).

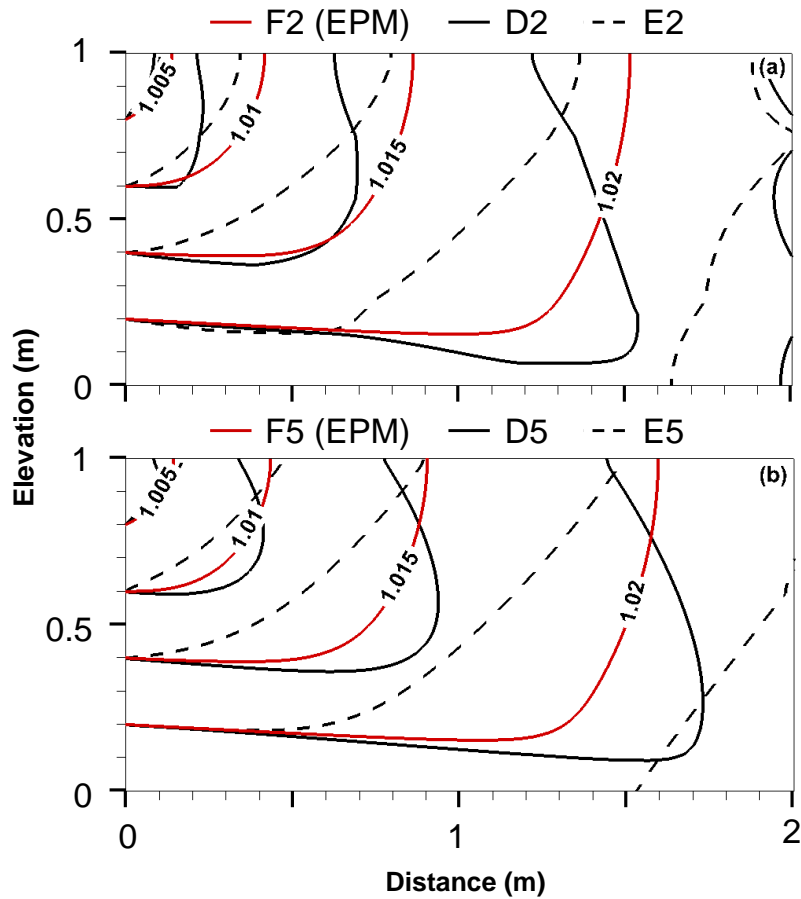


**Figure 2.13** Distributions of equivalent freshwater hydraulic heads in Cases D2, D5, E2 and E5, and their respective EPMs.

### 2.4.5 Field-scale settings

Figure 2.14 shows the seawater distribution in simplified, field-scale fractured systems with aquifer conditions that are arguably more common than the Henry problem. Only the first 500 m of the aquifers are shown for clarity. Trends in seawater wedge metrics are illustrated in Figure 2.15 for Case 1 only, for brevity.

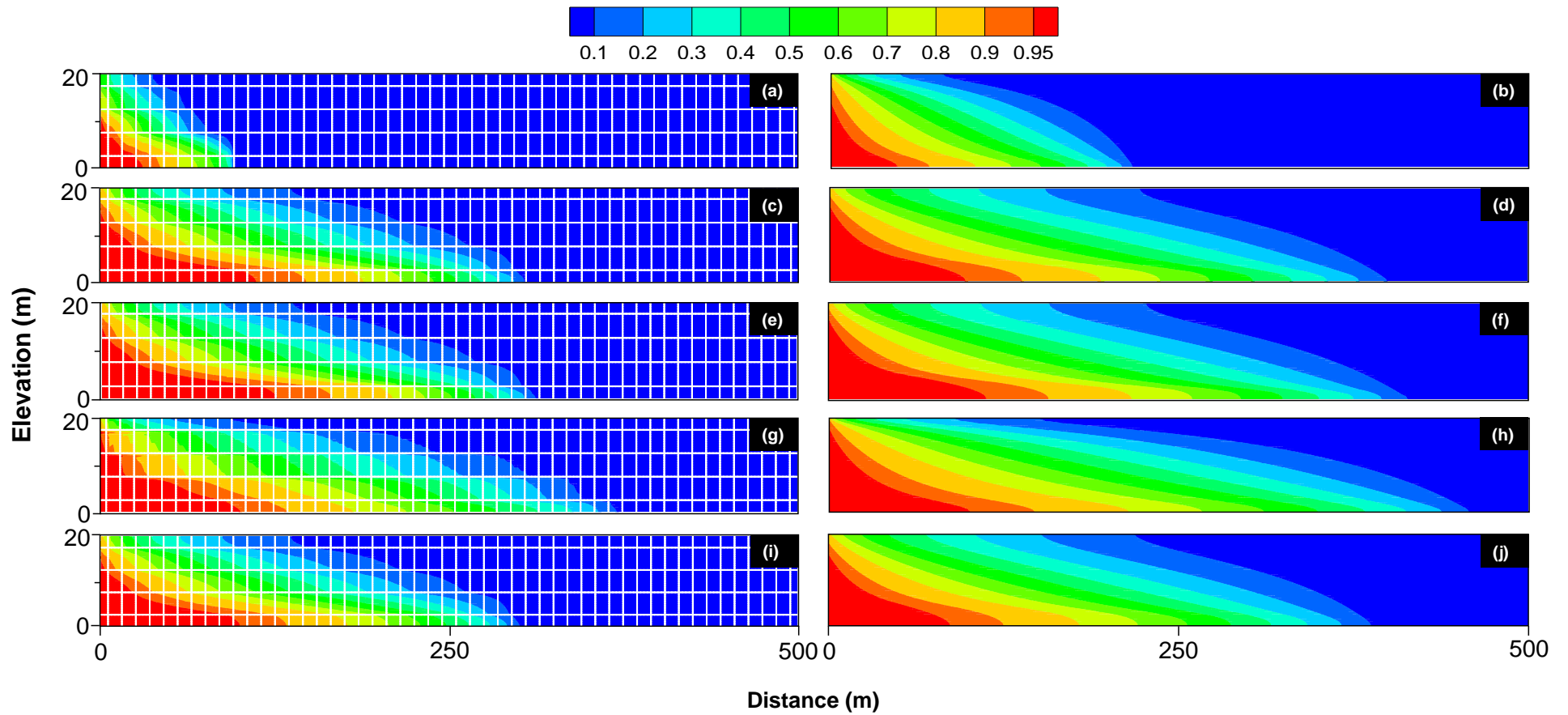


**Figure 2.14** Steady-state salinity distributions in: (a), (c), (e), (g), (i) the field-scale DFN models, and (b), (d), (f), (h), (j) the field-scale EPM models (Cases 1-5, respectively). Fractures are shown by white lines.

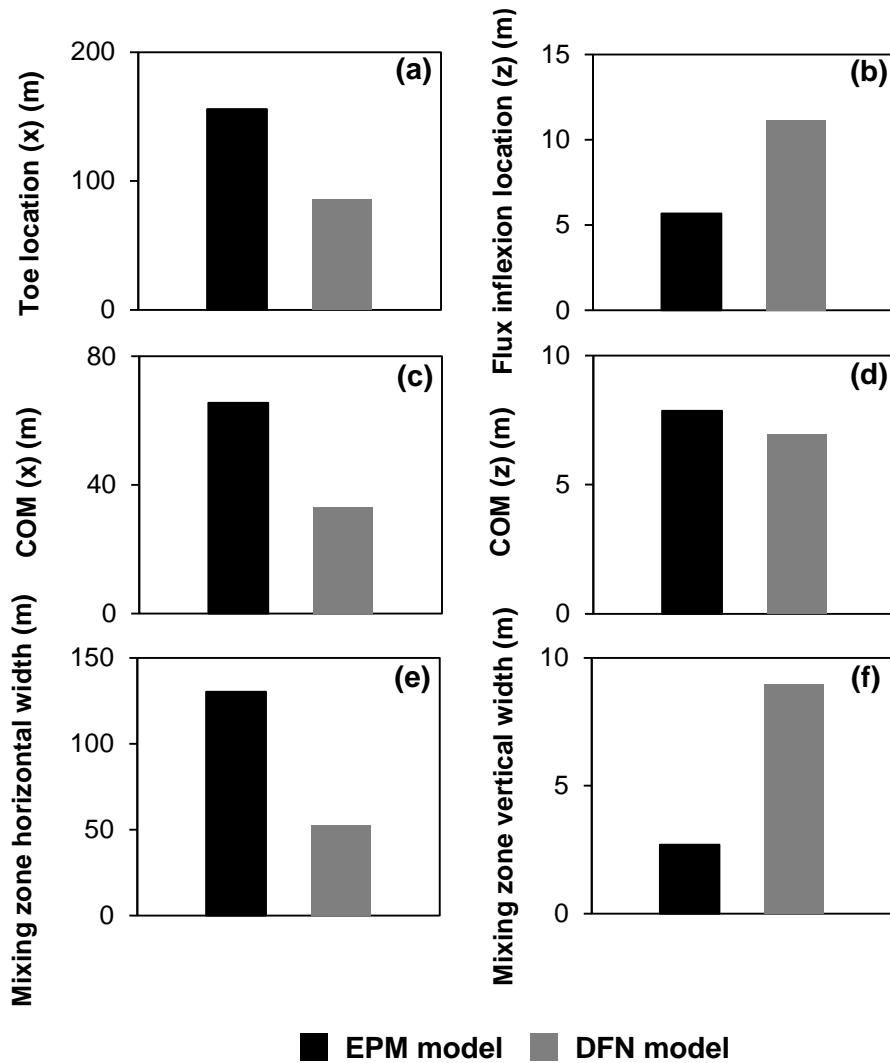


**Figure 2.15** Influence of Case 1 orthogonal fractures on: (a) toe position, (b) flux inflexion location, (c) COM in the  $x$  direction, (d) COM in the  $z$  direction, and (e) and (f) mixing zone widths.

Figures 2.14 and 2.15 demonstrate trends in the field-scale models that are similar to those observed in the higher density Case C scenarios obtained from the modified Henry problem. For example, the seawater wedge in the Case 1 DFN model (Figure 2.14a) is compressed relative to the EPM model (Figure 2.14b). The toe location (Figure 2.15a) and the seawater-freshwater flux inflexion point (Figure 2.15b) are further landward and upward in the DFN model compared with the EPM model, respectively. Further, the Case 1 EPM model overestimates the horizontal location

of the COM (Figure 2.15c) and underestimates the width of the mixing zone at the seaward boundary (Figure 2.15f), as was observed in the majority of Case C scenarios. Discrepancies between the field-scale and Henry problem results were apparent for the vertical location of the COM (Figure 2.15d) and the horizontal width of the mixing zone (Figure 2.15e), which were respectively lower and narrower in the DFN model than the EPM model.

The contours illustrated in Figure 2.14e show a rather subtle effect of reducing the porosity by an order of magnitude. That is, the seawater wedge toe intrudes 13.0 m and 20.7 m further inland in the low-porosity case (Figure 2.14e) compared to the associated higher matrix porosity simulations (i.e. Case 2 (Figure 2.14c) and Case 5 (Figure 2.14i), respectively).

## **2.5 Discussion**

The impacts of fractures on seawater wedge metrics resulting from the current study were similar to some of the findings from the heterogeneous porous media study by Kerrou and Renard (2010). For example, both studies demonstrate that geologic heterogeneity usually widens the seawater-freshwater mixing zone relative to homogeneous cases. This was observed in our study for Scenarios A1, C3-5, D3-D5 and E2-5, in which fractures caused widening in the vertical extent, and for Scenarios B1 and C1-4, and Cases D and E, in which the mixing zone was widened in the horizontal extent. However, narrowing of the mixing zone occurred in Scenarios A2-3, C1-2, D1-2 and E1, and Case B (i.e. in the vertical extent), and in Case A, and Scenarios B2-3 and C5 (i.e. in the horizontal extent). Hence, compared

to random heterogeneities, it is likely that fractures will cause more complicated changes to salinity distributions. The causal factors for widening or narrowing of the mixing zone are discussed further below.

Vertical fractures inside the seawater wedge were found to increase the vertical width of the mixing zone (e.g. Scenarios A1 and C3-C5) in comparison to the EPM (i.e. homogeneous) models. In the DFN models, the flows in vertical fractures were upwards, and where fractures intercepted the wedge, this resulted in upward transport of salt via advection, thereby widening the seawater-freshwater transition zone. For example, the fracture flow in Scenario A1 was  $1.08 \times 10^{-6}$  m<sup>2</sup>/s vertical upwards, averaged along the fracture. Scenario A3 had a significantly smaller upwards flow of  $1.50 \times 10^{-7}$  m<sup>2</sup>/s. The EPM model of Case A produced vertical flows approximately three orders of magnitude smaller than fracture velocities in Case A DFN models. Hence, where vertical fractures encounter seawater wedges, it is likely that EPM approaches are an inadequate approximation of SWI in fractured aquifers, even with modified dispersivity to account for the interface widening, because vertical fractures produce significant localised disturbance to the flow field and the seawater wedge.

Examples of vertical fracture effects on mixing zones in real-world settings include several coastal aquifers throughout Florida (e.g. the Everglades National Park, Price et al., 2003; the Floridan and Biscayne aquifers, Barlow, 2003). Lu et al. (2009) noted that groundwater salinity measurements from the abovementioned aquifers indicate the presence of wide (6-24 km; Price et al., 2003) mixing zones. These predominately carbonate systems are characterised by highly permeable vertical

fractures and karst features that facilitate the upward migration of seawater (e.g. Barlow, 2003; Barlow and Reichard, 2010), and result in enhanced mixing and thicker mixing zones.

In contrast to vertical fractures, systems characterised by only horizontal fractures (i.e. Case B) were found to produce narrower mixing zones at the sea boundary, compared to the EPM model (Figure 2.5f). That is, DFN models produced mixing zones with vertical widths of 0.13 to 0.15 m, whereas the EPM model mixing zone was 0.21 m wide at the sea boundary. In general terms, horizontal fractures are likely to have a greater impact than vertical fractures on the inland extent and distribution of seawater. The reason for this is explored by considering the effect of freshwater channelling through fractures on the overall flow field of the coastal aquifer. Horizontal fractures align with the general flow direction, and hence freshwater discharge to the sea occurs preferentially through the horizontal fractures. The freshwater discharge rate through a single horizontal fracture ( $q_{frac}$ ) increases as the fracture's elevation increases. For example, the ratio of  $q_{frac}$  to the inland freshwater flux ( $q_f$ ) increases from 0.25 in Scenario B1 to 0.44 and 0.66 in Scenarios B2 and B3, respectively. The accompanying reduction in discharge from the porous matrix (equal to  $q_f - q_{frac}$ ) in Scenarios B2 and B3 thus enables more seawater to penetrate the unfractured lower model domain, resulting in more extensive regions of seawater in Scenarios B2 and B3 compared to B1. The sensitivity of seawater extent to the fracture's location highlights the limitations of the EPM approach, which may not be suitable for predicting the vertical and lateral extents of seawater in fractured aquifers if the primary orientation of fractures is

horizontal (e.g. such as the Nardò aquifer, Italy; Masciopinto et al., 2008; Chrysikopoulos et al., 2010).

Horizontal fractures in DFNs containing vertical or inclined fractures with lower fracture densities (Scenarios C1, C2, D1, D2 and E1) also produce narrower mixing zones at the sea boundary, because horizontal fractures (rather than vertical or inclined fractures) dominate disturbances to the flow field. Here, the majority of incoming freshwater converges on either one (Scenarios C1, D1 and E1) or two (Scenarios C2 and D2) horizontal fractures, which become preferential pathways for freshwater discharge to sea, thereby tending to truncate the mixing zone at the fracture elevation. The freshwater channelling effect is stronger at low fracture densities, and EPM models of these are unable to approximate sufficiently well the narrowing of the interface that accompanies widely spaced horizontal fractures.

The higher-density fracture scenarios, with orthogonal fractures (i.e. Scenarios C4 and C5), produce a similar effect on the seawater wedge to the heterogeneities introduced by Kerrou and Renard (2010). Scenarios C4 and C5 produced seawater wedges that were shifted seaward and upward, widening the mixing zone relative to the EPM case. Hence, the fracture density is a key factor in determining whether the mixing zone will be wider or narrower than the EPM case.

The EPM model of Case C is unable to reproduce the seawater distribution, regardless of the fracture density. At high fracture densities (Scenarios C4 and C5), the EPM model provides a reasonable estimate of the steady-state flow field but is unable to reproduce the salt distribution. Following the work of Rubin and

Buddemeier (1996), it may be possible to reproduce the seawater distribution of high-density DFN models by adopting modified transverse and longitudinal dispersivities. Rubin and Buddemeier (1996) demonstrated that contaminant transport in some fractured porous formations can be represented by an EPM model using an appropriate value of transverse dispersivity. They showed that in fractured systems with high matrix permeability, the ratio between transverse and longitudinal dispersivity that is required to reproduce contaminant distributions using an EPM model is sensitive to the orientation of fractures. As the fracture angle relative to the direction of flow ( $\theta_f$ ) approaches  $90^\circ$ , transverse dispersivity may exceed longitudinal dispersivity. As  $\theta_f$  approaches  $0^\circ$ , longitudinal dispersivity increases and advective fracture flow dominates (Rubin and Buddemeier, 1996). As expected from Rubin and Buddemeier (1996) for the case of non-density dependent transport, our results demonstrate that the ratio between transverse and longitudinal dispersivity is also an important factor when using the EPM approach to simulate density-dependent problems (i.e. SWI) in fractured systems.

The results from Cases D and E highlight the effect of fracture inclination on seawater extent. Fractures almost parallel to the seawater interface ( $45^\circ$  incline; Case D) facilitate SWI and increase the penetration length of the wedge, whereas fractures roughly perpendicular to the interface ( $135^\circ$  incline; Case E) channel freshwater discharge to the sea and inhibit SWI. Transverse dispersion is enhanced by the perpendicular fractures, which increases the width of the mixing zone, as expected from the results for Case A. The results from the inclined fracture networks presented in this study indicate that generally, the EPM approach may provide more reliable approximations of seawater wedge metrics in cases where

fracture inclination is approximately parallel (rather than perpendicular) to the seawater-freshwater interface, and where fracture spacing is small. Further, the hydraulic head field in scenarios where fractures are orientated approximately perpendicular to the interface cannot be approximated using the EPM approach, regardless of fracture density.

The results shown in Figure 2.14 indicate that the problem appears to be somewhat insensitive to the value of matrix porosity, and rather, matrix-fracture hydraulic conductivity contrasts are more important in controlling the characteristics of the seawater distribution. Notwithstanding differences between the Henry and field-scale results, as mentioned above, the patterns in seawater distribution observed in the small-scale models may be amenable to upscaling under certain aquifer conditions.

## **2.6 Conclusions**

In this study, the influence of simple fracture network geometries on the distribution of seawater in fractured coastal aquifers is investigated. We consider confined aquifers under equilibrium conditions, and a series of uniform fracture networks and boundary conditions. The simulation results presented here provide an important first step towards determining the distribution of seawater in more complex fractured coastal aquifer settings. The key findings of this study are:

- 1) Vertical fractures within the seawater wedge will likely increase the width of the seawater-freshwater mixing zone, whereas vertical fractures inland of

the wedge have a minimal influence on the seawater distribution in the aquifer.

- 2) Horizontal fractures in the lower part of the aquifer effectively truncate the seawater wedge, whereas horizontal fractures in the zone of freshwater discharge may enhance the inland extent of the wedge.
- 3) Inclined fractures that are approximately parallel to the seawater-freshwater interface can facilitate SWI, whereas fractures roughly perpendicular to the interface inhibit SWI.
- 4) Homogeneous EPM models using bulk hydraulic conductivities are not suitable for inferring the distribution of seawater in the majority of DFN scenarios, although the EPM approach may be adequate for high density, orthogonal fracture scenarios if the flow system can be well-represented and appropriate EPM dispersivity values can be determined.

This study examines a range of simple regularly spaced fracture network geometries, yet a variety of complex salinity distributions were observed. In real-world coastal aquifers, it is likely that this variability will be amplified due to the complexity of real-world fracture networks and the resulting variations in geologic heterogeneity. The results indicate that the fracture density and fracture orientation are important considerations in developing models that simulate the distribution of seawater in fractured aquifers. Substantial underestimations of seawater extent can arise if only the hydraulic properties of the aquifer matrix are considered. Similarly, simulations utilising only the combined (bulk) fracture and matrix hydraulic properties (i.e. the EPM approach) may lead in some cases to considerable overestimations of seawater extent. Persistent differences between the field and

Henry-scale models require additional investigation, but are attributable to non-linear upscaling and grid resolution effects. Given these results, the use of EPM models to examine the distribution of seawater in fractured coastal aquifers is likely inapplicable in most cases. It would be useful to extend this study by investigating irregular fracture networks, i.e. where fracture length and fracture spacing are no longer uniform, to further ascertain how the structural properties of fracture networks impact the extent and distribution of seawater in fractured coastal systems.

## Chapter 3

### 3. A modelling investigation of solute transport in permeable porous media containing a discrete preferential flow feature

*This chapter is based on the following published paper:*

Sebben, M. L., Werner, A. D., 2016. A modelling investigation of solute transport in permeable porous media containing a discrete preferential flow feature. *Adv. Water Resour.* 94, 307-317, doi: 10.1016/j.advwatres.2016.05.022

#### 3.1 Abstract

Preferential flow features (PFFs, e.g. fractures and faults) are common features in rocks that otherwise have significant matrix permeability. Despite this, few studies have explored the influence of a PFF on the distribution of solute plumes in permeable rock formations, and the current understanding of PFF effects on solute plumes is based almost entirely on low-permeability rock matrices. This research uses numerical modelling to examine solute plumes that pass through a PFF in permeable rock, to explore the PFF's influence on plume migration. The study adopts intentionally simplified arrangements involving steady-state solute plumes in idealised, moderate-to-high-permeability rock aquifers containing a single PFF. A range of matrix-PFF permeability ratios ( $4.9 \times 10^{-6}$  to  $2.5 \times 10^{-2}$ ), typical of fractured sedimentary aquifers, is considered. The results indicate that for conditions representative of high-to-moderate-permeability sedimentary rock matrices containing a medium-sized fracture, the effect of the PFF on solute plume displacement and spreading can be considerable. For example, plumes are between 1.3 and 19 times wider than in associated porous media only scenarios, and

medium-sized PFFs in moderately permeable matrices can reduce the maximum solute concentration by up to  $10^4$  times. Plume displacement and spreading is lower in aquifers of higher matrix-PFF permeability ratios, and where solute plumes are more dispersed at the point of intersection with the PFF. Asymmetry in the plume caused by the passage through the PFF is more pronounced for more dispersive plumes. The current study demonstrates that PFFs most likely govern solute plume characteristics in typical permeable matrices, given that a single PFF of aperture representing a medium-sized fracture (i.e.  $5.0 \times 10^{-4}$  m) produces the equivalent spreading effects of 0.22-7.88 m of plume movement through the permeable matrix.

### **3.2 Introduction**

There are numerous problems of environmental concern that involve the transport of solutes in rocks containing preferential flow features (PFFs) such as fractures and faults. These include the long-term disposal of high-level radioactive waste (Reeves et al., 2008), groundwater contamination arising from urban development and industrialization (Birkhölzer et al., 1993a), amongst many others. In recent decades, considerable research attention has been given to the transport of solutes in aquifers of low-permeability rock matrices containing PFFs, where the transport of solutes occurs primarily via advection and dispersion within the PFF, and exchanges between PFFs and the rock matrix occur by molecular diffusion (e.g. Grisak and Pickens, 1981; Sudicky and Frind, 1982; Himmelsbach et al., 1998; Bense et al., 2013, Gassiat et al., 2013). This body of work has demonstrated that PFFs can provide pathways through which contaminated fluids can migrate rapidly relative to transport in the rock matrix (i.e. the primary porosity), which can

attenuate solute breakthrough curves and cause longer residence times than impermeable rocks containing PFFs (Bear et al., 1993; Singhal et al., 2010).

Flow and transport in aquifers containing PFFs and with moderate-to-high matrix permeability requires consideration of solute advection, mechanical dispersion and molecular diffusion in both the PFF and the porous matrix (Birkhölzer et al., 1993a). These conditions have received far less attention compared to low-permeability matrix settings (Rubin et al., 1997; Odling and Roden, 1997). This is despite that PFFs are common features in high-yielding, permeable rock aquifers (e.g. fractured limestone and sandstone), and are critical factors in the occurrence of many groundwater-dependent ecosystems (e.g. springs and outflows along PFFs in carbonate rocks; Bauer-Gottwein et al., 2011).

Studies of solute transport in permeable matrices containing PFFs include the work of Birkhölzer et al. (1993a; 1993b), Rubin and Buddemeier (1996), Rubin et al. (1997), Odling and Roden (1997), Sonnenborg et al. (1999) and Houseworth et al. (2013). Birkhölzer et al. (1993a; 1993b) presented an analytical model to describe advection-dominated solute transport (i.e. diffusion/dispersion is negligible) in a 2D PFF network embedded in a permeable rock matrix. The authors developed a ‘diffusion-advection number’ to determine the conditions for which diffusive exchange (via molecular diffusion) between the PFF and matrix is insignificant relative to advective PFF-matrix solute exchange. Results from numerical simulations (Birkhölzer et al., 1993b) indicated that solute transport in permeable rock matrices containing parallel, equidistant PFFs with uniform aperture can be represented using an equivalent porous media (EPM) approach if the representative

elementary volume of the network is large enough. Rubin and Buddemeier (1996) demonstrated that in permeable formations, the ratio of transverse to longitudinal dispersivity that is required to reproduce contaminant distributions in an EPM model is sensitive to the orientation of the PFF. Transverse dispersivity may exceed longitudinal dispersivity as the PFF angle relative to the direction of flow ( $\alpha_{pff}$ ) approaches  $90^\circ$ . As  $\alpha_{pff}$  approaches  $0^\circ$ , longitudinal dispersivity increases and advection in the PFF dominates flow in the system. These studies consider formations that can be approximated using the EPM approach, and do not provide insight into the local-scale effects of individual, discrete PFFs on the distribution of solute plumes in permeable matrices.

The methodology of Birkhölzer et al. (1993a; 1993b) was employed by Rubin et al. (1997) to examine solute transport in permeable media containing PFFs when the flow velocities inside PFFs are slow (i.e. the flow velocity inside the PFF is of the same order of magnitude as the matrix flow velocity). They found that the larger the deviation of the matrix-PFF velocity ratio from unity, the greater the effective dispersivity of the fractured permeable formation (Rubin et al., 1997). Odling and Roden (1997) used numerical modelling to study 2D flow and solute transport in permeable rock containing PFFs arranged according to naturally occurring geometries. They found that in permeable matrices (i.e. unlike for low-permeability rock), PFF orientation and density can be as influential as PFF connectivity on contaminant transport rates and solute plume heterogeneity. Hence, matrix-PFF hydraulic conductivity contrasts and PFF orientation are likely to influence the distribution of solutes in permeable rock matrices that are subject to both advective and dispersive transport processes. The effect of an individual PFF on solute

transport in permeable matrices was not considered in the abovementioned studies; despite that transport processes at small scales can influence dramatically solute transport at larger scales (Grisak and Pickens, 1980).

Laboratory experiments and numerical modelling were carried out by Sonnenborg et al. (1999) to examine 2D flow and solute transport in a permeable matrix with variable aperture PFFs. They demonstrated that the EPM approach may be justified for modelling preferential flow systems where physically realistic values for macro-porosity and macro-dispersivity could be obtained. Further experimental and theoretical work was recommended to test the range over which the EPM approach might be valid. Houseworth et al. (2013) obtained a closed-form analytical solution for solute transport during steady-state saturated flow in a single PFF embedded within a porous, permeable rock matrix. Unlike existing analytical solutions, Houseworth et al. (2013) incorporated lateral matrix diffusion, and flows through both the matrix and PFF. Their study considered the case where matrix diffusion dominates in comparison to matrix dispersion, and hence they did not provide insight into the effect of a PFF on a solute plume in a matrix that is subjected to both advection and dispersion.

Case studies of solute transport in karst aquifers (i.e. PFFs that are formed by fractures, faults and/or karst conduits) include Bonacci and Roje-Bonacci (1997) and Arfib et al. (2007). Mechanisms of seawater intrusion (SWI) through coastal karst springs were investigated in Blaž, Croatia (Bonacci and Roje-Bonacci, 1997) and central Crete, Greece (Arfib et al., 2007). Both studies demonstrated that PFFs can alter the distribution of seawater in coastal aquifers compared with the classical

description of a 'seawater wedge' in porous media. A recent study by Sebben et al. (2015) employed numerical models to investigate the characteristics of SWI in permeable rock matrices containing simple PFF network geometries. Their study demonstrated that PFFs can either widen or narrow the seawater wedge relative to porous media only (PMO) formations, depending on the PFF location and orientation. While Sebben et al. (2015) offer macro-scale descriptions of PFF effects on SWI plumes, the mechanisms that underlie solute plume widening (or narrowing) as it passes through an individual PFF were not explored because of the complex effects of heterogeneities on the density-dependent flow field. Quantitative analyses of solute plumes that intercept a PFF are needed at local scales to explain the integrated, macro-scale solute behaviour of previous PFF-permeable matrix studies.

The purpose of the current study is to explore within a modelling framework the influence of a single PFF (representing a medium-sized fracture) on the distribution of solutes in a permeable rock matrix. Numerical simulations are conducted to investigate PFF effects on a 2D solute plume caused by a point source, under steady-state groundwater flow conditions where regional flow is oblique to the PFF. Results are compared with associated PMO models, to determine the influence of PFFs on both the horizontal displacement of peak solute concentrations and the spreading of contaminant plumes in permeable rock matrices. We examine the distribution of solutes for a variety of matrix-PFF permeability ratios (given in terms of hydraulic conductivity, i.e. the matrix hydraulic conductivity is modified) and contaminant source locations, adopting aquifer properties that are representative of sedimentary rocks (e.g. sandstone and limestone) in which

preferential flow through discrete features and flow in the matrix are known to occur (e.g. Webb et al., 2010; Al Ajmi et al., 2014).

### **3.3 Methodology**

#### **3.3.1 Conceptual model**

The discrete fracture network (DFN) approach, wherein individual PFFs are incorporated explicitly into an n-dimensional model as (n-1)-dimensional features (e.g. Smith and Schwartz, 1984), was employed in constant-density numerical modelling experiments. PFFs within a DFN are assumed to contain water that is fully-mixed across the PFF width, such that solute concentration is uniform across the PFF's aperture. The model used here to evaluate PFF effects simulates groundwater flow and solute transport in a 1 m × 1 m 2D cross section through a homogeneous, isotropic, confined aquifer containing a single, discrete horizontal PFF at  $z = 50$  cm. The small domain size was chosen because very fine grid spacing perpendicular to the PFF-matrix interface ( $\Delta z \approx$  PFF aperture) is required if grid-independent results are to be achieved (Weatherill et al., 2008). Computational restrictions (i.e. avoiding excessively long run times) currently limit the application of DFN models to small-scale solute transport problems, if grid-independent results are sought (e.g. Tang et al., 1981; Graf and Simmons, 2009).

The model set up, including flow and transport boundary conditions, is shown in Figure 3.1. Constant head boundaries are prescribed so that the groundwater flow direction ( $\alpha_f$ ) is  $45^\circ$  relative to the orientation of the PFF. An  $\alpha_f$  of  $45^\circ$  was chosen

so that displacement of streamlines is expected to occur (i.e.  $0^\circ < \alpha_f < 90^\circ$ ). The flow field in the matrix is unaffected by the introduction of the PFF, because the model set up is such that the superposition principle applies to the flow field. A continuous mass flux of solute is assigned at  $x = 2.50$  cm, and  $z = 50.4125$  cm (Scenario 1),  $z = 54.8438$  cm (Scenario 2), or  $z = 85.00$  cm (Scenario 3) (i.e., 0.4125, 4.8438 or 35.00 cm, respectively, above the PFF). Various ratios of matrix-to-PFF hydraulic conductivity ( $K_m/K_f$ ) are considered that produce flow velocity ratios less than unity (i.e. the velocity in the PFF is larger than in the permeable block).  $K_m$  values were chosen to encapsulate a range of documented permeable matrix values, including limestone (e.g.  $10^{-6}$  m/s  $\leq K_m \leq 10^{-3}$  m/s; Geiger et al., 2010; Webb et al., 2010), and sandstone (e.g.  $10^{-8}$  m/s  $\leq K_m \leq 10^{-5}$  m/s; Birkhölzer et al., 1993a; Al Ajmi et al., 2014). Values for PFF aperture ( $2b$ ) are in the range of published values for PFFs in permeable matrices (e.g.  $10^{-4}$  m to  $10^{-3}$  m; Birkhölzer et al., 1993a; Sonnenborg et al., 1999; Geiger et al., 2010) and are representative of a medium-sized fracture. PFF hydraulic conductivity ( $K_f$ ) is given as (e.g. Graf and Therrien, 2007):

$$K_f = \frac{(2b)^2 \rho g}{12\mu} \quad (3.1)$$

where  $2b$  [L] is PFF aperture,  $\rho$  [M/L<sup>3</sup>] is fluid density,  $g$  [L/T<sup>2</sup>] is gravitational acceleration, and  $\mu$  [M/LT] is fluid dynamic viscosity.

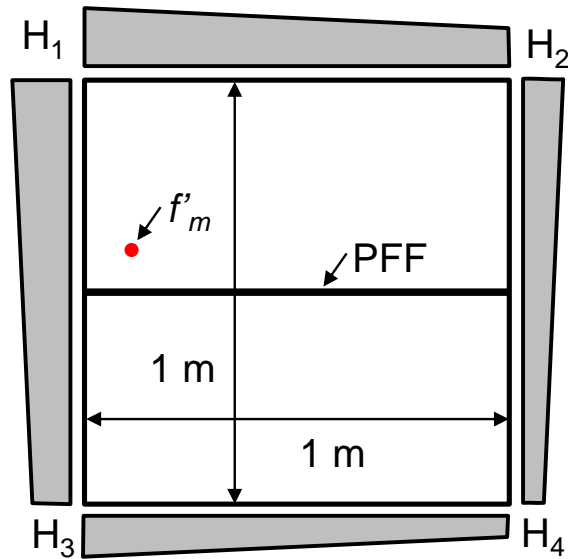


**Figure 3.1** Conceptual model of the DFN cases, where  $H$  is hydraulic head and  $f'_m$  is contaminant mass flux.

The model domain was discretised into variable block elements ranging from  $\Delta x = 0.39$  mm at the solute source to  $\Delta x = 6.25$  mm at the right model boundary. Vertical layers were refined from  $\Delta z = 0.25$  mm around the PFF to  $\Delta z = 1.25$  mm the domain boundaries, leading to 627,984 nodes. Grid Peclet numbers ranged from 0.078 to 1.25 (longitudinal), and 0.5 to 3.125 (transverse). The 3D model has a unit width to replicate a 2D domain. Simulations were first run in steady-state mode to produce equilibrium flow conditions with the PFF in place. Solute transport was then run in transient mode until steady-state conditions were reached. The simulation period of 92 days was subdivided using adaptive time-stepping based on a maximum 1% change in salt concentration at any node.

The displacement of peak solute concentrations as plumes pass through the PFF, the lateral extent of the solute plumes, and the solute concentrations above and below the PFF were analysed to evaluate the distribution of solutes in the aquifer for various parameter combinations. The locations of solute peaks at  $z = 49.975$  cm

(i.e. directly beneath the PFF) were obtained for both DFN and PMO situations to assess the displacement distance of the plume ( $D$ , Figure 3.2) as it passes through the PFF.

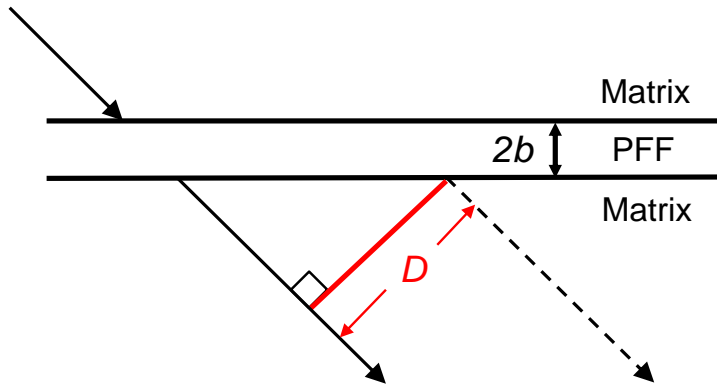


**Figure 3.2** Schematic description of the peak solute concentration displacement,  $D$ . The solid black arrow represents the main plume trajectory in the PMO models. The black dashed arrow represents the plume trajectory at the maximum solute concentration beneath the PFF in the DFN model.

The solute plume width (i.e. the horizontal width between concentration ( $C$ ) values of  $0.001 \text{ kg/m}^3$  at the outer edges of the plume) was analysed directly beneath the PFF and compared with that obtained for the PMO models. Using the methods described above, we explore how a medium-sized PFF embedded in a permeable rock matrix can influence the distribution of a solute plume, for a range of conditions typical of fractured sedimentary aquifers.

### 3.3.2 Numerical model

The simulations presented here were conducted using HydroGeoSphere (HGS; Therrien et al., 2010). HGS is a physics-based hydrogeological model, which solves 3D flow and solute transport in discretely fractured porous media. HGS has been

benchmarked previously against the Tang et al. (1981) analytical solution for solute transport in a single PFF embedded within a porous, impermeable rock matrix (e.g. Weatherill et al., 2008). In that case, fluid flow occurs in the PFF only, and solute transport occurs in both the matrix (via molecular diffusion only) and the PFF (via advection, longitudinal mechanical dispersion and molecular diffusion). HGS has also been benchmarked against the Wilson and Miller (1978) analytical solution (e.g. Therrien et al., 2010) describing the 2D dispersion of a solute plume in porous media under uniform, steady-state flow conditions, given as:

$$C = \frac{f'_m \exp\left(\frac{x}{B}\right) K_0\left(\frac{r}{B}\right)}{2\pi\theta(D_x D_z)^{\frac{1}{2}}} \quad (3.2.1)$$

$$B = \frac{2D_x}{V} \quad (3.2.2)$$

$$r = \left(x^2 + z^2 \frac{D_x}{D_z}\right)^{\frac{1}{2}} \quad (3.2.3)$$

where  $C$  [M/L<sup>3</sup>] is solute concentration,  $f'_m$  [M/LT] is the contaminant mass flux per unit length,  $x$  [L] is the distance from the plume along the  $x$ -axis,  $z$  [L] is the distance from the plume along the  $z$ -axis,  $\theta$  [-] is the matrix porosity,  $D_x$  [L<sup>2</sup>/T] is the longitudinal dispersion coefficient,  $D_z$  [L<sup>2</sup>/T] is the transverse dispersion coefficient,  $V$  [L/T] is the seepage velocity in the direction of flow, and  $K_0$  is the modified Bessel function of the second kind. While there has been no benchmarking of HGS for a situation of solute transport in a permeable rock matrix containing a PFF, the previous model testing demonstrates numerical robustness for our purposes, in particular considering the lack of an analytical expression for the current problem.

Individual PFFs are incorporated in HGS as 2D planes with uniform head across the PFF width (Therrien et al., 2010). The 2D PFF elements are superimposed onto 3D matrix elements such that continuity of the hydraulic heads and solute concentrations at the PFF-matrix interface is maintained (Graf and Therrien, 2008). Flow through PFFs is calculated according to the cubic law, i.e. Darcy's law and Equation (3.1) (Berkowitz, 2002; Graf and Therrien, 2007). Solute transport within PFFs is only simulated within the 2D plane of the PFF and as such, solute transport perpendicular to the PFF is controlled solely by the matrix. Detailed descriptions of the governing equations in HGS and the discrete PFF approach are provided elsewhere (e.g. Therrien and Sudicky, 1996; Shikaze et al., 1998; Therrien et al., 2010), and are not repeated here.

### 3.3.3 Fractured aquifer scenarios

Five different  $K_m/K_f$  ratios are simulated (Cases A to E). A sixth case (Case F) with lower  $\theta$  and smaller  $2b$  is included to extend the range of situations considered. Within each of the six cases, three scenarios are examined wherein the solute plume source is located at various heights above the PFF (0.4125 cm (Scenario 1), 4.8438 cm (Scenario 2) and 35 cm (Scenario 3). Each scenario contains a single, continuous horizontal PFF at  $z = 50$  cm. All PFFs are more transmissive than the surrounding porous matrix because presently, HGS is unable to represent barrier PFFs (i.e. PFFs containing material with a lower permeability than the host rock; Neumann, 2005) using the DFN approach.  $f'_m$  is modified in each case to maintain a constant concentration of  $1.0 \text{ kg/m}^3$  at the point source. For each DFN scenario, a PMO model with the same matrix properties is produced to assess PFF effects as the

difference between DFN and PMO solute distributions. Parameter values for each of the cases are listed in Table 3.1.

**Table 3.1** Model parameters for Cases A to F.

Parameter	Case A	Case B	Case C	Case D	Case E	Case F
Matrix porosity ( $\theta$ , -)	0.2	0.2	0.2	0.2	0.2	0.1
Matrix hydraulic conductivity ( $K_m$ , m/s)	$5.0 \times 10^{-3}$	$1.0 \times 10^{-3}$	$5.0 \times 10^{-4}$	$2.5 \times 10^{-4}$	$1.0 \times 10^{-6}$	$1.0 \times 10^{-5}$
Matrix longitudinal dispersivity ( $\alpha_L$ , m)	$5.0 \times 10^{-3}$	$5.0 \times 10^{-3}$				
Matrix transverse dispersivity ( $\alpha_T$ , m)	$5.0 \times 10^{-4}$	$5.0 \times 10^{-4}$				
Darcy velocity in the matrix ( $q_m$ , m/s)	$7.07 \times 10^{-4}$	$1.41 \times 10^{-4}$	$7.07 \times 10^{-5}$	$3.54 \times 10^{-5}$	$1.41 \times 10^{-7}$	$1.41 \times 10^{-6}$
PFF aperture ( $2b$ , m)	$5.0 \times 10^{-4}$	$2.5 \times 10^{-4}$				
PFF hydraulic conductivity ( $K_f$ , m/s)	0.204	0.204	0.204	0.204	0.204	0.051
PFF longitudinal dispersivity ( $\alpha_{LF}$ , m)	$5.0 \times 10^{-3}$	$5.0 \times 10^{-3}$				
Darcy velocity in the PFF ( $q_f$ , m/s)	$2.04 \times 10^{-2}$	$5.11 \times 10^{-3}$				
Solute mass flux ( $f'_m$ , kg/m/s)	$1.75 \times 10^{-6}$	$3.54 \times 10^{-7}$	$1.78 \times 10^{-7}$	$8.90 \times 10^{-8}$	$3.28 \times 10^{-10}$	$3.66 \times 10^{-9}$
Matrix-PFF hydraulic conductivity ratio ( $K_m/K_f$ , -)	$2.5 \times 10^{-2}$	$4.9 \times 10^{-3}$	$2.4 \times 10^{-3}$	$1.2 \times 10^{-3}$	$4.9 \times 10^{-6}$	$2.0 \times 10^{-4}$

### 3.4 Results

#### 3.4.1 Visual inspection of PFF effects on solute plumes

Figure 3.3 shows the direction of velocity vectors and the salinity isochlors for the PMO (Figure 3.3a) and DFN models (Figure 3.3b) of Scenario A1. Groundwater flows from the top left of the aquifer to the bottom right, at a  $45^\circ$  angle to the PFF

and at a Darcy velocity (in the porous matrix) of  $7.07 \times 10^{-4}$  m/s in the direction of flow. The solute plume develops from a continuous point source (at  $x = 2.5$  cm,  $z = 50.4125$  cm) above the PFF.

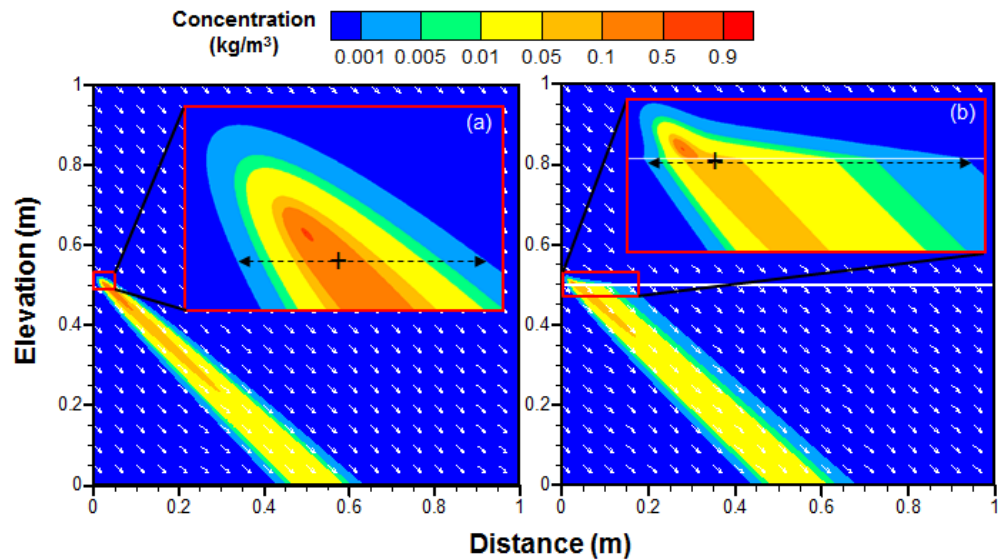


**Figure 3.3** Schematic description of the solute plume comparison metrics in: (a) the PMO model, and (b) the DFN model (shown for Scenario A1). Colours represent the solute concentrations. White arrows show the direction of velocity vectors. Black dashed arrows indicate the width of the solute plume. Black crosses highlight the location of maximum solute concentration immediately beneath the PFF. The PFF is shown by the white line.

The metrics analysed in the current study are illustrated in Figure 3.3. The black dashed line indicates the location of comparison between solute plume widths in the PMO (Figure 3.3a) and DFN (Figure 3.3b) models. The black cross in Figure 3.3 highlights the location of the maximum solute concentration beneath the PFF, from which  $D$  values are ascertained in the forthcoming analysis.

The influence of a single horizontal PFF located within a moderate-to-high-permeability porous matrix on solute plume spreading is illustrated in Figure 3.4,

for all cases (A to F). The corresponding PMO model is shown for Scenario A1 only (Figure 3.3a), for brevity.

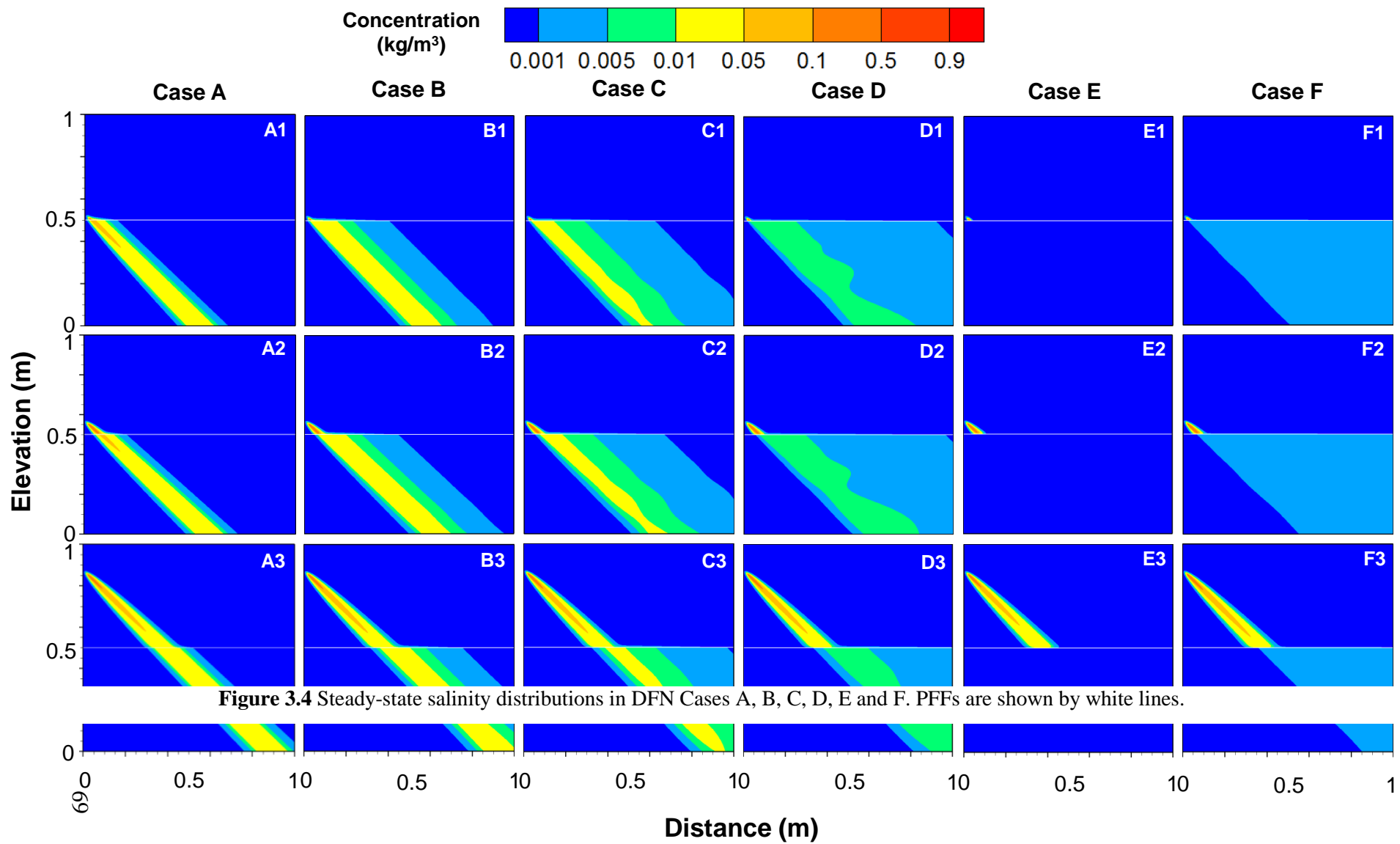
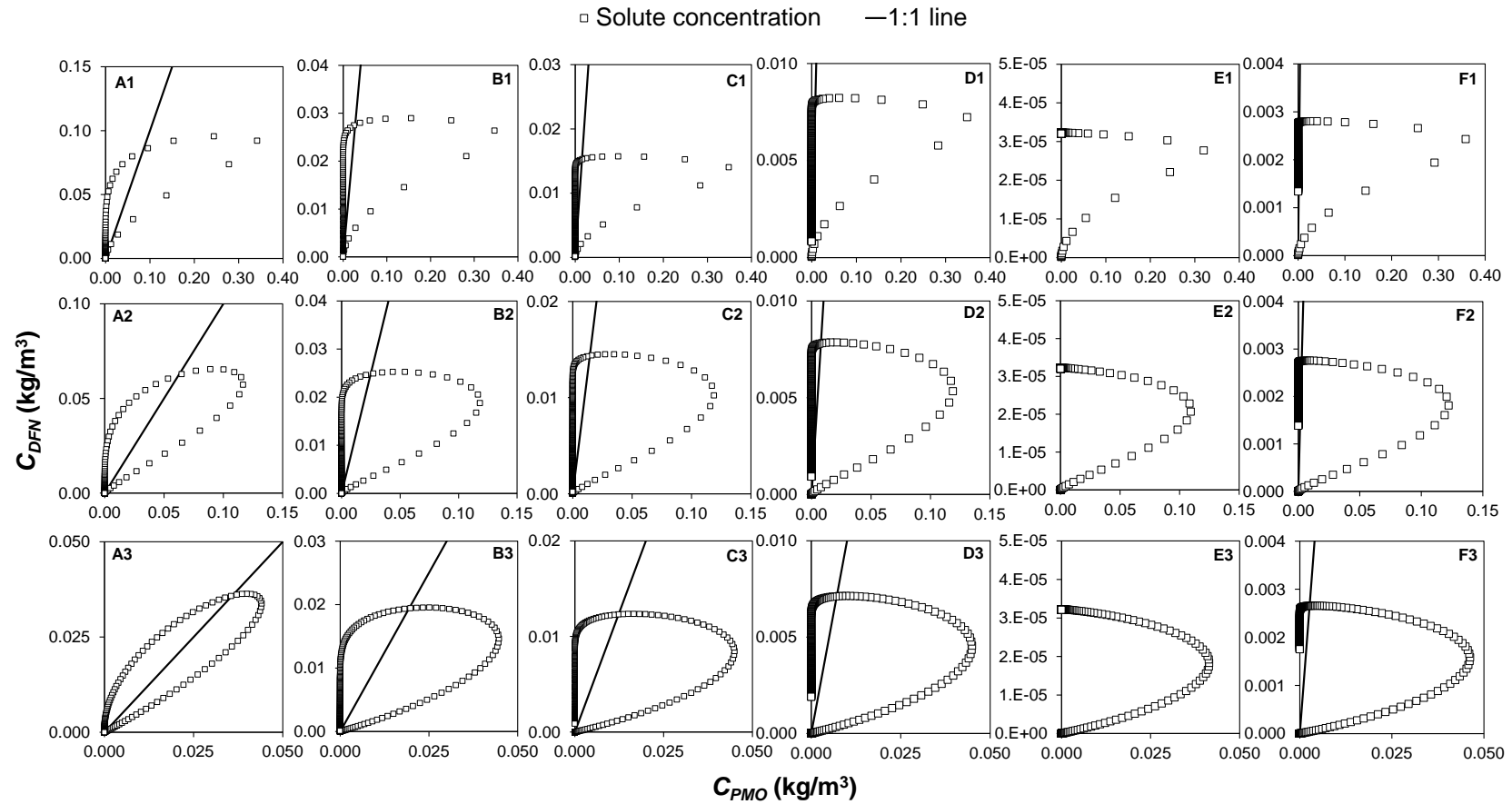


Figure 3.4 shows that in all cases, the PFF causes widening of the solute plume in the region of the aquifer beneath the PFF. This effect becomes more pronounced as the ratio of  $K_m/K_f$  decreases. That is, the solute plumes beneath the PFF are widest in Case E ( $K_m/K_f = 4.9 \times 10^{-6}$ ) and narrowest in Case A ( $K_m/K_f = 2.5 \times 10^{-2}$ ). The solute plumes in Cases D and F have spread to the model boundary ( $x = 1.0$  m) in the region of the aquifer both beneath the PFF and downstream of the plume source, for all Scenarios 1 to 3. Relatively high solute concentrations ( $> 0.01$  kg/m<sup>3</sup>) occur beneath the PFF in Cases A to C ( $K_m/K_f = 2.5 \times 10^{-2}$ ,  $4.9 \times 10^{-3}$  and  $2.4 \times 10^{-3}$ , respectively), and for all scenarios. In Cases D to F ( $K_m/K_f = 1.2 \times 10^{-3}$ ,  $4.9 \times 10^{-6}$  and  $2.0 \times 10^{-4}$ , respectively), plumes beneath the PFF are more dispersed. As the plume crosses the Case E PFF, the degree of dispersion is such that solute concentrations beneath the PFF are below the threshold limit ( $C < 0.001$  kg/m<sup>3</sup>) for visualisation in Figure 3.4. The apparent ‘wobble’ in the green isochlor, and to a lesser degree in the yellow isochlor of Cases C and D (Figure 3.4) is due to minor numerical errors resulting from low concentrations and increasing grid cell sizes beneath the PFF.

Solute concentrations immediately below the PFF in the DFN models ( $C_{DFN}$ ) are compared to solute concentrations in the associated PMO models ( $C_{PMO}$ ) in Figure 3.5.



**Figure 3.5** Comparison of solute concentrations immediately beneath the PFF in the DFN models ( $C_{DFN}$ ) and PMO models ( $C_{PMO}$ ), for all Cases A to F. The 1:1 lines of equality between  $C_{DFN}$  and  $C_{PMO}$  are shown by the solid black lines. Squares above (below) the 1:1 line indicate that the PFF has caused an increase (decrease) in solute concentration compared to the PMO model.

The maximum  $C_{DFN}$  and  $C_{PMO}$  values in Figure 3.5 represent the peak solute concentrations beneath the PFF in the DFN and PMO models, respectively. The 1:1 line, i.e. where  $C_{PMO} = C_{DFN}$ , is illustrated in Figure 3.5 for Cases A to D and Case F. The 1:1 line cannot be illustrated in Case E due the  $x$ - and  $y$ -axes scales that are required for visual inspection of the Case E solute concentrations. Data points that lie above the 1:1 line indicate that  $C_{DFN} > C_{PMO}$  (i.e. the PFF caused increased concentration), whereas data points that lie below the 1:1 line highlight regions where  $C_{DFN} < C_{PMO}$  (i.e. the PFF caused reduced concentration).

The apparent ‘loop’ in the Figure 3.5 plots is caused by the relationship between plume distributions in the DFN and PMO models. The lower arm of each loop represents the region of the plume to the left (i.e. smaller  $x$  coordinates; see Figure 3.3) of the position where the maximum  $C_{PMO}$  occurs. These values lie below the 1:1 line in all cases (Figure 3.5), indicating that the PFF reduces solute concentrations below the PFF, at least for values found to the left of the maximum  $C_{PMO}$  value.

The upper arm of the Figure 5 loops represent values to the right (i.e. a larger  $x$  coordinate; see Figure 3.3) of the peak  $C_{PMO}$  value. The 1:1 line crosses the upper arm, indicating that in this region, the PFF generally causes both lower and higher concentrations relative to the PMO situation. The point where the 1:1 line crosses the upper arm defines the transition from increased to decreased concentrations relative to the PMO case. The increased concentrations (values above the 1:1 line) occur only to the right of the maximum  $C_{PMO}$  value, because the PFF causing displacement (to the right; downstream within the PFF) of the peak concentration

within the plume. There is distinct asymmetry in the functions shown in Figure 3.5 that is also apparent in the solute plumes of Figure 3.4. That is, the plumes have a significantly larger dispersed width to the right of the maximum  $C_{DFN}$  value relative to the width of the dispersion zone to the left of the maximum  $C_{DFN}$  value. This phenomenon has been documented for situations involving low-permeability matrix settings containing complex PFF networks (e.g. Berkowitz and Scher, 1998; Becker and Shapiro, 2000; Reeves et al., 2008).

The curvature of the lines in Figure 3.5 is such that in all cases, the top branch of the loop descends steeply in an almost vertical line towards the origin, demonstrating that the plumes in the DFN models are spread by the PFF into regions of the model domain where  $C_{PMO}$  is negligible. In Cases A to C (i.e.  $K_m/K_f = 2.5 \times 10^{-2}$ ,  $4.9 \times 10^{-3}$  and  $2.4 \times 10^{-3}$ , respectively),  $C_{DFN}$  typically returns to ambient groundwater concentrations (i.e. the origin in Figure 3.5), whereas in Cases D to F (i.e.  $K_m/K_f = 1.2 \times 10^{-3}$ ,  $4.9 \times 10^{-6}$  and  $2.0 \times 10^{-4}$ , respectively), the PFF generally disperses the plume through the entire model domain to the right model boundary (Figure 3.4). As such,  $C_{DFN}$  along the descending arm of the curve (i.e. the top of the loop in Figure 3.5) does not return to ambient groundwater concentration, as is observed for the PMO scenarios. In Case E,  $C_{DFN}$  remains relatively constant at the maximum value ( $3.20 \times 10^{-5}$  to  $3.30 \times 10^{-5}$  kg/m<sup>3</sup>) such that the upper limb of the curve does not descend towards the origin, as is observed for all other cases. That is, the PFF in Cases E and F dominates completely the transport of solutes, such that only low concentrations occur in the matrix beneath the PFF, notwithstanding the possibility of boundary effects on Case E DFN concentrations.

The Figure 3.5 results illustrate that solute concentrations in the DFN models are closer to the PMO model concentrations when the plume reaching the PFF is more dispersed. That is, the difference between the DFN and PMO solutions is greatest in Scenario 1 for all cases. This is demonstrated in Figure 3.5 (for all cases except Case E, where  $K_m/K_f = 4.9 \times 10^{-6}$ ), whereby the model data ‘rotates’ about the 1:1 line (not visible for Case E) from Scenario 1 to Scenario 3, in which the 1:1 line is closer to passing through the maximum  $C_{PMO}$  value. The data points are more symmetrically distributed around the 1:1 line in Scenario 3, compared with Scenarios 1 and 2. This pattern is quantified by the root-mean-square errors (RMSEs) of solute concentrations beneath the PFF in the DFN models versus PMO values, given in Table 3.2. Cases E is omitted from Table 3.2 because the Case E solute plumes extend laterally beyond the model boundaries, and therefore, the RMSE values are not informative. Case F ( $K_m/K_f = 2.0 \times 10^{-4}$ ) plumes are also in contact with the model boundary, and therefore the Case F RMSE should be treated with caution. Nonetheless, the RMSEs in Table 3.2 provide a quantitative measure of the enhanced effect of a PFF on the solute distribution in a permeable matrix as  $K_m/K_f$  decreases (from Case A to Case F, with the exception of Case E).

**Table 3.2** Root-mean-square errors for solute concentrations beneath the PFF in the DFN models, relative to PMO model values.

Scenario	RMSE (kg/m <sup>3</sup> )				
	Case A	Case B	Case C	Case D	Case F
1	0.019	0.025	0.026	0.027	0.028
2	0.009	0.015	0.016	0.016	0.017
3	0.004	0.008	0.009	0.010	0.011

### 3.4.2 Quantification of PFF effects on solute plume characteristics below the PFF

Figure 3.6 illustrates the key solute plume metrics: (a) displacement of the peak solute concentration ( $D$ ), i.e. the distance that peak solutes ( $C_{DFN}$  and  $C_{PMO}$ ) are offset in the direction perpendicular to flow, as shown in Figure 3.2, (b) ratio of DFN and PMO peak concentrations beneath the PFF (i.e. at  $z = 49.975$  cm) ( $C_{Dmax}/C_{Pmax}$ ), (c) ratio of DFN and PMO solute plume widths below the PFF ( $W_{DFN}/W_{PMO}$ ), and (d) plume asymmetry ratio ( $W_L/W_R$ ), i.e. the ratio of the width of the solute plume to the left of the maximum  $C_{DFN}$  to the width of the solute plume to the right of the maximum  $C_{DFN}$ . Plume width and symmetry are analysed along the alignment of the PFF (i.e. at  $45^\circ$  relative to the primary flow direction), and therefore,  $W_L/W_R < 1$  even for PMO cases, in which plumes are symmetric perpendicular to the flow direction.  $W_{DFN}/W_{PMO}$  and  $W_L/W_R$  could not be obtained for Case E because solute concentrations beneath the PFF are too low (i.e.  $C = < 0.001$  kg/m<sup>3</sup>) to obtain a value for  $W_{PFF}$ . Case F is omitted from Figure 3.6 because the smaller  $2b$  and  $\theta$  precludes direct comparison with other cases.

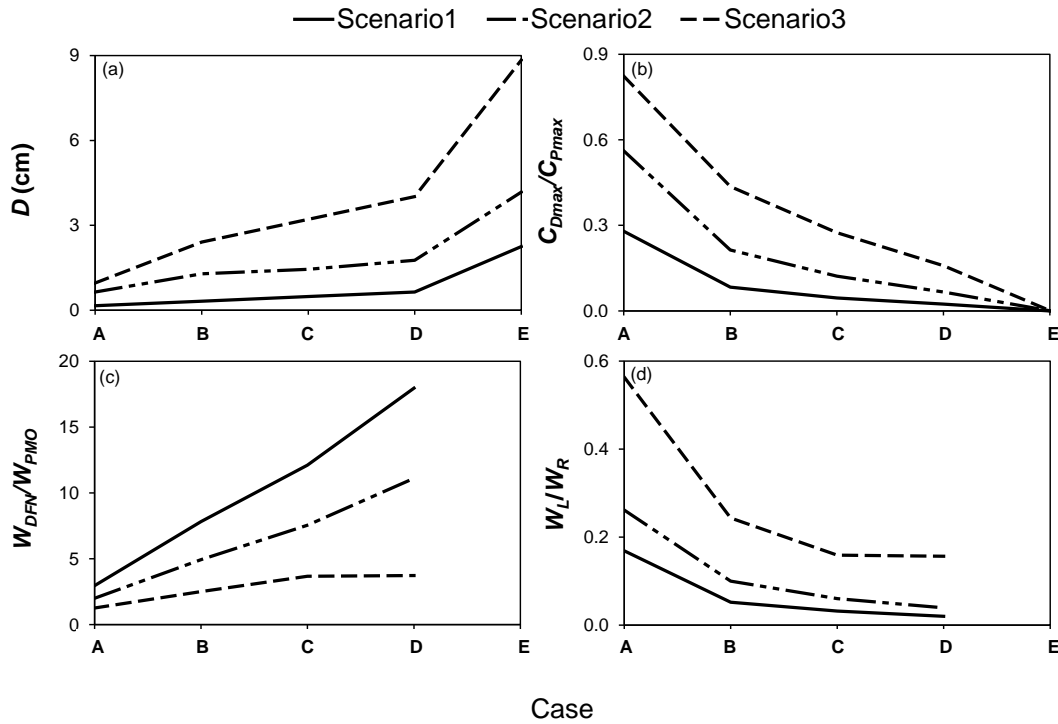


**Figure 3.6** Influence of  $K_m/K_f$  on: (a)  $D$ , (b)  $C_{Dmax}/C_{Pmax}$  below the PFF, (c)  $W_{DFN}/W_{PMO}$ , and (d)  $W_L/W_R$ , for Cases A to E.

Figure 3.6a shows that displacement of the peak solute concentration ( $D$ ) increases as  $K_m/K_f$  decreases (i.e. from Case A to E) and for more dispersed plumes (i.e. from Scenario 1 to 3). For example, the ratio of plume displacement in Scenarios 1 and 3 (i.e.  $D_1/D_3$ ) ranges from 0.13 in Case B, to 0.25 for Case E. This result indicates that  $D_1 < D_3$ , for all cases.  $D_1/D_3$  typically increases as  $K_m/K_f$  decreases. An exception is found in Case A (i.e.  $K_m/K_f = 2.5 \times 10^{-2}$ ), where  $D_1/D_3 = 0.17$ , i.e. the ratio is larger than for Case B (0.13). For Case F (not included in Figure 3.6), displacement of the peak solute concentration in all scenarios is greater than in Cases A to D, and less than Case E.  $D$  ranges from 0.96 cm (Scenario F1) to 5.14 cm (Scenario F3), i.e. between 0.43 and 6.0 times the  $D$  of the corresponding plumes in Cases A to E.

Attenuation of the peak solute concentration, caused by the PFF (i.e.  $C_{Dmax}/C_{Pmax}$ ), is illustrated in Figure 3.6b for Cases A to E. Attenuation increases from Case A to E (i.e. as  $K_m/K_f$  decreases) and from Scenario 3 to Scenario 1 (i.e. from more dispersed to less dispersed plumes). That is, the maximum solute concentrations in the DFN models range from one order of magnitude smaller (e.g. Case A, Scenarios B1 and B2, Scenarios C1 and C2) to four orders of magnitude smaller (e.g. Scenarios E1 and E2) than the corresponding PMO models. Within each case, attenuation of the peak solute concentration ( $C_{Dmax}/C_{Pmax}$ ) is largest for Scenario 1 (i.e. Scenario A1 (0.28) to Scenario D1 (0.02)) In Case E,  $C_{Dmax}/C_{Pmax}$  is uniform for all scenarios ( $< 0.001$ ), because  $C_{Dmax}$  is negligible. These results demonstrate that the PFF has a greater effect on attenuation when solute plumes passing through a PFF are less dispersed. For Case F (not shown in Figure 3.6b), transects along  $z = 49.975$  cm lie a distance  $b$  (i.e. half the PFF aperture) away from the edge of the PFF. Attenuation in Case F is greater than in Cases A to D (i.e. because  $K_m/K_f$  is smaller), and is less than Case E (i.e. where  $K_m/K_f$  is larger). Similar to Cases A to E, the greatest attenuation is observed for Scenario F1 ( $C_{Dmax}/C_{Pmax} = 0.01$ ).

Figure 3.6c illustrates the width of the solute plumes beneath the PFF in the DFN models compared to the associated PMO model (i.e.  $W_{DFN}/W_{PMO}$ ). Plume widening is largest for smaller values of  $K_m/K_f$  (i.e. Cases D and F). That is, the influence of the PFF on solute plume spreading increases as  $K_m/K_f$  decreases. Within each case, plume widening is largest for less dispersed plumes (i.e. Scenarios A1, B1, C1, etc.). For example, the plume width ratio ( $W_{DFN}/W_{PMO}$ ) is greatest in Scenarios A1 (2.95), B1 (7.83), C1 (12.11) and D1 (17.96) and decreases by between 20.8% and 42.6% to 1.26 (A3), 2.50 (B3), 3.67 (C3) and 3.73 (D3). These results demonstrate

that the deviation of the DFN and PMO solute plume widths in Cases A to D decreases as the concentration of the solute plume decreases. The influence of the PFF on plume spreading in Case F (not shown in Figure 3.6c) is greater than in Cases A to D. Here, the plume width ratio ranges from  $W_{DFN}/W_{PMO} = 3.58$  (Scenario F3) to 19.32 (Scenario F1), i.e. plume widening in Scenario F3 is 18.5% of the plume widening in Scenario F1.

Plume asymmetry (i.e.  $W_L/W_R$ ) for Cases A to D is illustrated in Figure 3.6d. Solute distributions immediately beneath the PFF are skewed to the right in all cases (i.e.  $W_R > W_L$ ) such that the plume asymmetry ratio is always  $< 1$ . Within each scenario, a greater degree of asymmetry is imparted in more dispersed plumes (i.e. Scenarios D1, D2, D3, etc.). That is, for Scenarios A1 to D1 and F1 (Case F not shown in Figure 3.6d),  $W_R$  is between 5.9 and 58.2 times larger than  $W_L$ , and for Scenarios A3 to F3,  $W_R$  is between 1.8 and 6.9 times larger than  $W_L$ . The results obtained for Scenario D3 and Case F are likely inaccurate because the  $C = 0.001 \text{ kg/m}^3$  isochlor intercepts the right model boundary and hence, values for  $W_R$  may be underestimated.

Table 3.3 provides the results of a sensitivity analysis evaluating the effects of PFF orientation on the four key solute plume metrics illustrated in Figure 3.6. Scenario C2 ( $K_m/K_f = 2.4 \times 10^{-3}$ ) was chosen for the analysis because the C2 plume in the scenarios adopting  $45^\circ$  flow does not intercept the model boundary, and the rock matrix in Case C has intermediate permeability relative to the other simulated cases. Two additional PFF orientations were considered: (1)  $40^\circ$  relative to the primary flow direction, and (2)  $60^\circ$  relative to the primary flow direction.  $W_{DFN}/W_{PMO}$  and

$W_L/W_R$  could not be obtained for the 60° PFF because the solute plume intercepts the right model boundary.

**Table 3.3** Solute plume metrics for Scenario C2 with varied PFF orientation.

PFF orientatio n (°)	Plume metric			
	$D$ (cm)	$C_{Dmax}/C_{Pma}$ $x$ (-)	$W_{DFN}/W_{PM}$ $o$ (-)	$W_L/W_R$ (-)
40	1.12	0.13	7.43	0.08
45	1.45	0.12	7.54	0.06
60	2.73	0.12	-	-

The results in Table 3.3 demonstrate that PFF effects on solute plumes are generally more pronounced as the angle of the PFF increases (i.e. the orientation of the PFF approaches the flow direction). For example, the 60° PFF causes a greater displacement of the peak solute concentration ( $D = 2.73$  cm) compared to the 40° and 45° PFFs ( $D = 1.12$  cm and 1.45 cm, respectively). Table 3.3 also shows that the peak concentration of a plume passing through a 60° or 45° PFF is likely to be slightly more attenuated than a plume passing through a 40° PFF. Further, plumes passing through a 45° PFF are likely to be wider and less symmetrical than plumes passing through a 40° PFF.

### 3.4.3 Quantification of PFF effects on solute plume characteristics above the PFF

For all cases explored in this study, solute distributions near the plume source are in good agreement with the solute distributions in the PMO scenarios (not shown here for brevity). That is, the plumes in the DFN case behave as if they were travelling through a homogeneous porous medium for most of the flow distance between the solute source and the PFF, i.e. following Equation (3.2). Scenario 1 in each case is an exception to this, because the plume source is located very close

(0.4125 cm) to the PFF, compared with Scenarios 2 and 3. As the plume approaches the top edge of the PFF (e.g.  $50.0 \text{ cm} < z < 51.5 \text{ cm}$  in Scenario 2), the solute concentrations in the DFN models deviate substantially from the equivalent PMO models. Figure 3.7 demonstrates the effect of the PFF on solute distributions above the PFF in Scenario A2 ( $K_m/K_f = 2.5 \times 10^{-2}$ ). DFN and PMO model solute breakthrough curves are given at: (a)  $z = 51.250 \text{ cm}$ , (b)  $z = 50.625 \text{ cm}$ , (c)  $z = 50.413 \text{ cm}$ , and (d)  $z = 50.025 \text{ cm}$ .

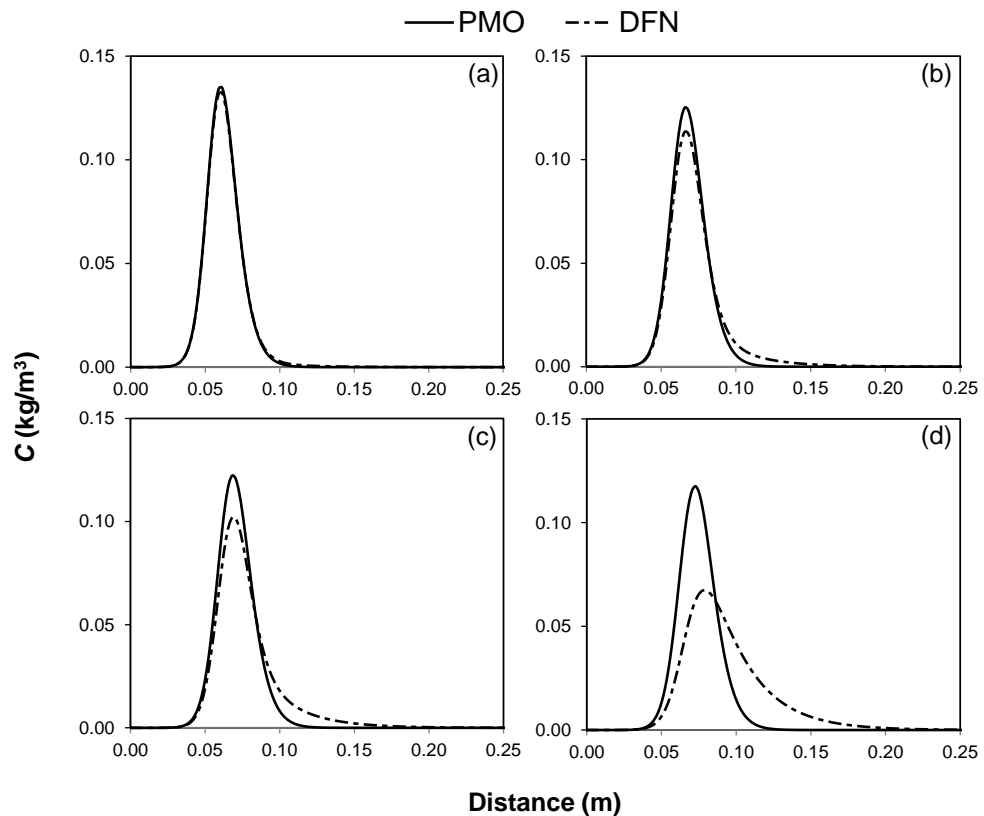


**Figure 3.7** Scenario A2 ( $K_m/K_f = 2.5 \times 10^{-2}$ ) solute concentrations above the PFF in the PMO model (solid black lines) and DFN model (dashed black lines). Solute concentrations are obtained at: (a)  $z = 51.250 \text{ cm}$ , (b)  $z = 50.625 \text{ cm}$ , (c)  $z = 50.413 \text{ cm}$ , and (d)  $z = 50.025 \text{ cm}$ .

Figure 3.7a shows a near perfect agreement between the DFN and PMO solute concentrations, highlighting the minimum distance above the PFF where solute concentrations are not influenced by the PFF. Figures 3.7b to 3.7d demonstrate

progressively stronger up-gradient effects of the PFF on the plume as it approaches the PFF. The attenuation of the plume includes a shift in the DFN peak concentration ( $C_{Dmax}$ ) to the right, and a reduction in  $C_{Dmax}$  to 57% of the maximum PMO concentration ( $C_{Dmax} = 0.067 \text{ kg/m}^3$  and  $C_{Pmax} = 0.118 \text{ kg/m}^3$ ). The up-gradient effects of the PFF also include enhanced asymmetry in the DFN case.

### **3.5 Discussion**

Previous research into solute transport in permeable rock formations containing PF features (e.g. Birkhölzer et al. 1993a; 1993b; Odling and Roden, 1997) is extended in this study by quantifying the displacement and spreading of solute plumes passing through a PFF, and linking these to the main parameters of our idealised setting. This methodology allows for an examination of the effects of an individual PFF that are otherwise difficult to ascertain within the multi-PFF models of previous studies. The impact of a PFF on solute plume distributions resulting from the current study were similar to some of the findings from Odling and Roden (1997), who examined solute transport in natural PFF network geometries embedded within a permeable matrix. For example, both studies demonstrate that PFFs in permeable rock formations can enhance solute transport and dispersion within the rock matrix and thus, in both cases, a significant portion of the solute may reside within the matrix. In the current study, solute plumes in all Cases A to F were displaced to varying degrees, and the lateral extents of the plumes were greater than those in PMO rock matrices. Odling and Roden (1997) did not examine the effect of PFFs on solute plume displacement, and thus, to the best of the authors' knowledge, this is the first numerical study to consider PFF effects on solute plume

displacement in permeable rock matrices. Such effects are probably more complex and widespread in real-world permeable rock aquifers, because PFFs usually occur as interconnected networks. Nonetheless, the results here identify key relationships between PFF effects and plume responses that have otherwise not been studied.

For the conceptual models considered here, large values of  $K_m/K_f$  (Case A) resulted in small values for  $D$  (0.16 cm to 0.96 cm), in comparison to smaller values of  $K_m/K_f$  (i.e. Cases B to F). This result is expected, and can be explained in part by the refraction of flow lines (i.e. the change in flow direction due to a change in velocity). Refraction of a groundwater flow path will occur as water passes from one stratum to another with a different hydraulic conductivity (e.g. from the porous matrix to a PFF) (Hubbert, 1940). The change in flow direction is dependent on the *angle of incidence* (i.e. the angle between normal at the boundary and the incoming streamline ( $\sigma_1$ ;  $45^\circ$  in the current study); Kresic, 1997) and the ratio of the two strata hydraulic conductivities ( $K_1$  and  $K_2$ ), given as (Fetter, 2001):

$$\frac{K_1}{K_2} = \frac{\tan \sigma_1}{\tan \sigma_2} \quad (3.3)$$

where  $\sigma_2$  [radians] is the *angle of refraction* (i.e. the angle between normal at the boundary and the outgoing streamline). In the current study,  $K_1/K_2 = K_m/K_f$ . Thus, Equation (3.3) suggests that, where  $K_m/K_f$  is closer to unity, the difference between  $\sigma_1$  and  $\sigma_2$  is smaller, leading to less displacement of the flow line. Conversely, decreasing  $K_m/K_f$  will produce more flow line displacement, and consequently larger values of  $D$ . This concept is supported by the increasing trend in  $D$  obtained from Case A (largest  $K_m/K_f$ ) to Case E (smallest  $K_m/K_f$ ).

Additional simulations that are modified forms of Scenario C2, with 60° and 40° PFF orientations, indicate that more oblique plumes (larger values of  $\sigma_1$ ) produce greater displacement (larger  $D$ ). Larger flow line displacement is expected when the difference in  $\sigma_1$  and  $\sigma_2$  (i.e. the flow line deviation) is greatest. The flow line deviation is  $|\sigma_2 - \sigma_1|$ . Considering Equation (3.3), this becomes  $|\sigma_2 - \tan^{-1}(K_m/K_f \tan \sigma_2)|$ , which increases monotonically with  $\sigma_2$  ( $0 \leq \sigma_2 \leq 90^\circ$ ). Thus, flow line refraction is likely the primary cause of greater peak concentration displacement ( $D$ ) with increasing obliqueness of the PFF relative to the flow line.

$D$  was also found to vary in response to the degree of dispersion of the solute plume as it passes through the PFF. That is, for all Cases A to F, less dispersed plumes passing through the PFF (i.e. Scenarios A1 to F1) are displaced to a lesser degree than their more dispersed counterparts (i.e. Scenarios A2 to F2 and A3 to F3). Equation (3.2) implies that solute concentrations directly above the matrix-PFF interface increase as PFFs are located closer to the source. In Scenarios A1 to F1, the concentration gradients between the PFF and the matrix are therefore steeper than in Scenarios A2 to F2 and A3 to F3, because there is a greater variation between the incoming plume concentration and the incoming (fresh) groundwater concentration inside the PFF. The dispersive flux is proportional to the concentration gradient, according to Fick's law for diffusion (Domenico and Schwartz, 1998), and hence, as the concentration gradient increases, solutes are moved via dispersive transport more rapidly between the PFF and the rock matrix. It follows that the more dispersed plumes in Scenarios A3 to F3 produce smaller concentration gradients and lower dispersive fluxes, which cause solutes to remain inside the PFF for longer distances.

It is worthwhile to note that the displacement of the plume's centre of mass should be unaffected by the degree of dispersion of the plume as it passes through the PFF, following theory presented by Kitanidis (1988) and others. This is tested by considering the centres of mass of plumes passing through the PFFs in Case C, which were found to be displaced by 13.2 cm ( $\pm 1.1$  cm). That is, the displacement of the plumes' centres of mass varied by  $< 9\%$  (relative to the average displacement) between Scenarios C1 to C3, whereas the displacement of the peak concentration differed by up to 88% between Scenarios C1 to C3.

Maximum solute concentrations immediately beneath the PFF were found to be higher, relative to the associated PMO model (i.e.  $C_{Dmax}/C_{Pmax}$ ; see Figure 3.6b), in aquifers characterised by larger  $K_m/K_f$  ratios (e.g. Case A). This is because the smaller deviation of flow lines for higher  $K_m/K_f$  ratios results in shorter distances of flow within PFFs, and subsequently the plumes are less dispersed on exit, leading to weaker attenuation of peak concentrations. In a similar manner, aquifers characterised by larger  $K_m/K_f$  ratios were found to produce narrower solute plumes.

Figure 3.8 illustrates the plume widening effect of the PFF in Cases A, B and C, given in terms of the length of matrix material required to produce a solute plume with an equivalent width to that of the PFF scenario. That is, we used the Wilson and Miller (1978) solution to determine the plume travel distance (through the matrix) required to create the same plume widening as caused by the PFF. Cases D to F are not included because in the majority of scenarios, the  $C = 0.001$  kg/m<sup>3</sup> isochlor intercepted the right model boundary and hence the effect of the PFF on

the width of the solute plumes may be underestimated. The matrix-PFF ratio is given in terms of  $(K_m/K_f)^{-1}$  to highlight the linearity in the Figure 3.8 relationship.

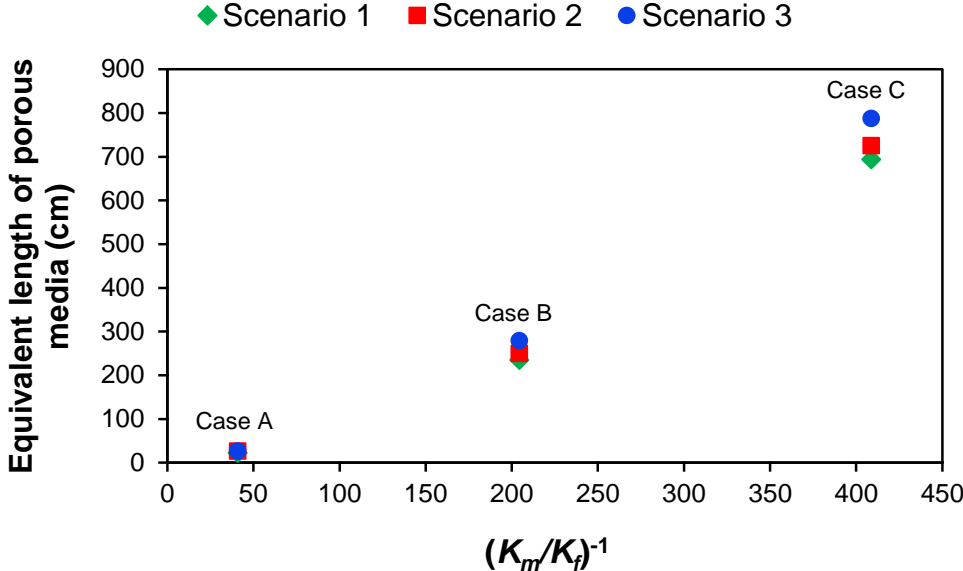


**Figure 3.8** Equivalent length of porous media required to reproduce the solute plume widths in Cases A ( $K_m/K_f = 2.5 \times 10^{-2}$ ), B ( $K_m/K_f = 4.9 \times 10^{-3}$ ) and C ( $K_m/K_f = 2.4 \times 10^{-3}$ ).

Figure 3.8 shows an almost linear increase in the equivalent length of homogeneous porous media required to produce the same degree of plume widening as the PFF in Cases A, B and C. Figure 3.8 highlights the considerable influence of the PFF on solute plume widths in Cases A to C, and demonstrates that the degree of spreading caused by a PFF, with an aperture of 0.5 mm, is similar to the dispersive effect of up to several metres of matrix material. We therefore anticipate that in most permeable rock matrices containing PFFs, whereby PFF spacing is less than several metres, the PFFs rather than the matrix material will dominate the spreading of solute plumes.

For all cases explored in this study, solute distributions are strongly asymmetric immediately beneath the PFF. For cases with larger contrasts between  $K_m$  and  $K_f$  (i.e. smaller  $K_m/K_f$  ratios), flow lines converge more closely at the matrix-PFF interface than for cases with larger  $K_m/K_f$  ratios (noting that flow lines diverge on re-entry into the matrix). Therefore, flow lines inside the PFF are closer together (perpendicular to each other) than in the rock matrix. Dense flow lines enhance transverse dispersion (e.g. Werth et al., 2006; Cirpka et al., 2011), and the travel distance within the PFF also increases for these cases. Solutes that disperse to the left of the main plume trajectory have a shorter path to exit the PFF and thus, are transversely dispersed less than those that disperse to the right. As such, the breakthrough of the plume at the PFF exit has enhanced asymmetry relative to PMO simulations. More dispersed plumes produce smaller concentration gradients between the matrix and PFF, leading to lower dispersive fluxes, which cause solutes to remain inside the PFF for longer distances, which enhances the plume's asymmetry. The enhancement of plume asymmetry caused by the PFF starts above the PFF, as is shown in Figure 3.7.

It is hypothesised that the changes to the plume concentrations above the PFF (indicated in Figure 3.7) is potentially the consequence of a non-physical artefact of the advection-dispersion equation; a process we refer to as numerical 'back dispersion'. That is, enhanced solute concentrations occur upstream of the PFF, i.e. within the matrix and against the direction of flow, because the direction of the concentration gradient drives solutes in the opposite direction to the flow. Back dispersion was also observed in the traditional form of the Henry (1964) seawater intrusion problem by Segol et al. (1975) and Frind (1982), who attributed it to the

fixed concentration sea boundary condition. Henry's original sea boundary condition required an abrupt change from freshwater to seawater without dilution of the seawater outside the exit boundary (Frind, 1982). In our case, as solutes travel along the PFF, the concentration inside the PFF is greater than the solute concentration in the matrix above the PFF (i.e. upstream), and as such, solutes will disperse back into the matrix in the upstream flow direction and in the solute down-gradient direction. Further testing is required to ascertain whether or not this is a physical process or a non-physical artefact of the numerical model, as was observed for the Henry (1964) problem by Segol et al. (1975) and Frind (1982).

### **3.6 Conclusions**

In this study, the influence of a single, discrete PFF on the displacement and spreading of solute plumes in permeable rock matrices is investigated. We examine the steady-state distribution of solutes in sedimentary rocks aquifers with moderate-to-high matrix permeability (e.g. sandstone and limestone), where solute plumes pass through a PFF representing a medium-sized fracture. The simulation results presented here provide important insights into the individual effect of a PFF. The key findings of this study are:

- 1) Peak concentrations of plumes passing through a PFF embedded in a permeable rock matrix will be displaced to varying degrees, depending on  $K_m/K_f$  and the concentration of the plume as it encounters the PFF. Peak concentrations of plumes crossing a PFF under high  $K_m/K_f$  conditions will be displaced a smaller distance than those under lower  $K_m/K_f$  conditions.

Furthermore, the peak concentrations in more dilute plumes passing through a PFF will be displaced to a larger degree than more concentrated plumes.

- 2) Medium-sized PFFs in moderately permeable matrices (i.e. cases in the current study characterised by lower  $K_m/K_f$  ratios, such as Case E) may dilute solute concentrations immediately beneath the PFF to < 1% of the solute concentration at the same location in associated PMO scenarios. Potential implications may therefore arise for contaminant spreading in permeable rock matrices containing networks of PFFs, where such substantial dilutions of solute plumes are achieved.
- 3) Solute concentrations beneath a PFF are likely to be lower, and the plume is likely to be wider, than in a permeable, homogeneous porous medium. These effects are greater for lower values of  $K_m/K_f$ . Solute distributions are likely to be more asymmetric and attenuated when solute plumes encountering a PFF are less dispersed. In permeable rock matrices containing PFFs, whereby PFF spacing is less than several metres, the PFFs (rather than the matrix material) will likely dominate the spreading of solute plumes.
- 4) PFF effects on solute plumes are likely to be more pronounced in cases where the angle of the PFF approaches the flow direction. That is, the peak solute concentration of a plume passing through a PFF is likely to be displaced further in cases where the angle of incidence is large. In these cases, solute plumes are also likely to be wider, more attenuated, and less symmetrical.
- 5) As solute plumes approach the PFF, and reach a critical distance above the PFF (approximately 1 cm for the cases explored in this study), solute

concentrations above the PFF in the DFN models are higher than in the PMO models. We hypothesise that this may be a non-physical phenomenon that is the result of ‘back dispersion’, which we suggest is an artefact of the advection-dispersion equation that has been observed in seawater intrusion studies, and that warrants further analysis.

The individual effect of a single PFF embedded in a moderate-to-high permeability rock matrix has been demonstrated for a range of aquifer conditions. In real-world permeable rock aquifers, networks of interconnected PFFs are more likely to occur and as such, the PFF effects demonstrated by the current study will be more complex and widespread. The results indicate that PFFs can have a substantial influence on the distribution of solutes in permeable rock matrices. Solute concentrations in such aquifers may be overestimated if only the hydraulic properties of the porous matrix are considered. Similarly, the lateral extents of solute plumes may be largely underestimated if individual PFFs are not accounted for explicitly in numerical models.

## Chapter 4

### 4. On the effects of preferential or barrier flow features on solute plumes in permeable porous media

*This chapter is based on the following published paper:*

Sebben, M. L., Werner, A. D., 2016b. On the effects of preferential or barrier flow features on solute plumes in permeable porous media. *Adv. Water Resour.* 98, 32-46, doi: 10.1016/j.advwatres.2016.10.011.

#### 4.1 Abstract

Despite that discrete flow features (DFFs, e.g. fractures and faults) are common features in the subsurface, few studies have explored the influence of DFFs on solute plumes in otherwise permeable rocks (e.g. sandstone, limestone), compared to low-permeability rock settings (e.g. granite and basalt). DFFs can provide preferential flow pathways (i.e. ‘preferential flow features’; PFFs), or can act to impede flow (i.e. ‘barrier flow features’; BFFs). This research uses a simple analytical expression and numerical modelling to explore how a single DFF influences the distribution of solute plumes in permeable aquifers. The analysis quantifies the displacement and widening (or narrowing) of a steady-state solute plume as it passes through a DFF in idealised,  $1 \times 1$  m moderately permeable rock aquifers. Previous research is extended by accounting for DFFs as 2D flow features, and including BFF situations. A range of matrix-DFF permeability ratios (0.01 to 100) and DFF apertures (0.25 mm to 2 cm), typical of sedimentary aquifers containing medium-to-large fractures, are considered. The results indicate that for

the conceptual models considered here, PFFs typically have a more significant influence on plume distributions than BFFs, and the impact of DFFs on solute plumes generally increases with increasing aperture. For example, displacement of peak solute concentration caused by DFFs exceeds 20 cm in some PFF cases, compared to a maximum of 0.64 cm in BFF cases. PFFs widen plumes up to 9.7 times, compared to a maximum plume widening of 2.0 times in BFF cases. Plumes passing through a PFF are less symmetrical, and peak solute concentrations beneath PFFs are up to two orders of magnitude lower than plumes in BFF cases. This study extends current knowledge of the attenuating influence of DFFs in otherwise permeable rocks on solute plume characteristics, through evaluation of 2D flow effects in DFFs for a variety of DFF apertures, and by considering BFF situations.

## **4.2 Introduction**

Discrete flow features (DFFs) such as fractures, faults, sand lenses and clay layers are common geologic features in groundwater systems. DFFs can provide preferential pathways (i.e. ‘preferential flow features’; PFFs) or act as barriers (i.e. ‘barrier flow features’, BFFs) to fluid flow and solute transport. DFFs are common in rock aquifers where the parent rock permeability ranges from virtually impermeable (e.g. granite and basalt) to permeable (e.g. sandstone and limestone). Considerably less research attention has been paid to the role of PFFs in modifying groundwater flow and solute transport in permeable rock aquifers, compared to low-permeability rocks (Rubin et al., 1997; Odling and Roden, 1997). The influence of BFFs has been studied to a lesser degree than PFFs. Nonetheless, previous studies of low-permeability rocks (e.g. Thoma et al., 1992; Kessler and Hunt, 1994)

have shown that fluid flow and solute transport can be altered significantly by the restrictions to flow caused by BFFs.

Solute transport in low-permeability rocks containing PFFs typically occurs via solute advection and mechanical dispersion within the PFF only, and exchanges between PFFs and the rock matrix occur by molecular diffusion (e.g. Grisak and Pickens, 1981; Sudicky and Frind, 1982). However, in permeable rock aquifers containing PFFs, solute transport more likely occurs via advection, mechanical dispersion and molecular diffusion in both the PFF and the rock matrix (Birkhölzer et al., 1993a). Hence, consideration of these transport processes is required to ascertain the impacts of PFFs on solute transport in otherwise permeable rocks.

Previous studies of solute transport in permeable rocks containing PFFs include Birkhölzer et al. (1993b), Rubin and Buddemeier (1996), Odling and Roden (1997), Houseworth et al. (2013), Willmann et al. (2013), Sebben et al. (2015) and Sebben and Werner (2016). Birkhölzer et al. (1993b) examined solute transport in fractured rock formations and found that solute transport in permeable rocks containing parallel, equidistant PFFs with uniform aperture can be represented using the equivalent porous media (EPM) approach (i.e. PFFs are not incorporated explicitly into the model) if the representative elementary volume of the network is large enough. Rubin and Buddemeier (1996) found that the ratio of transverse to longitudinal dispersivity that is required to reproduce contaminant distributions in an EPM model is sensitive to the orientation of the PFF. Odling and Roden (1997) used numerical modelling to study 2D flow and solute transport in permeable rocks containing naturally occurring PFF geometries. They concluded that the orientation

and density of PFFs can be as influential as PFF connectivity on contaminant transport rates and solute plume heterogeneity. However, the effect of transport processes at the scale of an individual PFF was not considered, and therefore the key factors driving solute transport within their PFF networks were not revealed, despite that these small-scale processes can influence solute transport at larger scales (Grisak and Pickens, 1980).

Houseworth et al. (2013) obtained a closed-form analytical solution for solute transport during steady-state saturated flow in a single PFF embedded within a porous, permeable rock matrix. The authors incorporated several factors not previously included in analytical solutions for comparable transport problems, including 2D flow in the matrix and a general solute source position. Houseworth et al. (2013) considered the case where advective velocities in the matrix are sufficiently small that matrix diffusion dominates in comparison to matrix dispersion. Hence, the effect of a PFF on a solute plume in a matrix that is subjected to both advection and dispersion remains unexplored. Willmann et al. (2013) developed a particle-tracking method that accounts for advection and diffusion explicitly in both the PFFs and surrounding matrix. Mass exchanges from the PFF into the matrix are dependent on the advective flux perpendicular to the matrix, the PFF aperture, and the diffusive component. The authors recommended further research to ascertain whether a transport-related PFF aperture should be used in preference to the hydraulic aperture.

The influence of simple PFF network geometries on seawater intrusion in otherwise permeable coastal aquifers was examined by Sebben et al. (2015). They employed

discrete fracture network (DFN) modelling to demonstrate that PFFs can either widen or narrow the seawater wedge relative to homogenous porous media formations, depending on the location and orientation of the PFFs. Sebben et al. (2015) describe PFF effects on seawater intrusion at the macro-scale; however, the complex effects of heterogeneities on the density-dependent flow field precluded examination of the mechanisms that underlie solute plume widening (or narrowing) as it passes through an individual PFF. Sebben and Werner (2016) used DFN modelling to explore the influence of a single PFF on the distribution of solutes in moderate-to-high permeability rock matrices ( $10^{-6}$  m/s to  $10^{-3}$  m/s, e.g. sandstone and limestone). Numerical simulations were performed to investigate PFF effects on a 2D solute plume under steady-state groundwater flow conditions. Their study considered the influence of PFFs that represent medium-sized fractures (0.25 mm to 0.5 mm fracture aperture). Further, PFFs were assumed to be fully mixed, open channels (i.e. flow through PFFs was calculated according to the cubic law (Berkowitz, 2002; Graf and Therrien, 2007)) that can be treated as 1D flow features. The authors found that the degree of spreading that occurs when solute plumes pass through medium-sized PFFs in moderate-to-high permeability matrices is highly dependent on the ratio of the matrix hydraulic conductivity ( $K_m$ ) to the hydraulic conductivity of the PFF ( $K_f$ ), and on the concentration of the plume where it encounters the PFF. In cases with low  $K_m/K_f$  values, PFFs were found to dilute solute plumes by factors of greater than 100.

Sebben and Werner (2016) encountered seemingly anomalous behaviour arising out of the advection-dispersion equation in the form of higher-than-expected solute concentrations up-gradient of the PFF. It is hypothesised that these are non-physical

effects attributable to ‘back dispersion’ (termed ‘upstream dispersion’ by Konikow (2011)), which is the anomalous movement of solutes from the PFF back into the matrix against the direction of groundwater flow. Back dispersion has been recognised by Al-Niami and Rushton (1977), Marino (1978) and Kumar (1983). In reality, dispersion of solutes in opposition to the flow of groundwater is expected only in low-permeability sediments, where solute transport by molecular diffusion may exceed advective transport rates (e.g. Grisak and Pickens, 1980; Harrison et al., 1992). It is likely that this effect is not physically realistic for the PFF situations examined by Sebben and Werner (2016), given the moderate-to-high permeability of the rock matrices considered. Back dispersion has also been observed previously in numerical investigations of seawater intrusion (e.g. Segol et al., 1975; Frind, 1982), solute transport in aquifers containing structured heterogeneities (e.g. Liu et al., 2014), and surface-subsurface solute exchanges in hillslope settings (e.g. Liggett et al., 2014). Presently, there is no guidance on the extent of errors in solute predictions for situations where back dispersion is thought to have impacted modelling results. Further analyses were recommended by Sebben and Werner (2016) to ascertain the extent to which back dispersion adversely impacts the results of numerical experiments of DFF situations.

In some cases, DFFs contain material that is less permeable than the host rock, and hence, form BFFs (e.g. Laubach, 2003; Bense and Person, 2006). For example, fractures may be partially or completely clogged as a result of mineral deposition formed by weathering reactions (e.g. Thoma et al., 1992; Kessler and Hunt, 1994). Previous studies of BFFs in permeable rock matrices have focussed primarily on characterising the flow regime rather than solute transport processes. For example,

Antonelli and Aydin (1994) used mini-permeameters and image analysis to characterise the porosity and permeability of fault zones in sandstone outcrops. They found that low-permeability deformation bands (0.5 to 2 mm thick) can have permeabilities one to four orders of magnitude lower than the host rock. Bense et al. (2003) characterized faults in the Roer Valley Rift System (the Netherlands), and showed that in some cases, vertical faults may act as barriers to horizontal fluid flow (i.e. perpendicular to the fault). Groundwater level fluctuations, spring discharge rates and packer tests were analysed by Celico et al. (2006) to help refine the conceptual model of the Matese fractured limestone aquifer (Italy); in particular, by characterising the fault zone hydraulic conductivity. Their analyses highlighted the presence of low-permeability zones within the fault that act as barriers to groundwater flow perpendicular to the fault.

Bense and Person (2006) examined the conduit-barrier behaviour of the Baton Rouge Fault, which traverses sedimentary sediments in south Louisiana (USA). Large changes in hydraulic head were observed across the fault, indicating low permeabilities normal to the fault, whereas geochemical data showed enhanced vertical fluid flows (i.e. along the fault). Numerical modelling of 2D steady groundwater flow and solute transport demonstrated that the anisotropic nature of faults can partly explain the dual conduit-barrier behaviour observed in field studies.

Studies of solute transport across BFFs include analyses of contaminant migration across clay liners (e.g. Johnson et al., 1989) or barrier walls (e.g. Zhang and Qiu, 2010). These studies found that low-permeability clay liners beneath waste disposal

sites may not prevent contamination of underlying aquifers (Johnson et al., 1989), and that contaminant migration is largely influenced by the barrier's depth and hydraulic conductivity (Zhang and Qiu, 2010). However, small-scale solute transport processes at the matrix-BFF interface remain essentially unexplored.

The primary objective of this study is to explore within a modelling framework how the steady-state distributions of solute plumes in permeable aquifers are influenced by a DFF. This study extends the work of Sebben and Werner (2016), who treated DFFs as 1D flow features, considered only medium-sized fractures, neglected situations of BFFs, and did not attempt to account for the influence of back dispersion in their numerical results. This is achieved by evaluating: (1) the impact of 2D flow effects within DFFs, (2) solute plume changes where BFFs are encountered in otherwise permeable rock aquifers, and (3) the potential role of back dispersion on predictions of PFF effects on solute transport. A simple analytical expression for the advective displacement of a solute plume encountering a DFF is also presented. We examine the distribution of solutes for a variety of matrix-DFF permeability ratios and DFF apertures, adopting aquifer properties that are representative of sedimentary rocks (e.g. sandstone and limestone) in which PFFs, BFFs, and flow in the matrix are known to occur (e.g. Webb et al., 2010; Al Ajmi et al., 2014; Mádl-Szőnyi and Tóth, 2015).

## **4.3 Methodology**

### **4.3.1 Flow line refraction through discrete flow features**

We initially investigate the problem of 2D flow effects in DFFs by offering a new and simple expression for the displacement of a flow line as it passes through a DFF. The expression is founded on the refraction that occurs as water flows between two strata with different hydraulic conductivities (Hubbert, 1940). The degree of refraction is dependent on the angle of incidence ( $\sigma_1$ ; Figure 4.1) and the ratio of the two strata hydraulic conductivities ( $K_1$  and  $K_2$ ), as (Rumer and Shiau, 1968; Fetter, 2001):

$$\frac{K_1}{K_2} = \frac{\tan \sigma_1}{\tan \sigma_2} \quad (4.1)$$

where  $\sigma_1$  and  $\sigma_2$  are the angles of incidence and refraction, respectively (Figure 4.1), and  $K_1$  and  $K_2$  are the matrix hydraulic conductivity ( $K_m$ ) and the DFF hydraulic conductivity ( $K_f$ ), respectively.

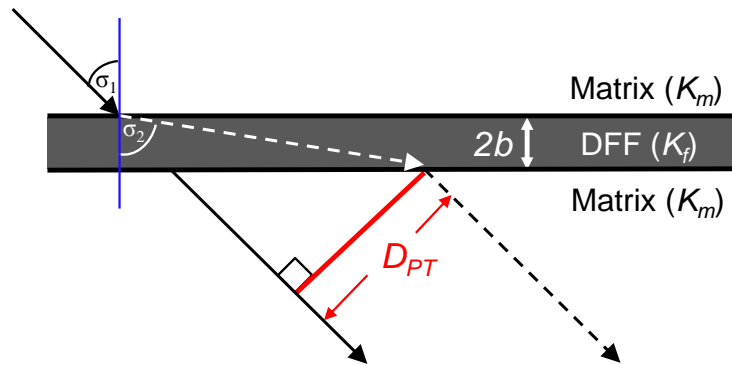


**Figure 4.1** Schematic description of the flow line displacement,  $D_{PT}$ . The solid black line represents the groundwater flow trajectory without a DFF. The dashed lines represent the flow line trajectory after refraction at interfaces between the matrix and DFF.

Considering the DFF aperture ( $2b$ ) and the geometry of the problem (Figure 4.1), we obtain a simple analytic expression for the orthogonal displacement ( $D_{PT}$ ) of the flow line, as:

$$D_{PT} = \frac{2b \sin(\sigma_2 - \sigma_1)}{\cos(\sigma_2)} \quad (4.2)$$

Flow line displacement is comparable to the displacement of peak solute concentration only where solute molecular diffusion and mechanical dispersion can be ignored. Equation (4.2) assumes stratified conditions (as opposed to the fully mixed conditions adopted by Sebben and Werner (2016); i.e. where solute concentration is uniform across the PFF's aperture) within the DFF. The optimal choice of stratified or fully mixed assumptions is unclear, and is likely to depend on the characteristics of the system.

It is noteworthy that the ratio of the components of groundwater flow (i.e. in the matrix and the DFF) parallel to the DFF is equal to the corresponding ratio of  $K$  values, based on Equation (4.1) and considering conservation of mass. That is, higher and lower Darcy velocities are expected in PFFs and BFFs, respectively, relative to the matrix velocity component in the DFF orientation immediately upstream of the DFF. This simple “rule of thumb” pertaining to groundwater flow in the vicinity of DFFs is important for the interpretation of numerical modelling results presented in later sections.

Birkhölzer et al. (1993a) and Sebben and Werner (2016) show that the transport and spreading of solutes associated with PFFs is mainly linked to the  $K_m/K_f$  ratio.  $K_f$  is commonly related to  $2b$  via the cubic law where PFFs are open conduits. To allow for the investigation of both PFFs and BFFs, and to consider independently the effects of aperture and  $K_f$ , DFFs in the present study are assumed to contain porous material (i.e. are not open channels). Therefore,  $K_f$  is always less than the value obtained from the cubic law (i.e. the upper limit of  $K_f$ ). This extends the analysis of Sebben and Werner (2016), who analysed only open-conduit PFFs. A range of

$K_m/K_f$  ratios is considered by modifying  $K_f$  within the range  $10^{-7}$  m/s (BFF) to  $10^{-3}$  m/s (PFF), and maintaining  $K_m$  at a value of  $10^{-5}$  m/s, which represents a moderately permeable rock matrix in which DFFs are likely to occur (e.g. limestone,  $10^{-6}$  m/s  $\leq K_m \leq 10^{-3}$  m/s; Geiger et al., 2010; Webb et al., 2010, and sandstone,  $10^{-8}$  m/s  $\leq K_m \leq 10^{-5}$  m/s; Birkhölzer et al., 1993a; Al Ajmi et al., 2014).  $2b$  is varied between that of a medium-sized fracture (0.25 mm) and a wide fracture (2 cm) (e.g. Barton, 1973).

### **4.3.2 Numerical investigation of dispersive effects on solute transport**

#### **4.3.2.1 Numerical model**

The simulations presented here were conducted using HydroGeoSphere (HGS; Therrien et al., 2010). HGS is a physics-based hydrogeological model, which solves 3D flow and solute transport in discretely fractured porous media. Detailed descriptions of the governing equations in HGS are provided elsewhere (e.g. Therrien and Sudicky, 1996; Therrien et al., 2010), and are not repeated here. We use HGS to simulate flow and transport within permeable rock matrices containing a DFF. No benchmarking has been undertaken of HGS for this exact problem; however, the code has been tested against the various components of the problem. For example, HGS has been benchmarked against the Tang et al. (1981) analytical solution for solute transport in a single PFF embedded within a porous, impermeable rock matrix (e.g. Weatherill et al., 2008, using the DFN approach).

HGS has also been benchmarked previously against the Wilson and Miller (1978) analytical solution (e.g. Therrien et al., 2010) describing the 2D dispersion of a solute plume in porous media under uniform, steady-state flow conditions, given as:

$$C = \frac{f'_m \exp\left(\frac{x}{B}\right) K_0\left(\frac{r}{B}\right)}{2\pi\theta_m (D_L D_T)^{\frac{1}{2}}} \quad (4.3.1)$$

$$B = \frac{2D_L}{V} \quad (4.3.2)$$

$$r = \left( x^2 + z^2 \frac{D_L}{D_T} \right)^{\frac{1}{2}} \quad (4.3.3)$$

where  $C$  [M/L<sup>3</sup>] is solute concentration,  $f'_m$  [M/LT] is the contaminant mass flux per unit length,  $x$  [L] is the distance from the plume source parallel to the flow direction,  $z$  [L] is the distance from the plume source perpendicular to the flow direction,  $\theta_m$  [-] is the matrix porosity,  $D_L$  [L<sup>2</sup>/T] is the longitudinal dispersion coefficient,  $D_T$  [L<sup>2</sup>/T] is the transverse dispersion coefficient,  $V$  [L/T] is the seepage velocity in the direction of flow, and  $K_0$  is the modified Bessel function of the second kind. The previous model testing discussed above demonstrates the numerical robustness of HGS for various situations of similar type to the current study (i.e. solute transport in fractured permeable rocks), notwithstanding that the influence of back dispersion on solute transport problems involving DFFs has not been systematically studied previously.

#### 4.3.2.2 Conceptual model

In this study, DFFs are incorporated in numerical modelling experiments as porous media layers, primarily because this representation allows for the evaluation of the effects of stratification within the DFF, which are otherwise neglected in the DFN approach. As mentioned above, stratification leads to displacement in flow lines that may not be adequately represented under the fully mixed conditions of the DFN approach of HGS. Also, this allows us to study BFFs, which are precluded by the DFN approach (Sebben and Werner, 2016). The model simulates groundwater flow and solute transport in a  $1 \text{ m} \times 1 \text{ m}$  2D cross section through a homogeneous, isotropic aquifer containing a single, straight DFF, located at  $z = 50 \text{ cm}$  (i.e. halfway through the domain). The small domain size was chosen to accommodate the very fine grid spacing required perpendicular to the medium-sized fractures (i.e.  $\Delta z \approx$  PFF aperture, following Weatherill et al. (2008)) if grid-independent results are to be achieved.

The findings from preliminary testing of the porous media approach to simulating DFFs are illustrated in Figure 4.2, which demonstrates that for a medium-sized, open PFF (wherein flow is calculated according the cubic law), the DFN and porous media representations of DFFs produce almost identical results. The ratios of the matrix-PFF Darcy velocities parallel to the PFF ( $q_{mx}/q_{fx}$ ) in both the DFN and porous media models follow the abovementioned “rule of thumb”, i.e.  $q_{mx}/q_{fx}$  are within 2% of the corresponding  $K_m/K_f$  for each case. It can be inferred from this that 2D effects (e.g. stratification) within open PFFs are small, at least for the cases illustrated in Figure 4.2. Therefore, the results of PFF simulations, which adopt the porous-medium representation of DFFs, are expected to be reasonably compatible with those obtained from DFN analyses.

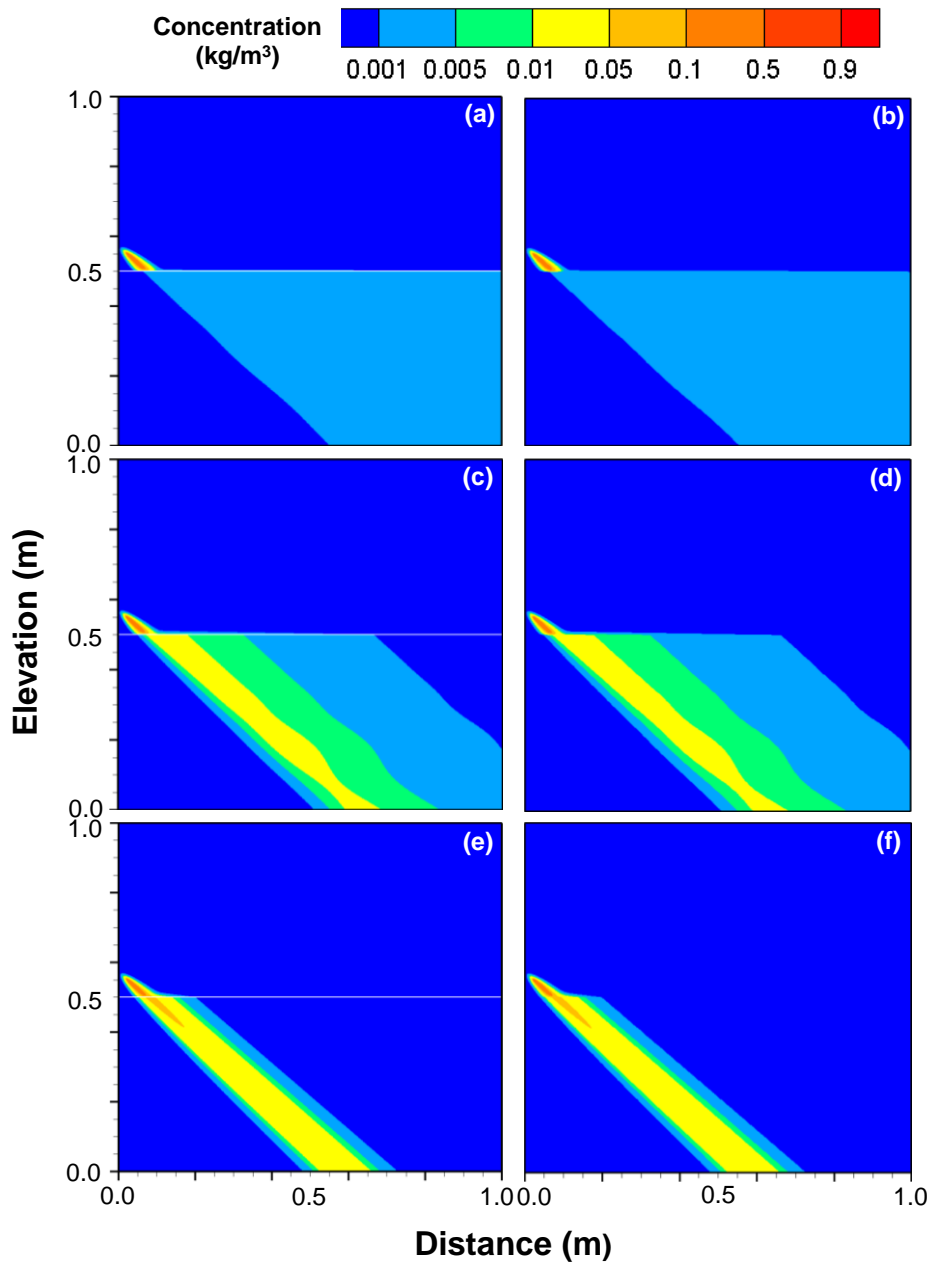


**Figure 4.2** Comparison of solute distributions involving a plume passing through a PFF that is oblique ( $45^\circ$ ) to the groundwater flow direction. PFFs are incorporated in models using the DFN approach (a, c, e) or as a porous media layer (b, d, f). The solid white line in the DFN models represents the discrete PFF.  $2b$  is 0.25 mm in (a) and (b) and 0.5 mm in (c) to (f). The  $K_m/K_f$  ratios for each case are: (a) and (b)  $2.0 \times 10^{-4}$ ; (c) and (d)  $2.4 \times 10^{-3}$ , and (e) and (f)  $2.5 \times 10^{-2}$ .

The conceptual model, including flow and transport boundary conditions, is shown in Figure 4.3. Constant-head boundaries are prescribed so that the orientation of groundwater flows is  $45^\circ$  relative to the DFF alignment. The DFF influences the flow field within the matrix, although the effect is small in most cases, particularly for PFFs. Nonetheless, the constant-head boundary conditions impose head gradients that create essentially consistent domain-scale flow conditions. A continuous mass flux of solute of  $3.7 \times 10^{-9}$  kg/m/s is assigned at  $x = 10.0$  cm, and at 4.8 cm above the DFF, such that the concentration at the source ( $C_0$ ) is approximately  $1.0$  kg/m<sup>3</sup>.

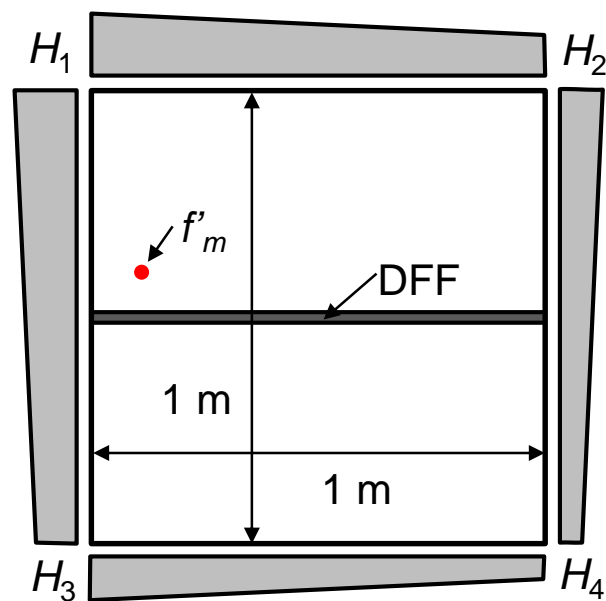


**Figure 4.3** Conceptual model of a permeable rock matrix containing a DFF (not to scale), where  $H$  is hydraulic head and  $f'_m$  is contaminant mass flux. Adapted from Sebben and Werner (2016).

The model domains were discretised into variable-block elements ranging from  $\Delta x = 0.39$  mm (minimum block width; Scenario 1) to 2.5 mm (maximum block width; Scenario 4), and  $\Delta z = 0.13$  mm (minimum block height; i.e. half the  $2b$  of Scenario 1) to 2.5 mm (maximum block height; Scenario 4). In all cases,  $\Delta z$  at the matrix-

DFF interface is equal to half the aperture. A grid convergence test was undertaken in which other mesh resolutions were evaluated (i.e. the mesh size was increased by 66.7% (Scenarios B1, B3, B4 and D1) or decreased by 66.7% (Scenarios B3, B4, D3 and D4)). A finer grid produced peak solute concentrations beneath the DFF that varied by up to 0.82% (Scenario B3). Scenarios re-run with coarser grids produced peak solute concentrations that were different by up to 17.4% (Scenario B3).

The 3D model has a unit width to replicate a 2D domain. Simulations were first run to produce steady-state flow conditions. Solute transport was then simulated in transient mode until steady-state conditions were reached. The simulation period of 92 days was subdivided using adaptive time-stepping based on a maximum 1% change in salt concentration at any node.

Sensitivity analyses were performed by modifying  $K_m/K_f$  and  $2b$ , to examine their impact on steady-state solute plume distributions. Additional simulations were performed to consider the influence of  $\alpha_L$  (longitudinal dispersivity) and  $\alpha_T$  (transverse dispersivity). The measurable aspects of each simulation are shown in Figure 4.4, which provides the solute plume distributions for the matrix-only (MO) model (Figure 4.4a) and Scenario A1 (Figure 4.4b) for illustrative purposes. Measured characteristics of plumes include: (1) solute plume width in the MO model ( $W_{MO}$ ) and in the DFF model ( $W_{DFF}$ ), (2) plume asymmetry ratio ( $W_L/W_R$ ), i.e. the ratio of the width of the solute plume to the left of  $C_{max}$  ( $W_L$ ), to the width of the solute plume to the right of  $C_{max}$  ( $W_R$ ), and (3) maximum solute concentration beneath the DFF ( $C_{max}$ ). It is noteworthy that analyses of plume width and

symmetry are undertaken along the alignment of the DFF (i.e. at  $45^\circ$  relative to the flow direction), and therefore,  $W_L/W_R$  indicates an asymmetric plume even for MO cases (in which the plumes are symmetric perpendicular to the flow direction).

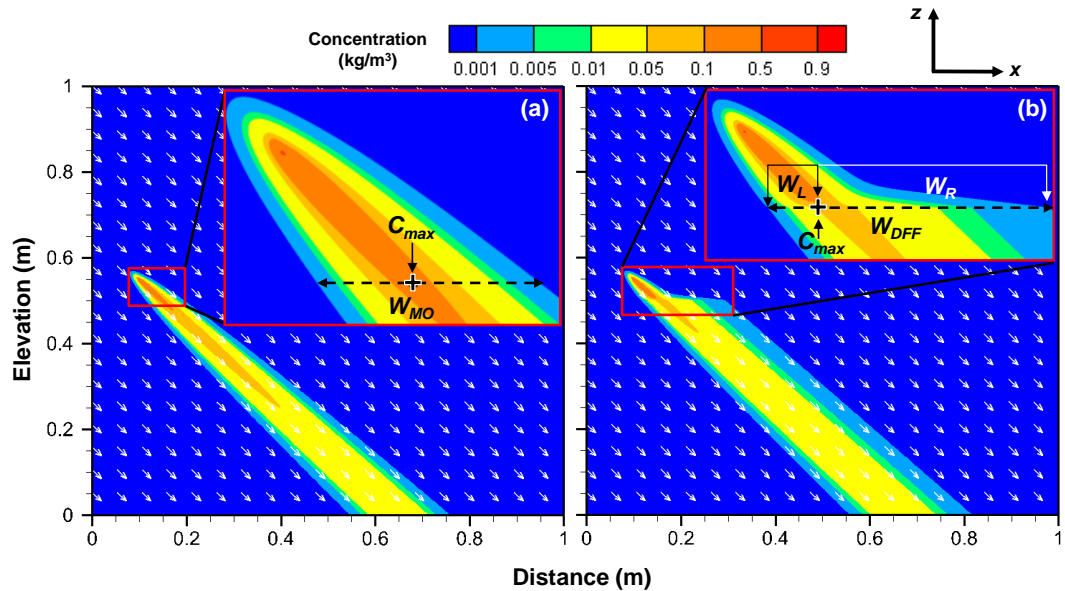


**Figure 4.4** Schematic description of the solute plume comparison metrics in: (a) the MO model, and (b) the DFF model. Colours represent the solute concentrations. White arrows show the direction of velocity vectors. Black dashed arrows indicate the width of the solute plume. Black crosses highlight the location of maximum solute concentration immediately beneath the DFF.

$C_{max}$  (black crosses; Figure 4.4) is referred to herein as  $C_{PFF}$ ,  $C_{BFF}$  and  $C_{MO}$  in the PFF, BFF and MO models, respectively. The horizontal distance between the  $x$ -location of  $C_{MO}$  and that of  $C_{PFF}$  or  $C_{BFF}$  ( $D_H$ ; Figure 4.5) is used in the forthcoming analysis to calculate the displacement of peak solute concentration in the numerical models ( $D_{NM}$ ), given as:

$$D_{NM} = \cos \sigma_1 D_H \quad (4.4)$$

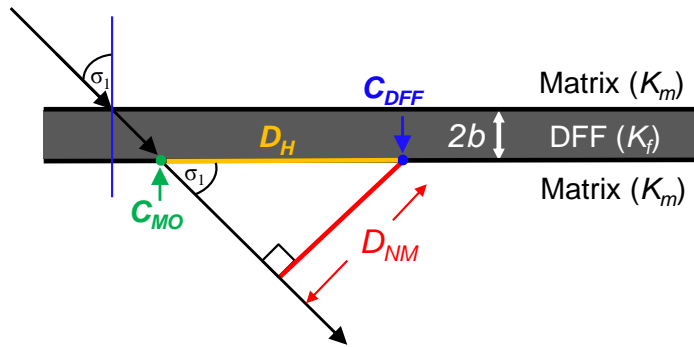


**Figure 4.5** Schematic description of the displacement of peak solute concentration,  $D_{NM}$ . The solid black line represents the groundwater flow trajectory without a DFF.  $C_{MO}$  is the peak solute concentration without a DFF and  $C_{DFF}$  is the peak solute concentration beneath the DFF.  $D_H$  indicates the horizontal distance between the  $x$ -location of  $C_{MO}$  and  $C_{DFF}$ .

#### 4.3.2.3 Fractured aquifer scenarios

Six cases with different  $K_m/K_f$  ratios were evaluated (Cases A to F). Cases A, B and C examined the effects of PFFs (i.e.  $K_m/K_f = 0.01, 0.1$  and  $0.5$ , respectively), whereas Cases D, E and F considered the effects of BFFs (i.e.  $K_m/K_f = 2, 10$  and  $100$ , respectively). DFFs in all cases were considered to be filled to some degree with porous material, such that the DFF porosity ( $\theta_f$ ) was  $< 1$ . Within each case, four scenarios were tested using values for  $2b$  of  $0.25$  mm (Scenario 1),  $0.5$  mm (Scenario 2),  $1$  cm (Scenario 3) and  $2$  cm (Scenario 4). All other parameter values are listed in Table 4.1.

**Table 4.1** Simulation parameters for Cases A to F.

	Cases A to F
Matrix porosity ( $\theta_m$ , -)	0.1
Matrix hydraulic conductivity ( $K_m$ , m/s)	$10^{-5}$
Matrix longitudinal dispersivity ( $\alpha_L$ , m)	$5.0 \times 10^{-3}$
Matrix transverse dispersivity ( $\alpha_T$ , m)	$5.0 \times 10^{-4}$
DFF aperture ( $2b$ , m)	$2.5 \times 10^{-4}$ - $2.0 \times 10^{-2}$
DFF porosity ( $\theta_f$ , -)	0.2
DFF hydraulic conductivity ( $K_f$ , m/s)	$10^{-7}$ - $10^{-3}$
DFF longitudinal dispersivity ( $\alpha_{LF}$ , m)	$5.0 \times 10^{-3}$
DFF transverse dispersivity ( $\alpha_{TF}$ , m)	$5.0 \times 10^{-4}$
Solute mass flux ( $f'_m$ , kg/m/s)	$3.66 \times 10^{-9}$
Darcy velocity in the matrix ( $q_m$ , m/s)	$1.414 \times 10^{-6}$
Matrix-DFF hydraulic conductivity ratio ( $K_m/K_f$ , -)	$10^{-2}$ – $10^2$

### 4.3.3 Back dispersion effects

Back dispersion effects on solute plume distributions were evaluated by comparing the PFF simulations described above (i.e. using the conceptual model illustrated in Figure 4.3) with modified simulations that exclude back dispersion. This was achieved by imposing derived solute concentrations to the top of the PFF that were obtained from the Wilson and Miller (1978) solution. By fixing the concentrations at the upper boundary, back dispersion effects are avoided, because there are no downstream boundary effects within the simulation from which the concentration profile is obtained. This approach assumes that advection towards the PFF is sufficient to overcome dispersion in the upstream direction that might otherwise cause solutes to move from the DFF into the matrix in opposition to the flow

direction. It is acknowledged that without physical modelling, the occurrence and extent of back dispersion in real-world conditions is unclear, and therefore, the simulations that exclude back dispersion provide guidance that is conditional on the assumption that in some cases, no back dispersion would occur in reality. Simulations were undertaken using Scenarios A3, B3, C3, A4, B4 and C4, except with the model domain described above truncated at the top of the PFF, and with constant concentrations (according to Wilson and Miller (1978) values) prescribed along the top model boundary. Boundary conditions were otherwise the same as those illustrated in Figure 4.3.

## **4.4 Results**

### **4.4.1 Analysis of flow line refraction through discrete flow features**

Table 4.2 shows the displacement resulting from refraction at matrix-DFE interfaces ( $D_{PT}$ ; i.e. Equation (4.2)) for the various cases and scenarios. The sign of the values listed in Table 4.2 indicate the direction of  $D_{PT}$ , i.e. BFFs cause flow lines to refract in the opposite direction to PFFs. Positive  $D_{PT}$  values represent displacement to the right in Figure 4.1.

**Table 4.2** Displacement due to flow line refraction in Cases A to F.

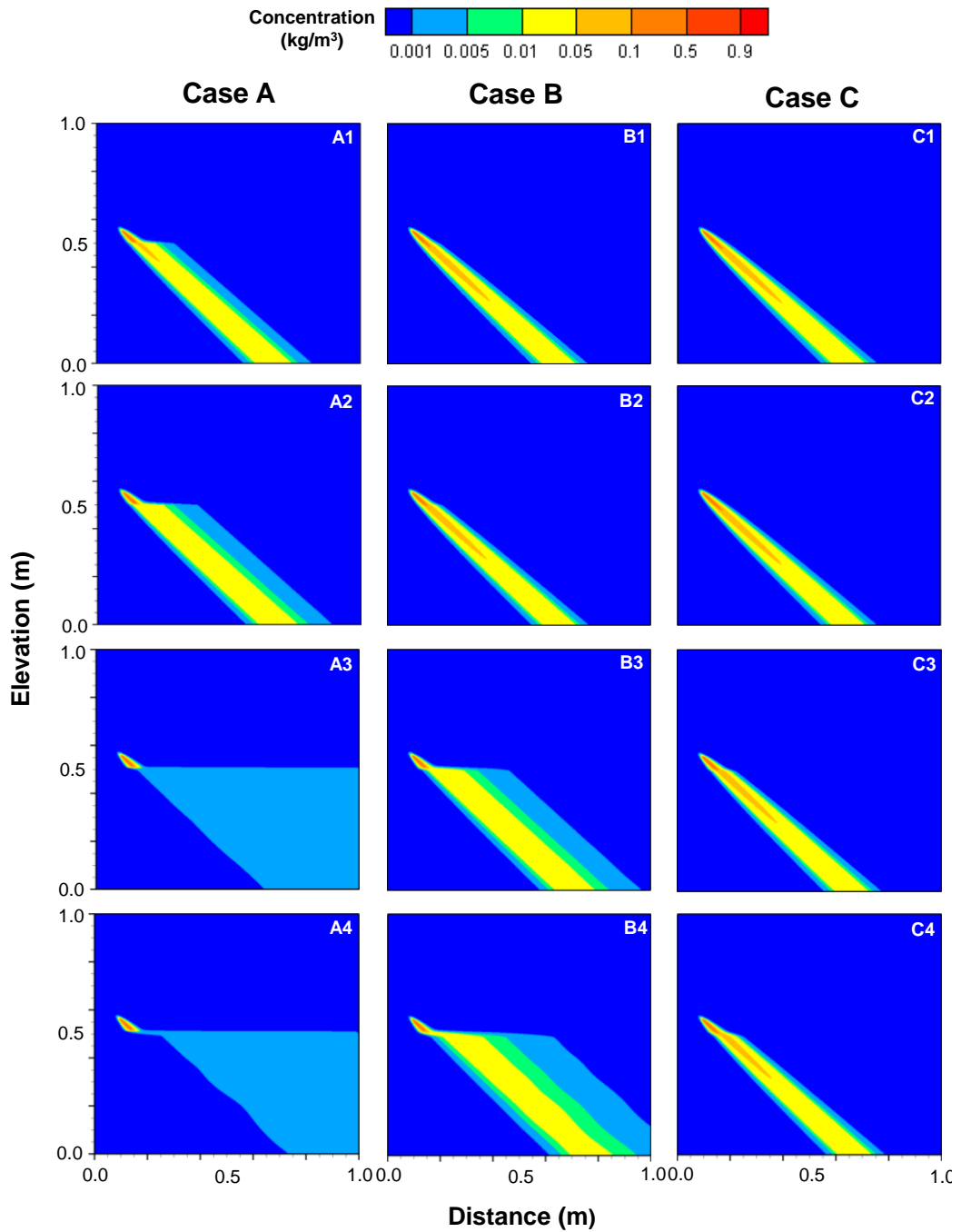
Case	$D_{PT}$ (cm)			
	Scenario 1	Scenario 2	Scenario 3	Scenario 4
A	1.75	3.50	70.0	140
B	0.16	0.32	6.36	12.73
C	0.02	0.04	0.71	1.42
D	-0.01	-0.02	-0.35	-0.71
E	-0.02	-0.03	-0.64	-1.27
F	-0.02	-0.04	-0.70	-1.40

Table 4.2 shows that as  $K_m/K_f$  increases in PFF cases (Cases A to C;  $K_m/K_f = 0.01$ , 0.1 and 0.5, respectively), the displacement due to refraction decreases, consistent with Rumer and Shiau, (1968) (i.e. Equation (4.1)). Conversely, the magnitude of displacement ( $|D_{PT}|$ ), caused by BFFs (Cases D to F;  $K_m/K_f = 2$ , 10 and 100, respectively), increases as  $K_m/K_f$  increases. The magnitude of BFF displacement ranges from 0.01 to 0.5 times the corresponding displacement (i.e. where BFF  $K_m/K_f$  is the same as PFF  $K_f/K_m$ ) in PFF cases. For example,  $|D_{PT}|$  in Scenario D1 (0.01 cm) is approximately half that of Scenario C1 (0.02 cm), noting that Case C  $K_m/K_f$  is equal to Case D  $K_f/K_m$ . In all cases,  $|D_{PT}|$  increases as  $2b$  increases, i.e.  $|D_{PT}|$  is greater in Scenario 4 than in Scenarios 1 to 3. The results in Table 4.2 suggest that, in the absence of dispersive effects and for the boundary conditions considered here, PFFs are likely to have a greater influence than BFFs on the displacement of solute plumes in moderately permeable rocks, at least for corresponding ratios of  $K_m$  to  $K_f$ .

#### 4.4.2 2D effects of DFFs on solute transport

##### 4.4.2.1 PFFs

Figure 4.6 illustrates the steady-state solute plume distributions caused by different PFFs in a moderately permeable rock matrix. The corresponding MO model is shown in Figure 4.4a. Darcy velocity in the rock matrix is  $1.41 \times 10^{-6}$  m/s in the direction of flow. Darcy velocities in the PFF are in the range of  $2.24 \times 10^{-6}$  m/s (Case C;  $K_m/K_f = 0.5$ ) to  $1.00 \times 10^{-4}$  m/s (Case A;  $K_m/K_f = 0.01$ ) in the direction of flow.



**Figure 4.6** Steady-state salinity distributions for PFF Cases A ( $K_m/K_f = 0.01$ ), B ( $K_m/K_f = 0.1$ ) and C ( $K_m/K_f = 0.5$ ).

Visual inspection of the plumes in Figure 4.6 indicates that PFFs with larger aperture (i.e. Scenarios 3 and 4) generally produce a greater displacement than smaller PFFs (i.e. Scenarios 1 and 2). This is consistent with refraction theory, as indicated by the results of Table 4.2. For a given scenario, solute plumes are wider

in Case A ( $K_m/K_f = 0.01$ ) than in Cases B and C ( $K_m/K_f = 0.1$  and  $0.5$ , respectively). The plume width also increases from Scenario 1 to Scenario 4, such that plumes immediately beneath the PFF intercept the right boundary ( $x = 1$  m) in Scenarios A3 and A4. PFFs in Case A typically produce less-symmetric plumes than PFFs in Cases B and C, and PFFs in Scenarios 3 or 4 typically produce less-symmetric plumes than PFFs in Scenarios 1 and 2. The solute plumes in Scenarios A3 and A4 are more dispersed than in Scenarios A1, A2, and all Cases B and C. The peak solute concentration beneath the PFF in Scenarios A3 and A4 is approximately  $0.001 \text{ kg/m}^3$ , whereas significantly higher solute concentrations ( $C > 0.01 \text{ kg/m}^3$ ) occur beneath the PFF in all other scenarios.

Specific aspects of the simulated plumes are evaluated in quantitative terms (e.g. displacement, width, asymmetry and attenuation), as illustrated in the graphs that follow. The modelled displacements ( $D_{NM}$ ) of solute plumes are shown in Figure 4.7.

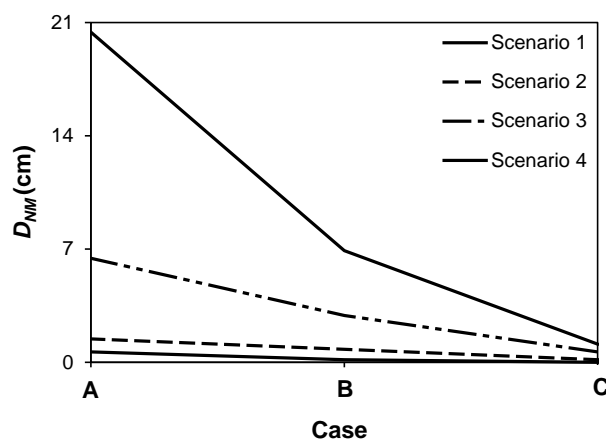


**Figure 4.7** Influence of  $K_m/K_f$  (cases) and  $2b$  (scenarios) on  $D_{NM}$  in PFF cases.

Figure 4.7 shows that the magnitude of  $D_{NM}$  decreases as  $K_m/K_f$  increases (i.e. from Cases A to C) and  $2b$  decreases (i.e. from Scenario 4 to Scenario 1).

The effects of dispersion on the displacement of the peak concentration of a plume passing through a PFF are shown in Figure 4.8, which compares the displacement of peak concentration to the flow line displacement (i.e.  $D_{NM}$  versus  $D_{PT}$ ).

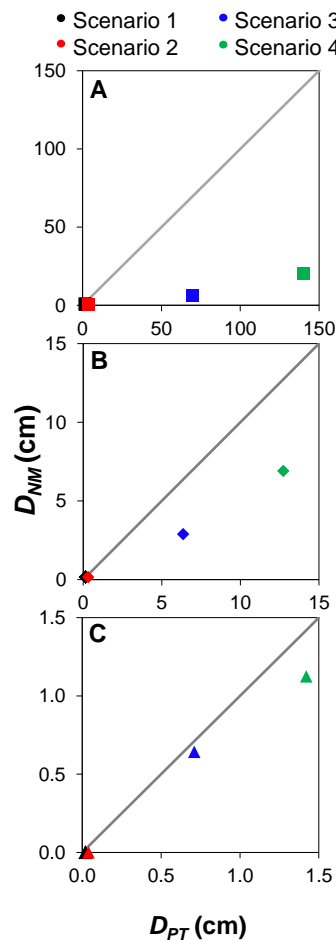


**Figure 4.8** Comparisons of  $D_{NM}$  and  $D_{PT}$  for Cases A, B and C. Scenarios 1, 2, 3 and 4 are indicated by black, red, blue and green markers, respectively. Note that the marker for Scenario 1 is obscured by Scenario 2 in each case. The 1:1 line is illustrated in grey.

The results in Figure 4.8 demonstrate that for smaller values of  $K_m/K_f$  (e.g. 0.01; Case A),  $D_{PT}$  is much larger than  $D_{NM}$ , indicated by the departure of the coloured markers from the 1:1 line. That is, the difference between  $D_{NM}$  and  $D_{PT}$  obtained for

Case A suggest that  $K_m/K_f$  is having a substantial influence on the role of dispersion in displacement (whereby the smaller ratios produce a larger deviation between  $D_{NM}$  and  $D_{PT}$ ), relative to Cases B and C. In all PFF cases,  $D_{NM}$  for Scenarios 1 and 2 are less than  $D_{PT}$ , although the required scale of the  $x$ -axis in Figure 4.8 prohibits visual representation of this difference. Scenarios C1 and C2 are an exception, because the PFF displaces the solute plumes by less than the horizontal grid resolution ( $\Delta x$ ), such that  $D_{NM} \approx 0$  cm. Therefore,  $K_m/K_f$  does not visibly impact the dispersive effect on the displacement of peak concentration for these scenarios.  $D_{NM}$  and  $D_{PT}$  are the most similar for Scenario C3 (a relative difference of 9%). This indicates a minor influence of the PFF in Case C on the role of dispersion in displacement. The small deviation in the flow line (i.e.  $D_{PT}$ ) for Scenario C3 means that  $D_{NM}$  is well-represented by  $D_{PT}$ .

The influence of dispersion on the displacement of peak concentration at the matrix-PFF interface was further examined by modifying the matrix and PFF longitudinal and transverse dispersivities ( $\alpha_L$ ,  $\alpha_{LF}$ ,  $\alpha_T$  and  $\alpha_{TF}$ , respectively) in Scenario B3 ( $K_m/K_f = 0.1$ ; results not shown for brevity). Increasing the dispersivities (by a factor of 2) to  $\alpha_L = \alpha_{LF} = 0.01$  m and  $\alpha_T = \alpha_{TF} = 0.001$  m causes a reduction in the magnitude of displacement from  $D_{NM} = 2.89$  cm to  $D_{NM} = 2.25$  cm. Conversely, reducing the dispersivities to  $\alpha_L = \alpha_{LF} = 0.003$  m and  $\alpha_T = \alpha_{TF} = 0.0003$  m increases  $D_{NM}$  to 3.37 cm. This result is expected, because lowering the dispersivity reduces the dispersiveness of the plume causing  $D_{NM}$  to converge on the higher, non-dispersive displacement value of  $D_{PT}$  (6.36 cm). Numerical instabilities arising from very small dispersivities precluded the HGS simulation of non-dispersive solute transport (i.e. advection-only) scenarios.

Figure 4.9 illustrates the following key solute plume metrics: (a) plume widening due to the PFF, given as the ratio of PFF and MO solute plume widths immediately beneath the PFF ( $W_{PFF}/W_{MO}$ ), (b) plume asymmetry in PFF simulations, given as the ratio  $W_L/W_R$ , and (c) attenuation of plume concentration attributable to the PFF, given as the ratio of PFF and MO peak concentrations immediately beneath the PFF ( $C_{PFF}/C_{MO}$ ). Scenarios A3 and A4 are omitted from Figures 4.9a and 4.9b because the concentration isochlor used to define plume characteristics (i.e.  $C = 0.001$  kg/m<sup>3</sup>) intercepts the right model boundary and hence,  $W_{PFF}$  and  $W_R$  cannot be obtained.

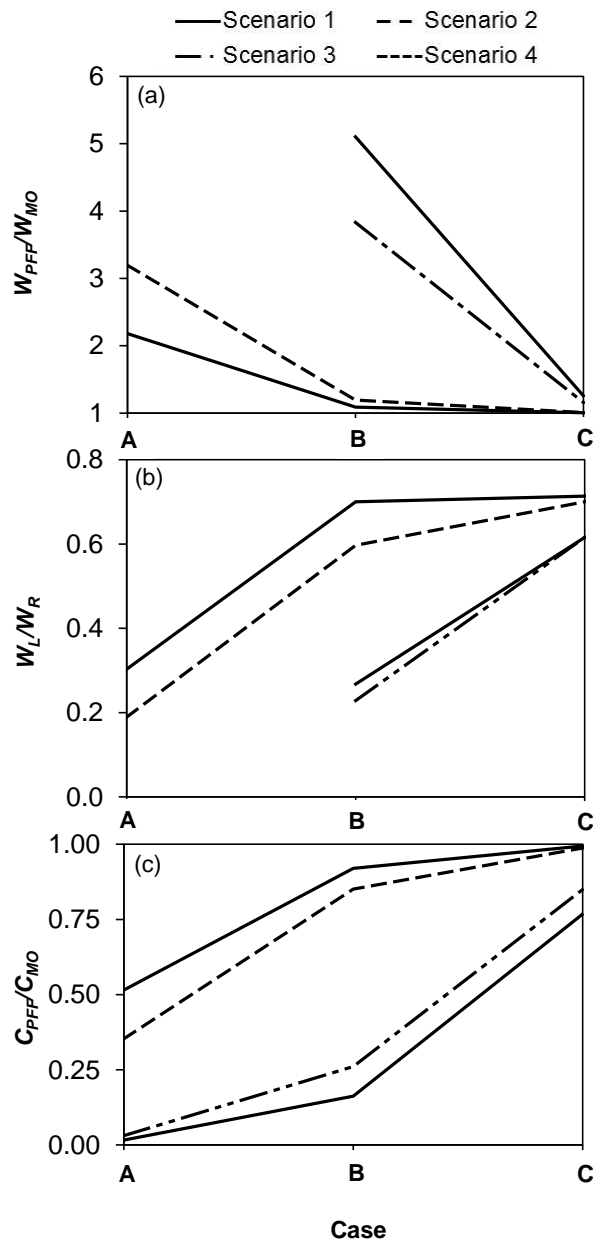


**Figure 4.9** Influence of  $K_m/K_f$  and  $2b$  on: (a)  $W_{PFF}/W_{MO}$ , (b)  $W_L/W_R$ , and (c)  $C_{PFF}/C_{MO}$  in PFF cases.

Figure 4.9a shows that the PFF causes a widening of the solute plume in the region of the model beneath the PFF, except in Scenario C1 ( $K_m/K_f = 0.5$ ), where the PFF's effect on the plume width is  $< \Delta x$ .  $W_{PFF}/W_{MO}$  typically decreases from Case A to Case C, demonstrating that PFFs have a greater impact on solute plume width when  $K_m/K_f$  is small (i.e. 0.01; Case A). This result is expected, and can be explained in

part by the more substantial influence of smaller  $K_m/K_f$  ratios on the dispersive effects of PFFs. A similar pattern of results was observed by Sebben and Werner (2016), who demonstrated that under the same constant-head boundary conditions employed in the current study, medium-sized, open PFFs had a greater impact on plume spreading when  $K_m/K_f$  was small. The results in Figure 4.9a also demonstrate (beyond the results of Sebben and Werner (2016)) that PFFs have a greater impact on solute plume width when  $2b$  is larger (i.e. from Scenario 1 to Scenario 4).

Asymmetry in the PFF model solute plumes (i.e.  $W_L/W_R$ ) is illustrated in Figure 4.9b. For the MO models,  $W_L/W_R = 0.72, 0.72, 0.64$  and  $0.70$  for Scenarios 1 to 4, respectively. Figure 4.9b shows that plume asymmetry is more pronounced in cases characterised by smaller  $K_m/K_f$  ratios (i.e. the plumes in Case A are less symmetric than in Cases B and C). Figure 4.9b also demonstrates that increasing  $2b$  imparts a greater degree of asymmetry in the solute plumes. A similar pattern was observed for Case A, albeit Scenarios A3 and A4 are omitted for reasons given above.

Attenuation of the peak solute concentrations in the PFF models is expressed in Figure 4.9c as the ratio of the maximum concentration beneath the PFF ( $C_{PFF}$ ) to the maximum solute concentration at the same elevation in the MO model ( $C_{MO}$ ), i.e.  $C_{PFF}/C_{MO}$ . Figure 4.9c demonstrates that smaller  $K_m/K_f$  ratios (Case A) produce more attenuated plumes than larger  $K_m/K_f$  ratios (Cases B and C). Increasing  $2b$  also produces more attenuated plumes, i.e.  $C_{PFF}/C_{MO}$  decreases from Scenario 1 to Scenario 4. The impact of  $2b$  on  $C_{PFF}/C_{MO}$  decreases as  $K_m/K_f$  increases, i.e. from Case A ( $K_m/K_f = 0.01$ ) to Case C ( $K_m/K_f = 0.5$ ).

The results presented for PFF cases considered in this study demonstrate that cases characterised by smaller  $K_m/K_f$  ratios (e.g.  $K_m/K_f = 0.01$ ; Case A) exhibit greater dispersive effects, in the form of wider, more asymmetric plumes, and a greater departure from non-dispersive displacement.

#### **4.4.2.2 BFFs**

Figure 4.10 illustrates the steady-state solute plume distributions caused by different BFFs in a moderately permeable rock matrix (corresponding MO model shown in Figure 4.4a).

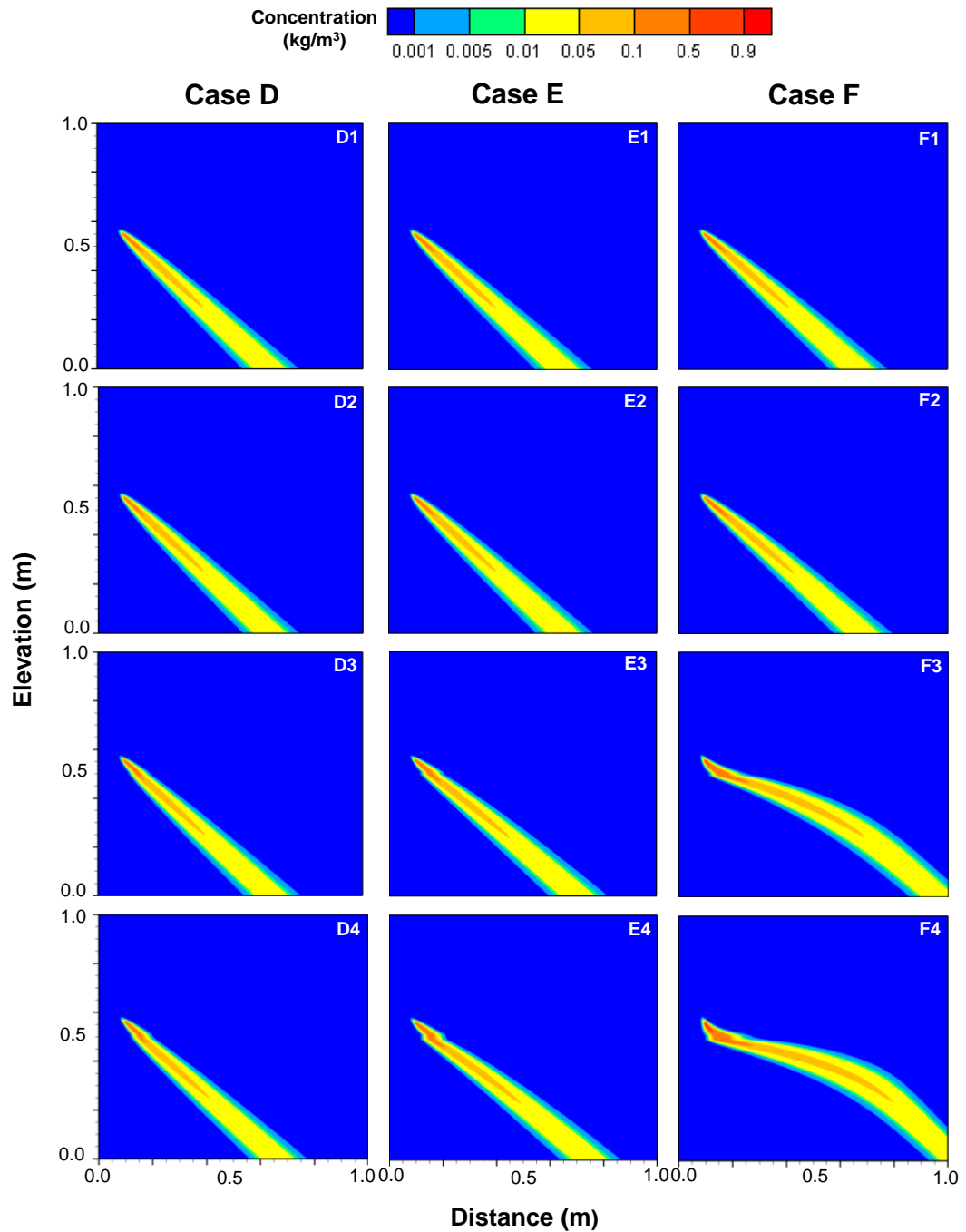


**Figure 4.10** Steady-state salinity distributions for BFF Cases D ( $K_m/K_f = 2$ ), E ( $K_m/K_f = 10$ ) and F ( $K_m/K_f = 100$ ).

Figure 4.10 demonstrates that BFFs with larger  $2b$  (e.g. Scenario 4) produce greater displacement. A similar pattern was observed for the PFF cases in Figure 4.6, and is consistent with the results in Table 4.2. The BFFs in Figure 4.10 are shown to

have a lesser influence on plume spreading compared to PFFs. That is, the widths of the solute plumes do not vary greatly between cases, although in general terms, plumes are a little wider in Cases E and F ( $K_m/K_f = 10$  and  $100$ , respectively) than in Case D ( $K_m/K_f = 2$ ). Changing  $2b$  has only a minor effect on plume spreading, i.e. within each case, plume widths in Scenarios 2 to 4 are within 10% of Scenario 1. Figure 4.10 also demonstrates that the peak solute concentrations beneath the BFFs are typically higher than those observed in the PFF cases (i.e.  $C < 0.25 \text{ kg/m}^3$  beneath BFFs,  $C < 0.12 \text{ kg/m}^3$  beneath PFFs). In Scenarios F3 and F4, the solute plumes display a curved shape. A closer inspection of the flow field for Scenario F4 is given in Figure 4.11.

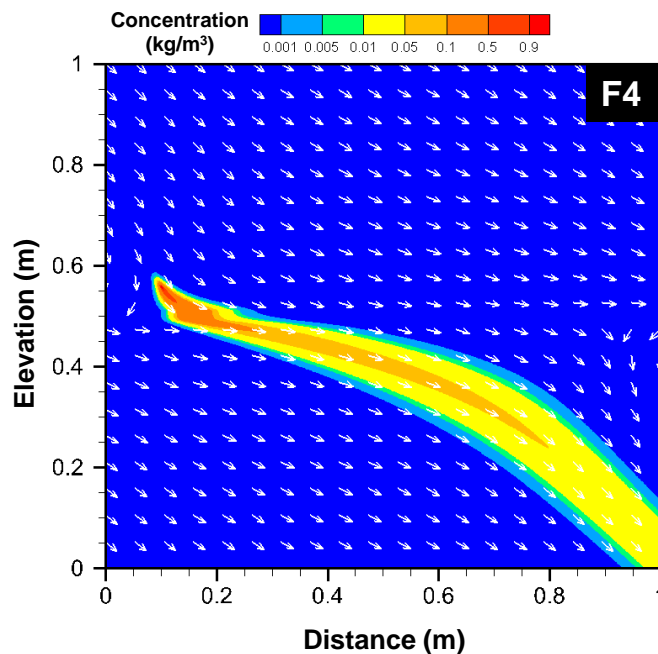


**Figure 4.11** Steady-state solute plume for Scenario F4 ( $K_m/K_f = 100$ ). White arrows indicate flow direction.

It is clear from Figure 4.11 that there is an interaction between the low  $K_f$  of the BFF and the model boundary that result in a plume curvature that is unlikely to

occur in real-world situations. Scenarios F3 and F4 were re-simulated using larger domain sizes (2 m × 2 m and 4 m × 4 m; results not shown) in an attempt to reduce the boundary effects on the solute distributions. The curvature of the plumes persists in the 2 m × 2 m models, but is reduced significantly in the 4 m × 4 m models. However, the domain size required a coarser grid discretization ( $\Delta x = 10$  mm,  $\Delta z = 3.1$  mm to 6.8 mm) so that the maximum number of nodes was not exceeded, leading to significant numerical errors and results that were grid-dependent. The results for Scenarios F3 and F4 (Figure 4.10) are therefore omitted from the forthcoming analysis.

The displacement, width, asymmetry and amplification of solute plumes, caused by BFFs, are evaluated in quantitative terms in the following sections. Figure 4.12 shows the modelled displacements ( $D_{NM}$ ) of solute plumes. Negative values for  $D_{NM}$  indicate that the plume is displaced in the opposite direction to the horizontal component of the regional groundwater flow (i.e. to the left in Figure 4.5). The Scenario 3 and Scenario 4 lines in Figure 4.12 are discontinuous because  $D_{NM}$  for Scenarios F3 and F4 are not included.

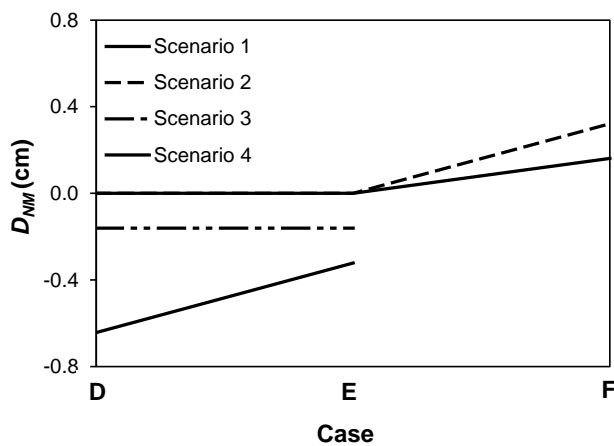


**Figure 4.12** Influence of  $K_m/K_f$  (cases) and  $2b$  (scenarios) on  $D_{NM}$  in BFF cases.

Figure 4.12 shows that the BFFs in Scenarios D1, D2, E1 and E2 do not displace the peak concentration as the plume passes through the BFF (i.e.  $D_{NM} \approx 0.0$  cm).  $D_{NM}$  is typically zero or negative for BFF cases because  $K_m/K_f > 1$  and  $\sigma_2 < \sigma_1$  (i.e. Equation (4.1)) and hence  $D_H$  (Figure 4.5) is negative. Scenarios F1 and F2 are exceptions, which is likely due to the interactions interaction between the low  $K_f$  of the BFFs and the model boundary, as was explored above for Scenarios F3 and F4. The general trend in Figure 4.12 demonstrates that as  $K_m/K_f$  and  $2b$  increase,  $D_{NM}$  also increases.

Dispersive effects on displacement as plumes encounter a BFF are shown in Figure 4.13 as  $D_{NM}$  versus  $D_{PT}$ .

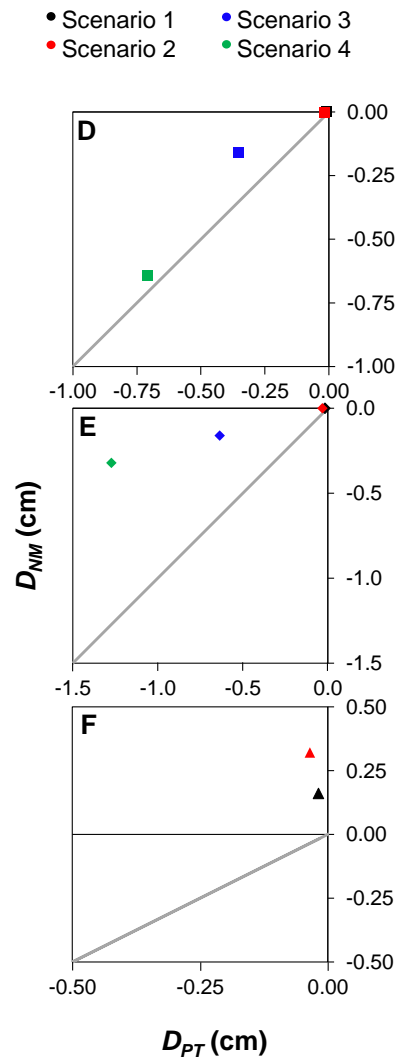


**Figure 4.13** Comparisons of  $D_{NM}$  and  $D_{PT}$  for Cases D, E and F. Scenarios 1, 2, 3 and 4 are indicated by black, red, blue and green markers, respectively. Note that the marker for Scenario 1 is obscured by Scenario 2 in Cases D and E. Markers are not illustrated for Scenarios F3 and F4 because  $D_{NM}$  has been omitted. The 1:1 line is illustrated in grey.

Figure 4.13 shows that for all BFF cases,  $D_{NM} > D_{PT}$  (i.e. the coloured markers for each scenario are positioned above the 1:1 line). The relative differences between  $|D_{NM}|$  and  $|D_{PT}|$  are less for smaller values of  $K_m/K_f$  (e.g. 2; Case D), indicating that  $K_m/K_f$  has a lesser influence on displacement in Case D compared to Cases E and F ( $K_m/K_f = 10$  and  $100$ , respectively). That is, smaller  $K_m/K_f$  ratios (for BFF cases) produce a smaller deviation between displacement from dispersive and non-dispersive approaches. For Scenarios D1, D2, E1 and E2, the BFF displaces the

peak solute concentration by less than  $\Delta x$  (i.e.  $D_{NM} \approx 0$  cm) and thus, the dispersive effect on the displacement of peak concentration is not visibly impacted by  $K_m/K_f$  for these scenarios.  $D_{NM}$  and  $D_{PT}$  are the most similar for Scenario D4 (a relative difference of 9%).

Figure 4.14 illustrates the key solute plume metrics: (a) plume widening due to the BFF, given as the ratio of BFF and MO solute plume widths immediately beneath the BFF ( $W_{BFF}/W_{MO}$ ), (b) plume asymmetry in BFF simulations, given as the ratio  $W_L/W_R$ , and (c) amplification of plume concentration attributable to the BFF, given as the ratio of peak BFF and MO concentrations immediately beneath the BFF ( $C_{BFF}/C_{MO}$ ).

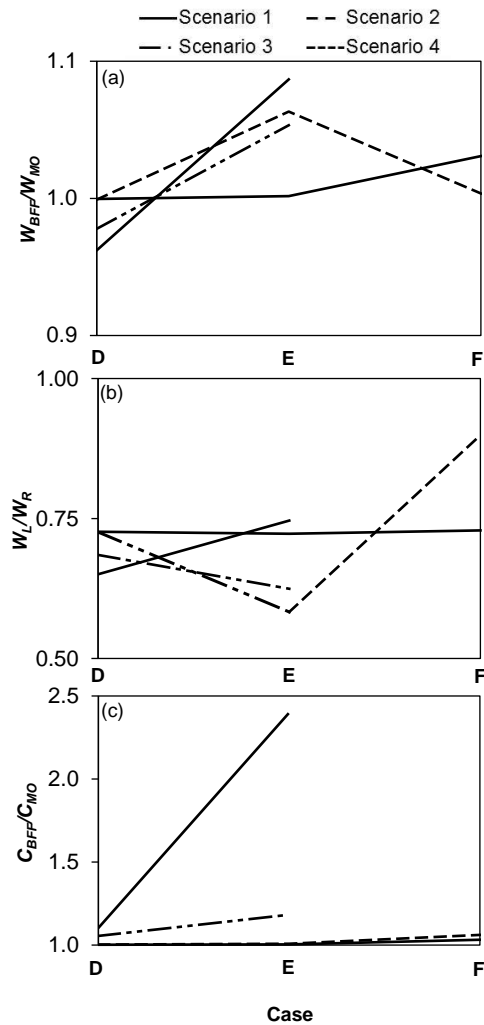


**Figure 4.14** Influence of  $K_m/K_f$  and  $2b$  on: (a)  $W_{BFF}/W_{MO}$ , (b)  $W_L/W_R$ , and (c)  $C_{BFF}/C_{MO}$  in BFF cases.

Figure 4.14a shows that solute plume widths are largely unaffected by BFFs (< 10% difference relative to the MO case). BFFs generally have a greater impact on solute plume width when  $K_m/K_f$  and  $2b$  are larger. That is,  $W_{BFF}/W_{MO}$  typically increases from Case D ( $K_m/K_f = 2$ ) to Case F ( $K_m/K_f = 100$ ) and from Scenario 1 to Scenario 4. This result is expected, and can be explained in part by the more substantial influence of larger  $K_m/K_f$  ratios on the dispersive effects of BFFs. Scenarios E3 and F2 are exceptions ( $W_{BFF}/W_{MO}$  decreases from Scenario E2 to F2, and from Scenario E2 to E3). The results in Figure 4.14a also shown that  $W_{BFF}/W_{MO} < 1$  for Scenarios D3 and D4, indicating that the plumes are narrower than for the MO case.

Asymmetry in the BFF model solute plumes (i.e.  $W_L/W_R$ ) is illustrated in Figure 4.14b. The plume asymmetry ratio is always  $< 1$  (i.e.  $W_R > W_L$ ), as was observed for the PFF cases. Figure 4.14b demonstrates that all values of  $W_L/W_R$  are relatively high (i.e.  $W_L/W_R > 0.5$ ), indicating that BFFs have a lesser influence on plume asymmetry than the PFFs examined above. In Scenarios D1, D2, D3, E4, F1 and F2, plumes beneath the BFFs are more symmetrical than in the associated MO models. The increased symmetry is likely due to the refraction of flow lines intercepting the BFF, which causes a simultaneous reduction in  $W_R$  and increase in  $W_L$ , such that  $W_L$  approaches the value of  $W_R$ . The influences of BFFs on  $W_L/W_R$  follow non-monotonic relationships for the remaining scenarios considered in the current study. Notably,  $K_m/K_f$  has only a minor influence on  $W_L/W_R$  for Scenario 1 ( $< 1\%$  variation relative to the MO case for Cases D to F).

Amplification of the peak solute concentration caused by the BFF is illustrated in Figure 4.14c. Figure 4.14c shows that the impact of BFFs on solute concentrations contrasts that of PFFs, which were shown in Figure 4.9c to attenuate (rather than amplify) the relative peak solute concentrations. That is,  $C_{BFF}/C_{MO}$  is always  $\geq 1$ , whereas  $C_{PFF}/C_{MO}$  is always  $< 1$ . BFFs cause the greatest increase in solute concentrations in cases with larger  $K_m/K_f$  and  $2b$  values (i.e. from Case D to Case F and from Scenario 1 to Scenario 4). Medium-sized BFFs (D1, D2, E1, E2, F1 and F2) have either no impact on the peak solute concentration, such that  $C_{BFF}/C_{MO} \approx 1$  (Scenarios D1, D2 and E1), or have a small ( $< 7\%$ ) strengthening effect on peak concentrations.

The results presented for the BFF cases considered in this study demonstrate that cases characterised by larger  $K_m/K_f$  ratios (e.g.  $K_m/K_f = 100$ ; Case F) typically exhibit greater dispersive effects on plume width and displacement. The dispersive effects of  $K_m/K_f$  on plume symmetry are unclear for BFF cases.

#### **4.4.3. Back dispersion**

The potentially non-physical effects of back dispersion (i.e. the anomalous movement of solutes from the PFF back into the matrix against the vertical direction of flow ( $q_{mz}$ )) up-gradient of PFFs (Sebben and Werner, 2016) are investigated for Cases A to C (Scenarios 3 and 4 only). Concentrations along the top of the PFF are compared in Figure 4.15 for cases with back dispersion (i.e. *BD*) and without back dispersion (i.e. *no BD*). Solute plumes with and without back dispersion are illustrated in Figures 4.6 and 4.15, respectively.

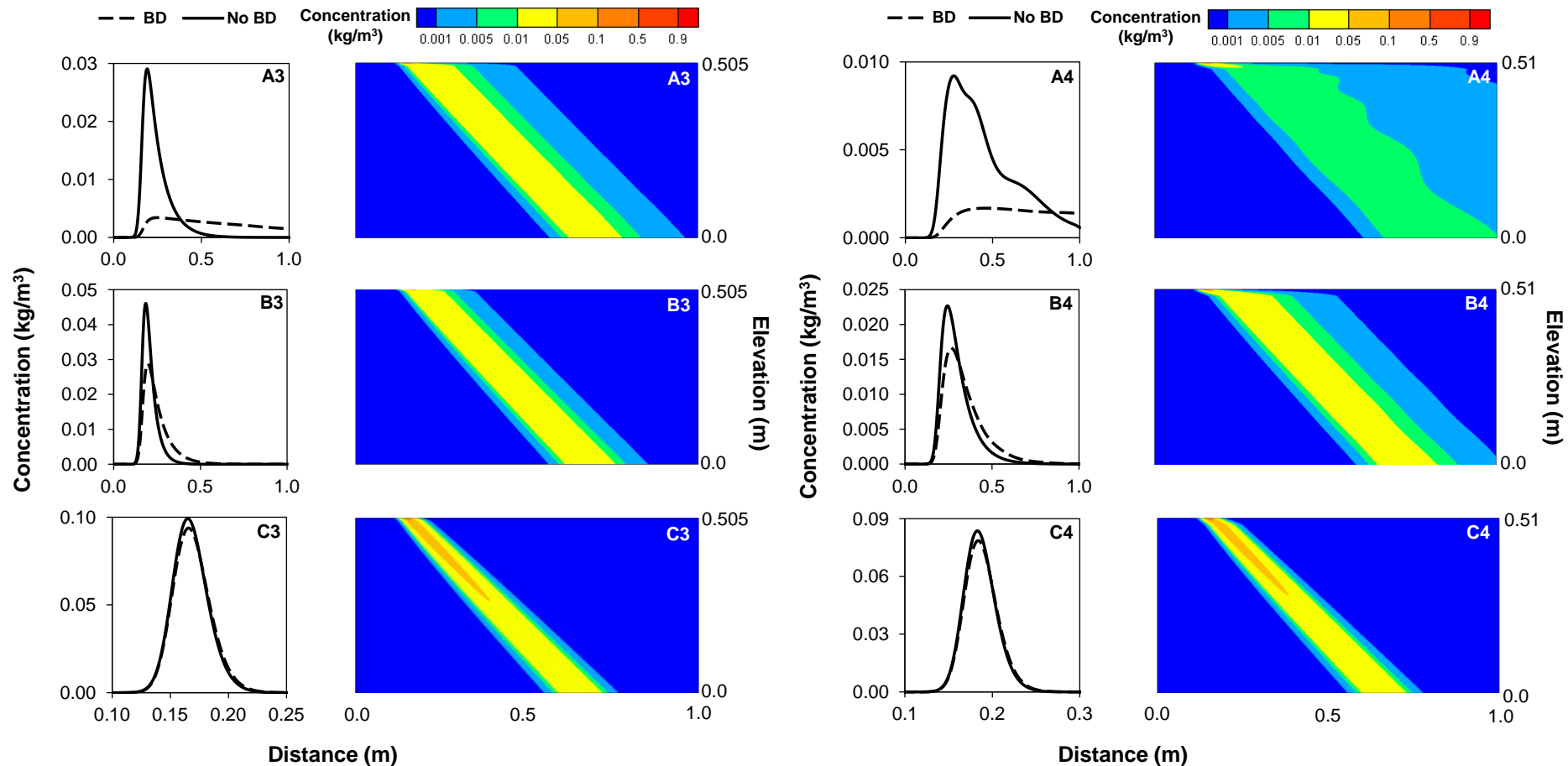


**Figure 4.15** Comparison of solute plume distributions with and without back dispersion in Cases A, B and C (Scenarios 3 and 4 only). Solute concentrations are compared along the top of the PFF in cases with back dispersion (black dashed line) and without back dispersion (solid black line). Solute concentrations in and beneath the PFFs in cases with no back dispersion are indicated by colours.

The concentration profiles illustrated in Figure 4.15 highlight an increase in back dispersion effects in cases with smaller  $K_m/K_f$  ratios (i.e. Case A;  $K_m/K_f = 0.01$ ) compared to larger  $K_m/K_f$  ratios (i.e. Cases B and C;  $K_m/K_f = 0.1$  and  $0.5$ , respectively). That is, more back dispersion occurs in cases with larger dispersive effects. This is demonstrated in the concentration versus distance plots in Figure 4.15, which show the difference between the peak solute concentrations along the top of the PFFs in cases with and without back dispersion. The solute concentrations along the top of the PFFs in Case C correspond approximately with those obtained using Equation (4.3), i.e. for MO conditions, and hence, it is unlikely that back dispersion plays an important role in the predictions. In Cases A and B, solute concentrations above the PFF are greater in cases with back dispersion, notwithstanding that the peak concentrations are attenuated in comparison to MO conditions.

The solute plumes for Cases B and C, shown in Figure 4.15, differ considerably to those presented for the comparable scenarios in Figure 4.6. The elimination of back dispersion reduces  $W_{PFF}/W_{MO}$  markedly in some cases, e.g. by 33% and 19% in Scenarios B3 and B4, respectively. Solute plumes are more symmetrical in cases without back dispersion, except in Scenario C4. The results from the simulations with and without back dispersion suggest that, in general terms, back dispersion has a considerable influence on the solute distributions in the PFF cases considered here, particularly for cases characterised by smaller  $K_m/K_f$  ratios. We note that, while back dispersion influences the peak concentration and width of the plumes for the cases explored here, the effect is minor in comparison to other factors such as  $K_m/K_f$  and  $2b$ .

## 4.5 Discussion

The impact of  $K_m/K_f$  on  $D_{PT}$  resulting from the current study was similar to the findings of Sebben and Werner (2016), who partially attributed the displacement of the peak concentration of a solute plume passing through a medium-sized, open PFF to refraction at the matrix-PFF interfaces. Both studies show that, where  $K_m/K_f$  is closer to unity (e.g. Cases C and D in the current study),  $|\sigma_2 - \sigma_1|$  is smaller, which leads to less displacement of the flow line (i.e. Equation (4.1)). A schematic description of the range of potential  $|D_{PT}|$  for PFF and BFF cases is illustrated in Figure 4.16.

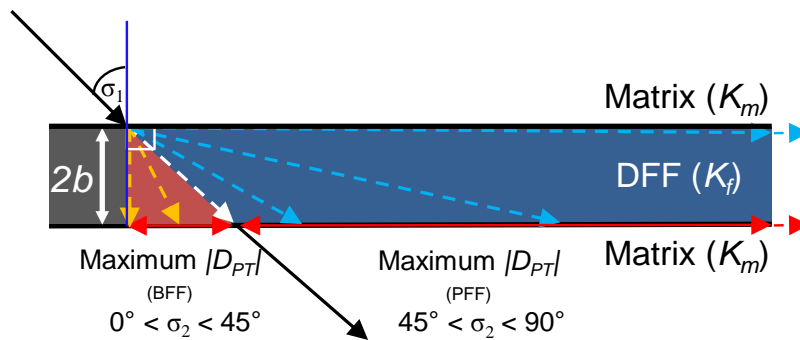


**Figure 4.16** Schematic description of potential  $|D_{PT}|$  for solute plumes intercepting a DFF in a steady flow field oblique to the DFF (solid black and white dashed arrows). Dark blue shading indicates a PFF. Red shading indicates a BFF. Blue dashed arrows illustrate potential flow lines for PFF cases. Orange dashed arrows illustrate potential flow lines for BFF cases. Red arrows indicate the maximum  $|D_{PT}|$ .

Figure 4.16 shows that, as  $\sigma_2$  approaches  $90^\circ$  (i.e. as  $K_m/K_f$  of PFF cases decreases), flow lines (and hence, pathlines for advective solute transport) are parallel to the PFF. As such, the maximum  $|D_{PT}|$  for PFF cases theoretically approaches infinity, or practically, the end of the PFF. Conversely, as  $K_m/K_f$  for BFF cases increases,  $\sigma_2$  approaches  $0^\circ$ , i.e. pathlines of advective solute transport are perpendicular to the

BFF, and the theoretical maximum  $|D_{PT}|$  is reached. Figure 4.16 demonstrates that in aquifers where groundwater flow is oblique to a DFF,  $|D_{PT}|$  for PFF cases is typically greater than for BFF cases. For all cases explored in this study,  $|D_{PT}|$  also increased from Scenario 1 (smallest  $2b$ ) to Scenario 4 (largest  $2b$ ) (i.e. Equation (4.2)). Sebben and Werner (2016) did not examine the impact of  $2b$  on solute plume displacement, and thus, to the best of the authors' knowledge, this is the first numerical study to consider the influence of  $2b$ , independent of  $K_f$ , on solute plume displacement in permeable rock matrices.

The previous work of Sebben and Werner (2016) demonstrated that the displacement of a plume's centre of mass is largely unaffected by the degree of dispersion of the plume as it passes through a PFF. Therefore, it is hypothesised that the displacement of a plume's centre of mass as it passes through a DFF is  $\approx |D_{PT}|$ . Table 4.3 shows the displacement of the plumes' centres of mass ( $D_{COM}$ ) for the various cases and scenarios explored in this study. Scenarios A3, A4, F3 and F4 are omitted from Table 4.3 because the plumes intercept the right model boundaries (Case A), or are influenced by significant boundary effects (Case F).

**Table 4.3** Displacement of plume centre of mass for Cases A to F.

Case	$D_{COM}$ (cm)			
	Scenario 1	Scenario 2	Scenario 3	Scenario 4
A	1.75	3.45	-	-
B	0.16	0.32	6.20	12.2
C	0.02	0.03	0.66	1.29
D	-0.01	-0.01	-0.28	-0.56
E	<0.01	<0.01	-0.18	-0.74
F	0.14	0.26	-	-

The results in Table 4.3 indicate that for most scenarios,  $D_{COM}$  and  $|D_{PT}|$  (Table 4.1) are in good agreement. For example,  $D_{COM}$  for PFF cases (Cases A to C) are generally within 10% of  $|D_{PT}|$ . The agreement between  $D_{COM}$  and  $|D_{PT}|$  is less for BFF cases, in particular, for Cases E and F.  $D_{COM}$  for Case D is within the same order of magnitude as  $|D_{PT}|$ , whereas  $|D_{PT}|$  generally does not provide a good approximation of  $D_{COM}$  for Cases E and F. Causal factors of the disagreement are presently unclear, and warrant further analysis that is outside the scope of the current study. Despite this, the results in Table 4.3 suggest that the analytical solution in Equation (4.2) offers a reasonable approximation of the displacement of a plume's centre of mass as it passes through a DFF.

Numerical predictions for the displacement of peak solute concentrations (i.e.  $D_{NM}$ ) showed a similar pattern of results to those obtained from the refraction analyses of flow lines (i.e.  $D_{PT}$ ). That is, PFF cases characterised by larger  $K_m/K_f$  ratios ( $K_m/K_f = 0.5$ ; Case C) were displaced to a lesser degree than in cases with small  $K_m/K_f$  ratios (i.e.  $K_m/K_f = 0.01$  and  $0.1$ ; Cases A and B, respectively). For BFF cases,  $D_{NM}$  was greater for cases with larger  $K_m/K_f$  ratios ( $K_m/K_f = 100$ ; Case F). DFFs with larger  $2b$  were also found to produce larger  $|D_{NM}|$  than DFFs with smaller  $2b$ . Comparisons of  $D_{NM}$  and  $D_{PT}$  (i.e. the difference between  $D_{NM}$  and  $D_{PT}$ ) demonstrated that dispersion effects are greater in some cases than in others. A causal factor is that as  $K_m/K_f$  increases (in PFF cases) or decreases (in BFF cases), the flow rate in the DFF ( $q_f$ ) approaches the flow rate in the matrix ( $q_m$ ;  $1.4 \times 10^{-6}$  m/s), thus reducing the variation in flow velocities that occurs across the matrix-DFF interface. Where the velocities are similar in the matrix and the DFF, there is

a reduced opportunity for DFF-based dispersion to occur (i.e. that would not have otherwise occurred without the DFF).

Aquifers containing a PFF were found to produce wider solute plumes than those containing a BFF. The impacts of PFFs on plume width resulting from the current study were similar to the study of medium-sized, open PFFs by Sebben and Werner (2016). Both studies demonstrate that aquifers characterised by smaller  $K_m/K_f$  ratios produce wider plumes. This is because of the larger deviation of flow lines for smaller  $K_m/K_f$  ratios, which results in longer distances of flow within PFFs prior to re-entry into the rock matrix. In a similar manner, increasing  $2b$  was found to increase the width of plumes in all PFF cases, because solutes will remain inside the PFF for longer before re-entering the rock matrix. The impacts of BFFs on plume width were found to be minor in comparison to PFF effects, because BFFs tend to change the angle of refraction (i.e.  $\sigma_2$ ; Figure 4.1) such that solutes cross the fracture through a shorter distance relative to flow angle changes caused by PFFs (i.e. Figure 4.16).

For all cases explored in this study, DFFs were shown to influence the symmetry of solute plumes immediately beneath the DFF. Asymmetry caused by PFFs was found to be more pronounced for smaller  $K_m/K_f$  (i.e. larger  $W_{PFF}$ ) and for PFFs with larger  $2b$ . BFFs typically produced more symmetrical plumes beneath the BFF. Causal factors for the impact of DFFs on plume symmetry are that different parts of the plume intercept the DFF at different angles relative to the DFF alignment, whereby solutes to the left of the peak concentration arrive at a steeper angle and solutes to the right of the peak concentration arrive at a shallower angle. The

refraction and displacement therefore differs between the left and right of the peak concentration, which enhances the asymmetric effects. Solutes that disperse to the left of the main plume trajectory have a shorter path to exit the DFF (and hence, are transversely dispersed less) than solutes that disperse to the right, as was observed for PFF cases by Sebben and Werner (2016). As such, plumes beneath PFFs are less symmetrical than in MO cases. For BFF cases, refraction at the matrix-BFF interfaces causes a simultaneous reduction in  $W_R$  and increase in  $W_L$ , such that  $W_L$  approaches the value of  $W_R$  and hence, plumes beneath BFFs are typically more symmetrical than in MO cases.

Peak solute concentrations were found to be lower beneath PFFs, and higher beneath BFFs, relative to the associated MO models. For the PFFs considered here, cases with smaller  $K_m/K_f$  values (Case A) caused a greater attenuation of  $C_{PFF}/C_{MO}$  than those characterised by larger  $K_m/K_f$  ratios (i.e. Cases B and C). This is because under low  $K_m/K_f$  conditions,  $q_f$  is considerably faster than  $q_m$  such that the dispersive effect of the PFF is greater. Conversely,  $C_{BFF}/C_{MO}$  was found to be amplified in aquifers containing BFFs. That is,  $C_{BFF}/C_{MO}$  typically increased as  $K_m/K_f$  increased (from Case D to Case F), although the impact of BFFs on  $C_{BFF}/C_{MO}$  was generally small for Scenarios 1 and 2 (i.e.  $C_{BFF}/C_{MO} \approx 1$ ). This is because  $q_f$  (and hence, mechanical dispersion in the BFF) decreases under high  $K_m/K_f$  conditions (Case F), which reduces the degree of plume spreading in the BFF compared to spreading in the rock matrix.

The fixed concentration simulations presented here highlight the influence of back dispersion on plume concentrations immediately above PFFs. Back dispersion

effects were found to be more pronounced in cases characterised by smaller  $K_m/K_f$  ratios (Case A) compared to larger  $K_m/K_f$  ratios (i.e. Cases B and C). The causes of back dispersion are unclear, although in the case of seawater intrusion problems, back dispersion was eliminated by modifying the downstream boundary condition (e.g. Segol et al., 1975). The current research does not evaluate the causes of, or factors contributing to, back dispersion. This remains an area for further investigation. For example, the degree of back dispersion is likely influenced by the Peclet number ( $Pe$ ), equal to  $V\Delta L/D$ , where  $V$  [L/T] is the seepage velocity in the direction of flow,  $\Delta L$  [L] is the element length in the direction of flow, and  $D$  [L<sup>2</sup>/T] is the dispersion coefficient.

#### **4.6 Conclusions**

In this study, the influence of a single DFF on the distribution of solute plumes in permeable rocks is investigated. We quantify the displacement and widening (or narrowing) of a steady-state solute plume as it passes through a DFF (representing a medium-to-large fracture) in idealised, moderately permeable rock aquifers. The analytical and numerical simulation results presented here provide an important first step towards understanding plume behaviour in more complex, real-world aquifer settings. Matrix-DFF permeability contrasts and DFF aperture are shown to have a considerable influence on plume displacement and spreading, particularly for PFFs. The key findings of this study are:

- 1) Solute plumes passing through a DFF embedded in a permeable rock matrix will be displaced to varying degrees, depending on  $K_m/K_f$  and  $2b$ . The magnitude of displacement of a plume passing through a PFF is larger in

cases characterised by smaller  $K_m/K_f$  ratios, because the dispersive effect is greater. For plumes passing through a BFF, the influence of  $K_m/K_f$  on the magnitude of displacement follows non-monotonic relationships. PFFs generally have a greater influence than BFFs on plume displacement in moderately permeable rocks, for the conceptual models considered here. In all cases, the degree of displacement increases as  $2b$  increases.

- 2) Medium-to-large PFFs embedded in moderately permeable rocks typically widen solute plumes. The increase in plume width is greatest when  $K_m/K_f$  is smaller, and for larger  $2b$ . Plumes passing through a BFF are widest when  $K_m/K_f$  and  $2b$  are large; however, they are generally narrow in comparison to PFF cases.
- 3) The asymmetry of solute plumes passing through a PFF is greater for smaller  $K_m/K_f$  ratios, and for larger  $2b$ . Plume symmetry is largely unaffected by BFFs in comparison to PFFs. For the boundary conditions considered here, solute plumes beneath BFFs are in some cases more symmetrical than in the associated MO models.
- 4) Peak solute concentrations are attenuated by PFFs, particularly in cases where  $K_m/K_f$  is small. This effect is intensified as  $2b$  increases from a medium-sized PFF to a large PFF. In contrast, peak solute concentrations are amplified by BFFs, such that plumes are typically more concentrated beneath BFFs compared to PFF or MO cases. Amplification of solute concentrations is minor beneath medium-sized BFFs, but increases significantly for larger BFFs.
- 5) Back dispersion has a more pronounced effect on the solute concentrations upstream of a PFF in cases where  $K_m/K_f$  is smaller. Reducing the influence

of back dispersion generally results in plumes that are narrower, more symmetrical, and more concentrated than in cases with back dispersion.

The current study adds to the previous findings by Sebben and Werner (2016) by providing insights into role of BFFs, the effects of 2D flow in DFFs, and DFF aperture, on the distribution of solute plumes in permeable aquifers. The present study also offers a new, simple analytical expression for the advective displacement of a solute plume intercepting a DFF.

A variety of complex concentration distributions have been demonstrated for a range of idealised aquifer conditions. In real-world aquifers, the variability in DFF size, location and orientation will likely amplify the complexity of the solute plumes presented in the current study. Substantial underestimations of plume extent may arise if PFFs are excluded from numerical models. The exclusion of BFFs is likely to be less impactful, notwithstanding that solute plumes are typically more concentrated beneath BFFs compared to in the matrix only.

# Chapter 5

## 5. Conclusions

The three studies presented in this thesis examined the influence of discrete flow features (DFFs) on contaminant transport in permeable rocks. Numerical modelling was undertaken to investigate how preferential flow features (PFFs) and flow barriers (BFFs) impact the displacement and spreading of solute plumes, in either density-dependent (PFFs only) or density-independent systems. In Chapter 2, a preliminary numerical investigation of seawater intrusion (SWI) in fractured permeable rocks was performed using modified forms of the Henry (1964) SWI benchmark problem. This study provided new insights into the role of fracture location, orientation and density on the distribution of seawater in coastal aquifers, in a first step towards determining the distribution of seawater in more complex coastal aquifer settings (i.e. fractured-rock systems) than has previously been attempted through numerical analysis. Chapter 3 explored how PFFs can influence the migration of density-independent solute plumes in otherwise permeable rocks, to try to unravel the solute plume behaviour observed in the complicated coastal setting of Chapter 2. Numerical simulations demonstrated the local-scale effects on solute plumes passing through an individual PFF, for a variety of matrix-PFF permeability contrasts representative of sedimentary aquifers. The analysis of Chapter 4 extended the Chapter 3 results by considering BFF situations, and the impact of 2D flow effects within DFFs. A simple analytical expression and numerical modelling provided important preliminary insights into the displacement and spreading of a solute plume as it passes through a DFF, and the attenuating effects of DFFs, in permeable rock aquifers.

The key findings from each of the three Chapters are as follows:

- 1) Chapter 2 demonstrates that vertical fractures within the seawater wedge are likely to increase the width of the seawater-freshwater mixing zone, whereas vertical fractures inland of the wedge have a minimal impact on the seawater distribution in the aquifer. Horizontal fractures in the zone of freshwater discharge may enhance the inland extent of seawater; whereas fractures in the lower part of the aquifer are likely to truncate the wedge and reduce the amount of seawater in the aquifer. Where inclined fractures are approximately parallel to the seawater-freshwater interface, SWI is likely to be enhanced. If fractures are roughly perpendicular to the interface, SWI tends to be inhibited. Homogeneous equivalent porous media (EPM) models based on the bulk hydraulic properties of the aquifer are likely to be unsuitable for inferring the distribution of seawater in the majority of fractured scenarios. The EPM approach may be applicable only to high-density, orthogonal fracture scenarios if the flow system can be well-represented by the EPM model, and if appropriate EPM dispersivity values can be determined.
  
- 2) Chapter 3 concludes that the impacts of an individual PFF on solute plume distributions are similar to the multi-PFF study by Odling and Roden (1997). For example, both studies demonstrate that solute transport and dispersion within a permeable rock matrix can be enhanced by the presence of PFFs, and that a significant portion of the solute may reside within the

matrix. The analyses in Chapter 3 also show that solute plumes are likely to be wider and more attenuated (i.e. the peak solute concentration is reduced) beneath a PFF compared to the same location in associated porous media only (PMO) cases. If the matrix-DFF hydraulic conductivity ratio ( $K_m/K_f$ ) is smaller, then the displacement of the peak solute concentration passing through a PFF is likely to be larger. Plumes that are less dispersed as they encounter a PFF typically produce plumes that are more asymmetric and attenuated beneath the PFF. As the orientation of a PFF approaches the primary flow direction, PFF effects on solute plumes are likely to be more pronounced. PFFs (rather than the matrix material) generally dominate the spreading of solute plumes in permeable rock matrices wherein the PFF spacing is less than several metres. For some of the cases explored in this study, solute concentrations above the PFF in the DFN models were found to be higher than in the PMO models. It is hypothesised that ‘back dispersion’, i.e. the anomalous movement of solutes against the flow direction, may be the potential cause of these observations; however, further analyses are needed to confirm this.

- 3) For the cases considered in Chapter 4, PFFs are shown to have a greater influence on the displacement of peak concentrations than BFFs, that is, for corresponding ratios of  $K_m/K_f$  and  $K_f/K_m$ . For PFF cases, the degree of displacement increases as  $K_m/K_f$  decreases, and as the PFF aperture ( $2b$ ) increases. Plumes encountering a medium-to-large PFF embedded in moderately permeable rock are generally wider beneath the PFF than at the corresponding location in the matrix only (MO) models. The increase in

plume width beneath PFFs is greatest when  $K_m/K_f$  is smaller, and for larger  $2b$ . The attenuation effect of PFFs is intensified as  $2b$  increases. When  $K_m/K_f$  is smaller and  $2b$  is larger, solute plumes passing through a PFF are generally more asymmetric. It is hypothesised that back dispersion is the cause of changes in solute concentration above PFFs. Back dispersion appears to have a greater influence on solute concentrations upstream of a PFF in cases where  $K_m/K_f$  is smaller. Reducing the influence of back dispersion generally produces narrower, more symmetrical plumes that are more concentrated than in cases affected by back dispersion. For BFF cases, the influence of  $K_m/K_f$  on the magnitude of displacement follows non-monotonic relationships. The magnitude of displacement increases as  $2b$  increases, similar to PFF cases. Plumes passing through a BFF are widest when  $K_m/K_f$  and  $2b$  are large, and are generally narrower than for PFF cases. Plume symmetry is largely unaffected by BFFs, although for some cases considered in this study, solute plumes beneath BFFs are more symmetrical than in the associated MO models. Plumes beneath BFFs are typically more concentrated compared to PFF or MO cases. This effect is also intensified as  $2b$  increases.

The numerical investigations presented in this thesis demonstrate a variety of complex salinity distributions for a range of idealised aquifer conditions involving DFFs. In real-world aquifers, the variability in DFF size, location, orientation and density will likely amplify the complexity of the relationships presented here. Nonetheless, this work has shown how DFFs can control the extent of contaminant migration in permeable rock aquifers. Substantial underestimations of plume extent

may arise if only the hydraulic properties of the aquifer matrix are considered in numerical investigations of solute transport. The influence of discontinuous DFFs was not considered in this thesis and hence, would be a useful direction for future research. It also remains to be confirmed whether ‘back dispersion’ is a physical process, or a non-physical artefact of the advection-dispersion equation. The current research has contributed to the development of an analytical solution (Robinson et al., in prep), which has allowed for the numerical results obtained in the current study to be benchmarked against a mathematical solution to DFF effects on solute plumes that is far less reliant on the numerical strategies of the HydroGeoSphere control-volume finite-element code.

## References

- Abarca, E., Carrera, J., Sanchez-Villa, X., Dentz, M., 2007. Anisotropic dispersive Henry problem. *Adv. Water Resour.* 30(4), 913–926, doi: 10.1016/j.advwatres.2006.08.005.
- Al Ajmi, H., Hinderer, M., Rausch, R., Hornung, J., Bassis, A., Keller, M., Schüth, C., 2014. Matrix versus fracture permeability in a regional sandstone aquifer (Wajid sandstone, SW Saudi Arabia). *Grundwasser* 19(2), 151-157, doi: 10.1007/s00767-014-0258-4.
- Al-Niami, A. N. S., Rushton, K. R., 1977. Analysis of flow against dispersion in porous media. *J. Hydrol.* 33(1-2), 87-97, doi: 10.1016/0022-1694(77)90100-7.
- Allen, D. M., Abbey, D. G., Mackie, D. C., Luzitano, R. D., Cleary, M., 2002. Investigation of Potential Saltwater Intrusion Pathways in a Fractured Aquifer using an Integrated Geophysical, Geological and Geochemical Approach. *J. Environ. Eng. Geoph.* 7(1), 19-36, doi: 10.4133/JEEG7.1.19.
- Allen, D. M., Liteanu, E., Mackie, D. C., 2003. Geologic Controls on the Occurrence of Saltwater Intrusion in Heterogeneous and Fractured Island Aquifers, Southwestern British Columbia, Canada, paper presented at 2<sup>nd</sup> International Conference on Saltwater Intrusion in Coastal Aquifers – Monitoring, Modeling, and Management. Mérida, México.
- Antonelli, M., Aydin, A., 1994. Effect of faulting on fluid flow in porous sandstones: petrophysical properties. *AAPG Bull.* 78(3), 355–377.
- Arfib, B., de Marsily, G., Ganoulis, J., 2007. Locating the zone of saline intrusion in a coastal karst aquifer using springflow data. *Ground Water* 45(1), 28-35, doi: 10.1111/j.1745-6584.2006.00252.x.
- Bakalowicz, M., 2005. Karst groundwater: a challenge for new resources. *Hydrogeol. J.* 13(1), 148-160, doi: 10.1007/s10040-004-0402-9.
- Barcelona, M. J., Kim, M., Masciopinto, C., La Mantia, R., 2006. A Gypsum-Barrier Design to Stop Seawater Intrusion in a Fractured Aquifer at Salento (Southern Italy). In *Proceedings of 1<sup>st</sup> SWIM-SWICA Conference*, vol. 1, edited by G. Barrocu, pp. 263-272, Cagliari, Italy.
- Barenblatt, G. I., Zheltov, I. P., Kochina, I. N., 1960. Basic concepts in the theory of seepage of homogeneous liquids in fissured rock. *J. Appl. Math. Mech.* 24(5), 1286–1303, doi: 10.1016/0021-8928(60)90107-6.
- Barlow, P. M., 2003. Ground water in freshwater–saltwater environments of the Atlantic coast. *US Geol. Surv. Circ.* 1262.
- Barlow, P. M., Reichard, E. G., 2010. Saltwater intrusion in coastal regions of North America. *Hydrogeol. J.* 18(1), 247–260, doi: 10.1007/s10040-009-0514-3.

Barton, N., 1973. Review of a new shear-strength criterion for rock joints. *Eng. Geol.* 7(4), 287-332, doi: 10.1016/0013-7952(73)90013-6.

Bauer-Gottwein, P., Gondwe, B. R. N., Charvet, G., Marín, L. E., Rebolledo-Vieyra, M., Merddiz-Alonso, G., 2011. Review: The Yucatán Peninsula karst aquifer, Mexico. *Hydrogeol. J.* 19(3), 507-524, doi: 10.1007/s10040-010-0699-5.

Bear, J., Tsang, C-F., de Marsily, G., 1993. *Flow and Contaminant Transport in Fractured Rock*, first ed., Academic Press, Inc. California, U.S.A.

Becker, M. W., Shapiro, A. M., 2000. Tracer transport in fractured crystalline rock: Evidence of nondiffusive breakthrough tailing. *Water Resour. Res.* 36(7), 1677-1686, doi: 10.1029/2000WR900080.

Bense, V. F., Person, M. A., 2006. Faults as conduit-barrier systems to fluid flow in siliciclastic sedimentary aquifers. *Water Resour. Res.* 42(5), W05421, doi: 10.1029/2005WR004480.

Bense, V. F., Van den Berg, E. H., Van Balen, R. T., 2003. Deformation mechanisms and hydraulic properties of fault zones in unconsolidated sediments; the Roer Valley Rift System, The Netherlands. *Hydrogeol. J.* 11(3), 319-332, doi: 10.1007/s10040-003-0262-8.

Bense, V. F., Gleeson, T., Loveless, S. E., Bour, O., Scibek, J., 2013. Fault zone hydrogeology. *Earth-Sci. Rev.* 127, 171-192, doi: 10.1016/j.earscirev.2013.09.008.

Berkowitz, B., 2002. Characterizing flow and transport in fractured geological media: A review. *Adv. Water Resour.* 25(8-12), 861-884, doi: 10.1016/S0309-1708(02)00042-8.

Berkowitz, B., Scher, H., 1998. Theory of anomalous chemical transport in random fracture networks. *Phys. Rev. E.* 57(5), 5858-5869, doi: 10.1103/PhysRevE.57.5858.

Birkhölzer, J., Rubin, H., Daniels, H., Rouvé, G., 1993a. Contaminant advection and spreading in a fractured permeable formation: Part 1. Parametric evaluation and analytical solution. *J. Hydrol.* 144(1-4), 1-33, doi: 10.1016/0022-1694(93)90163-4.

Birkhölzer, J., Rubin, H., Daniels, H., Rouvé, G., 1993b. Contaminant advection and spreading in a fractured permeable formation: Part 2. Numerical simulation. *J. Hydrol.* 144(1-4), 35-58, doi: 10.1016/0022-1694(93)90164-5.

Bonacci, O., Roje-Bonacci, T., 1997. Sea water intrusion in coastal karst springs: example of Blaž Spring (Croatia). *Hydrolog. Sci. J.* 42(1), 89-100, doi: 10.1080/02626669709492008.

Celico, F., Petrella, E., Celico, P., 2006. Hydrogeological behaviour of some fault zones in a carbonate aquifer of Southern Italy: an experimentally based model. *Terra Nova* 18(5), doi: 10.1111/j.1365-3121.2006.00694.x.

Chang, C. M., Yeh, H. D., 2010. Spectral approach to seawater intrusion in heterogeneous coastal aquifers. *Hydrol. Earth Syst Sci.* 14(5), 719–727, doi: 10.5194/hess-14-719-2010.

Chrysikopoulos, C. V., Masciopinto, C., La Mantia, R., Manariotis, I. D., 2010. Removal of Biocolloids Suspended in Reclaimed Wastewater by Injection into a Fractured Aquifer Model. *Environ. Sci. Technol.* 44(3), 971-977, doi: 10.1021/es902754n.

Cirpka, O. A., de Barros, F. P. J., Chiogna, G., Rolle, M., Novak, W., 2011. Stochastic flux-related analysis of transverse mixing in two-dimensional heterogeneous porous media. *Water Resour. Res.* 47(6), W06515, doi: 10.1029/2010WR010279.

Croucher, A. E., O'Sullivan, M. J., 1995. The Henry problem for saltwater intrusion. *Water Resour. Res.* 31(7), 1809-1814, doi: 10.1029/95WR00431.

Custodio, E., Bruggeman, G. A (Eds.), 1987. Groundwater problems in coastal areas: a contribution to the International Hydrological Programme. Studies and reports in hydrology, vol. 45, UNESCO, Paris, France.

Dagan, G., Zeitoun, D. G., 1998. Free-surface flow toward a well and interface upconing in stratified aquifers of random conductivity. *Water Resour. Res.* 34(11), 3191–3196, doi: 10.1029/98WR02039.

Dokou, Z., Karatzas, G. P., 2012. Saltwater intrusion estimation in a karstified coastal system using density-dependent modelling and comparison with the sharp-interface approach. *Hydrolog. Sci. J.* 57(5), 985-999, doi: 10.1080/02626667.2012.690070.

Domenico, P. A., Schwartz, F. W., 1998. *Physical and Chemical Hydrogeology*, second ed., John Wiley and Sons, New York, U.S.A.

Elder, J. W., 1967. Transient convection in a porous medium. *J. Fluid Mech.* 27(3), 609-623, doi: 10.1017/S0022112067000576.

Fetter, C. W., 2001. *Applied Hydrogeology*, fourth ed., Prentice-Hall, New Jersey, U.S.A.

Frind, E. O., 1982. Simulation of long-term transient density-dependent transport in groundwater. *Adv. Water Resour.* 5(2), 73-88, doi: 10.1016/0309-1708(82)90049-5.

Gassiat, C., Gleeson, T., Lefebvre, R., McKenzie, J., 2013. Hydraulic fracturing in faulted sedimentary basins: Numerical simulation of potential contamination of

shallow aquifers over long time scales. *Water Resour. Res.* 49(12), 8310–8327, doi: 10.1002/2013WR014287.

Geiger, S., Cortis, A., Birkholzer, J. T., 2010. Upscaling solute transport in naturally fractured porous media with the continuous time random walk method. *Water Resour. Res.* 46(12), W12530, doi: 10.1029/2010WR009133.

Giudici, M., Margiotta, S., Mazzone, F., Negri, S., Vassena, C., 2012. Modelling hydrostratigraphy and groundwater flow of a fractured and karst aquifer in a Mediterranean basin (Salento peninsula, southeastern Italy). *Environ. Earth Sci.* 67(7), 1891-1907, doi: 10.1007/s12665-012-1631-1.

Graf, T., 2005. Modeling coupled thermohaline flow and reactive transport in discretely-fractured porous media. Ph.D. thesis, Fac. of Sci. and Eng. Uni. Laval, Québec City, Québec, Canada.

Graf, T., Simmons, C. T., 2009. Variable-density groundwater flow and solute transport in fractured rock: Applicability of the *Tang et al.* [1981] analytical solution. *Water Resour. Res.* 45(2), W02425, doi: 10.1029/2008WR007278.

Graf, T., Therrien, R., 2005. Variable-density groundwater flow and solute transport in porous media containing nonuniform discrete fractures. *Adv. Water Resour.* 28(12), 1351–1367, doi: 10.1016/j.advwatres.2005.04.011.

Graf, T., Therrien, R., 2007. Variable-density groundwater flow and solute transport in irregular 2D fracture networks. *Adv. Water Resour.* 30(3), 455–468, doi: 10.1016/j.advwatres.2006.05.003.

Graf, T., Therrien, R., 2008. A test case for the simulation of three-dimensional variable-density flow and solute transport in discretely-fractured porous media. *Adv. Water Resour.* 31(10), 1352-1363, doi: 10.1016/j.advwatres.2008.07.003.

Grisak, G. E., Pickens, J. F., 1980. Solute transport through fractured media: 1. The effect of matrix diffusion. *Water Resour. Res.* 16(4), 719-730, doi: 10.1029/WR016i004p00719.

Grisak, G. E., Pickens, J. F., 1981. An analytical solution for solute transport through fractured media with matrix diffusion. *J. Hydrol.* 52(1-2), 47-57, doi: 10.1016/0022-1694(81)90095-0.

Harrison, B., Sudicky, E. A., Cherry, J. A., 1992. Numerical analysis of solute migration through fractured clayey deposits into underlying aquifers. *Water Resour. Res.* 28(2), 515-526, doi: 10.1029/91WR02559.

Held, R., Attinger, S., Kinzelbach, W., 2005. Homogenization and effective parameters for the Henry problem in heterogeneous formations. *Water Resour. Res.* 41(11), W11420, doi: 10.1029/2004WR003674.

Henry, H. R., 1964. Effects of dispersion on salt encroachment in coastal aquifers, U.S. Geol. Surv. Water Supply Pap., 1613-C.

- Himmelsbach, T., Hötzl, H., Maloszewski, P., 1998. Solute transport processes in a highly permeable fault zone of Lindau fractured rock test site (Germany). *Ground Water* 36(5), 792-800, doi: 10.1111/j.1745-6584.1998.tb02197.x.
- Houseworth, J. E., Asahina, D., Birkholzer, J. T., 2013. An analytical model for solute transport through a water-saturated single fracture and permeable rock matrix. *Water Resour. Res.* 49(10), 6317-6338, doi: 10.1002/wrcr.20497.
- Hubbert, M. K., 1940. The theory of ground-water motion. *J. Geol.* 48(8) Part 1: 785-944.
- Johnson, R. L., Cherry, J. A., Pankow, J. F., 1989. Diffusive contaminant transport in natural clay: A field example and implications for clay-lined waste disposal sites. *Environ. Sci. Technol.* 23(3), 340-349, doi: 10.1021/es00180a012.
- Kerrou, J., Renard, P., 2010. A numerical analysis of dimensionality and heterogeneity effects on advective dispersive seawater intrusion processes. *Hydrogeol. J.* 18(1), 55–72, doi: 10.1007/s10040-009-0533-0.
- Kessler, J. H., Hunt, J. R., 1994. Dissolved and colloidal contaminant transport in a partially clogged fracture. *Water Resour. Res.* 30(4), 1195-1206, doi: 10.1029/93WR03555.
- Kinzelbach, W., 1986. Groundwater Modelling. An Introduction with Sample Programs in BASIC, in *Dev. Water Sci.*, vol. 25, p. 267, Elsevier, New York, U.S.A.
- Kitanidis, P. K., 1988. Prediction by the method of moments of transport in a heterogeneous formation. *J. Hydrol.* 102(1-4), 453-473, doi: 10.1016/0022-1694(88)90111-4.
- Konikow, L. F., 2011. The secret to successful solute-transport modeling. *Ground Water* 49(2), 144–159, doi: 10.1111/j.1745-6584.2010.00764.x.
- Krásný, J., Sharp, Jr, J. M., 2007. Hydrogeology of fractured rocks from particular fractures to regional approaches: State-of-the-art and future challenges, in *Groundwater in Fractured Rocks – IAH Selected Papers*, edited by J. Krásný and J.M. Sharp, Jr., pp. 1-30, Taylor and Francis Group, London, U.K.
- Kresic, N., 1997. *Quantitative solutions in hydrogeology and groundwater modeling*, CRC Press, Florida, U.S.A.
- Kumar, N., 1983. Unsteady flow against dispersion in finite porous media. *J. Hydrol.* 63(3-4), 345-358, doi: 10.1016/0022-1694(83)90050-1.
- Langevin, C. D., 2003. Simulation of submarine ground water discharge to a Marine Estuary: Biscayne Bay, Florida. *Ground Water* 41(6), 758-771, doi: 10.1111/j.1745-6584.2003.tb02417.x.

- Laubach, S. E., 2003. Practical approaches to identifying sealed and open fractures. *AAPG Bull.* 87(4), 561-579, doi: 10.1306/11060201106.
- Leve, G. W., 1983. Relation of concealed faults to water quality and the formation of solution features in the Floridan aquifer, northeastern Florida, U.S.A. *J. Hydrol.* 61(1-3), 251-264, doi: 10.1016/0022-1694(83)90252-4.
- Lim, J.-W., Lee, E., Moon, H. S., Lee, K.-K., 2013. Integrated investigation of seawater intrusion around oil storage caverns in a coastal fractured aquifer using hydrogeochemical and isotopic data. *J. Hydrol.* 486, 202-210, doi: 10.1016/j.jhydrol.2013.01.023.
- Liggett, J. E., Werner, A. D., Smerdon, B. D., Partington, D., Simmons, C. T., 2014. Fully integrated modeling of surface-subsurface solute transport and the effect of dispersion in tracer hydrograph separation. *Water Resour. Res.* 50(10), 7750-7765, doi: 10.1002/2013WR015040.
- Liu, G., Zheng, C., Gorelick, S. M., 2004. Limits of applicability of the advection-dispersion model in aquifers containing connected high-conductivity channels. *Water Resour. Res.* 40(8), W08308, doi: 10.1029/2003WR002735.
- Lu, C., Kitanidis, P. K., Luo, J., 2009. Effects of kinetic mass transfer and transient flow conditions on widening mixing zones in coastal aquifers. *Water Resour. Res.* 45(12), W12402, doi: 10.1029/2008WR007643.
- Lu, C., Chen, Y., Zhang, C., Luo, J., 2013. Steady-state freshwater-seawater mixing zone in stratified coastal aquifers. *J. Hydrol.* 505, 24-34, doi: 10.1016/j.jhydrol.2013.09.017.
- Mádl-Szőnyi, J., Tóth, Á., 2015. Basin-scale conceptual groundwater flow model for an unconfined and confined thick carbonate region. *Hydrogeol. J.* 23(7), 1359-1380, doi: 10.1007/s10040-015-1274-x.
- Marino, M. A., 1978. Flow against dispersion in nonadsorbing porous media. *J. Hydrol.* 37(1-2), 149-158, doi: 10.1016/0022-1694(78)90103.
- Masciopinto, C., 2006. Simulation of coastal groundwater remediation: the case of Nardò fractured aquifer in Southern Italy. *Environ. Modell. Software* 21(1), 85-97, doi: 10.1016/j.envsoft.2004.09.028.
- Masciopinto, C., La Mantia, R., Chrysikopoulos, C. V., 2008. Fate and transport of pathogens in a fractured aquifer in the Salento area, Italy. *Water Resour. Res.* 44(1), W01404, doi: 10.1029/2006WR005643.
- Neumann, S. P., 2005. Trends, prospects and challenges in quantifying flow and transport through fractured rocks. *Hydrogeol. J.* 13(1), 124-147, doi: 10.1007/s10040-004-0397-2.

- Odling, N. E., Roden, J. E., 1997. Contaminant transport in fractured rocks with significant matrix permeability, using natural fracture geometries. *J. Contam. Hydrol.* 27(3-4), 263–283, doi: 10.1016/S0169-7722(96)00096-4.
- Pankow, J. F., Johnson, R. L., Hewetson, J. P., Cherry, J. A., 1986. An evaluation of contaminant migration patterns at two waste disposal sites on fractured porous media in terms of the equivalent porous medium (EPM) model. *J. Contam. Hydrol.* 1(1-2), 65-76, doi: 10.1016/0169-7722(86)90007-0.
- Park, H.-Y., Jang, K., Ju, J. W., Yeo, I. W., 2012. Hydrogeological characterization of seawater intrusion in tidally-forced coastal fractured bedrock aquifer. *J. Hydrol.* 446-447, 77-89, doi: 10.1016/j.jhydrol.2012.04.033.
- Price, R. M., Top, Z., Happell, J. D., Swart, P. K., 2003. Use of tritium and helium to define groundwater flow conditions in Everglades National Park. *Water Resour. Res.* 39(9), 1267, doi: 10.1029/2002WR001929.
- Rasmussen, P., Sonnenborg, T. O., Goncear, G., Hinsby, K., 2013. Assessing impacts of climate change, sea level rise, and drainage canals on saltwater intrusion to coastal aquifer. *Hydrol. Earth Syst. Sc.* 17(1), 421-443, doi: 10.5194/hess-17-421-2013.
- Reeves, D. M., Benson, D. A., Meerschaert, M. M., 2008. Transport of conservative solutes in simulated fracture networks: 1. Synthetic data generation. *Water Resour. Res.* 44(5), W05404, doi: 10.1029/2007WR006069.
- Rubin, H., Buddemeier, R. W., 1996. Transverse dispersion of contaminants in fractured permeable formations. *J. Hydrol.* 176(1-4), 133-151, doi: 10.1016/0022-1694(95)02783-1.
- Rubin, H., Dveyrin, D., Birkhölzer, J., Rouvé, G., 1997. Advection and dispersion of contaminant in a permeable medium embedding fractures in which advection velocity is comparatively slow. *J. Hydrol.* 199(1-2), 135-162, doi: 10.1016/S0022-1694(96)03258-1.
- Rumer, Jr, R. R., Shiau, J. C., 1968. Salt water interface in a layered coastal aquifer. *Water Resour. Res.* 4(6), 1235-1247, doi: 10.1029/WR004i006p01235.
- Scanlon, B. R., Mace, R. E., Barrett, M. E., Smith, B., 2003. Can we simulate regional groundwater flow in a karst system using equivalent porous media models? Case study, Barton Springs Edwards aquifer, USA. *J. Hydrol.* 276(1–4), 137–158, doi: 10.1016/S0022-1694(03)00064-7.
- Sebben, M. L., Werner, A. D., Graf, T., 2015. Seawater intrusion in fractured coastal aquifers: A preliminary numerical investigation using a fractured Henry problem. *Adv. Water Resour.* 85, 93-108, doi: 10.1016/j.advwatres.2015.09.013.
- Sebben, M. L., Werner, A. D., 2016. A modelling investigation of solute transport in permeable porous media containing a discrete preferential flow feature. *Adv. Water Resour.* 94, 307-317, doi: 10.1016/j.advwatres.2016.05.022.

- Sebben, M. L., Werner, A. D., 2016b. On the effects of preferential or barrier flow features on solute plumes in permeable porous media. *Adv. Water Resour.* 98, 32-46, doi: 10.1016/j.advwatres.2016.10.011.
- Segol, G., Pinder, G. F., Gray, W. G., 1975. A Galerkin-finite element technique for calculating the transient position of the saltwater front. *Water Resour. Res.* 11(2), 343-347, doi: 10.1029/WR011i002p00343.
- Shikaze, S. G., Sudicky, E. A., Schwartz, F. W., 1998. Density-dependent solute transport in discretely-fractured geologic media: is prediction possible? *J. Contam. Hydrol.* 34(3), 273-291, doi: 10.1016/S0169-7722(98)00080-1.
- Simpson, M. J., Clement, T. P., 2003. Theoretical analysis of the worthiness of Henry and Elder problems as benchmarks of density-dependent groundwater flow models. *Adv. Water Resour.* 26(1), 17-31, doi: 10.1016/S0309-1708(02)00085-4.
- Simpson, M. J., Clement, T. P., 2004. Improving the worthiness of the Henry problem as a benchmark for density-dependent groundwater flow models. *Water Resour. Res.* 40(1), W01504, doi: 10.1029/2003WR002199.
- Singhal, B. B. S., Gupta, R. P., 2010. *Applied Hydrogeology of Fractured Rocks*, second ed., Springer, The Netherlands.
- Smith, L., Schwartz, F. W., 1984. An analysis of the influence of fracture geometry on mass transport in fractured media. *Water Resour. Res.* 20(9), 1241-1252, doi: 10.1029/WR020i009p01241.
- Sonnenborg, T. O., Butts, M. B., Jensen, K. H., 1999. Aqueous flow and transport in analog systems of fractures embedded in permeable matrix. *Water Resour. Res.* 35(3), 719-729, doi: 10.1029/1998WR900099.
- Spechler, R. M., 1994. Saltwater intrusion and quality of water in the Floridan aquifer system, northeastern Florida, U.S. *Geol. Surv. Water-Resour. Invest. Rep.* 92-4174.
- Sudicky, E. A., 1990. The Laplace Transform Galerkin technique for efficient time-continuous solution of solute transport in double-porosity media. *Geoderma* 46(1-3), 209-232, doi: 10.1016/0016-7061(90)90016-3.
- Sudicky, E. A., Frind, E. O., 1982. Contaminant transport in fractured porous media: Analytical solutions for a system of parallel fractures. *Water Resour. Res.* 18(6), 1634-1642, doi: 10.1029/WR018i006p01634.
- Tang, D. H., Frind, E. O., Sudicky, E. A., 1981. Contaminant transport in fractured porous media: Analytical solution for a single fracture. *Water Resour. Res.* 17(3), 555-564, doi: 10.1029/WR017i003p00555.

- Therrien, R., Sudicky, E. A., 1996. Three-dimensional analysis of variably-saturated flow and solute transport in discretely-fractured porous media. *J. Contam. Hydrol.* 23(1-2), 1-44, doi: 10.1016/0169-7722(95)00088-7.
- Therrien, R., McLaren, R. G., Sudicky, E. A., Panday, S. M. 2010. *HydroGeoSphere – A Three-dimensional Numerical Model Describing Fully-Integrated Subsurface and Surface Flow and Solute Transport*. Groundwater Simul. Group, Univ. of Waterloo, Waterloo, Ont., Canada.
- Thoma, S. G., Gallegos, D. P., Smith, D. M., 1992. Impact of fracture coatings on fracture/matrix flow interactions in unsaturated, porous media. *Water Resour. Res.* 28(5), 1357-1367, doi: 10.1029/92WR00167.
- Vujević, K., Graf, T., Simmons, C. T., Werner, A. D., 2014. Impact of fracture network geometry on free convective flow patterns. *Adv. Water Resour.* 71, 65-80, doi: 10.1016/j.advwatres.2014.06.001.
- Weatherill, D., Graf, T., Simmons, C. T., Cook, P. G., Therrien, R., Reynolds, D. A., 2008. Discretizing the fracture-matrix interface to simulate solute transport. *Ground Water* 46(4), 606-615, doi: 10.1111/j.1745-6584.2007.00430.x.
- Webb, J. A., Grimes, K. G., Lewis, I. D., 2010. Volcanogenic origin of cenotes near Mt Gambier, southeastern Australia. *Geomorphology* 119(1-2), 23-35, doi: 10.1016/j.geomorph.2010.02.015.
- Werner, A. D., Bakker, M., Post, V. E. A., Vandenbohede, A., Lu, C., Ataie-Ashtiani, B., Simmons, C. T., Barry, D. A., 2013. Seawater intrusion processes, investigation and management: Recent advances and future challenges. *Adv. Water Resour.* 51, 3-26, doi: 10.1016/j.advwatres.2012.03.004.
- Werth, C. J., Cirpka, O. A., Grathwohl, P., 2006. Enhanced mixing and reaction through flow focusing in heterogeneous porous media. *Water Resour. Res.* 42(12), W12414, doi: 10.1029/2005WR004511.
- Willmann, M., Lanyon, G. W., Marschall, P., Kinzelbach, W., 2013. A new stochastic particle-tracking approach for fractured sedimentary formations. *Water Resour. Res.* 49(1), 352-359, doi: 10.1029/2012WR012191.
- Wilson, J. L., Miller, P. J., 1978. Two-dimensional plume in uniform groundwater flow. *J. Hydr. Eng. Div-ASCE* 104(4), 503-514.
- Yang, J., Graf, T., Herold, M., Ptak, T., 2013. Modelling the effects of tides and storm surges on coastal aquifers using a coupled surface-subsurface approach. *J. Contam. Hydrol.* 149, 61-75, doi: 10.1016/j.jconhyd.2013.03.002.
- Zhang, W-J., Qiu, Q-W., 2010. Analysis on contaminant migration through vertical barrier walls in a landfill in China. *Environ. Earth Sci.* 61(4), 847-852, doi: 10.1007/s12665-009-0399-4.

Zhou, Q., Liu, H.-H., Molz, F. J., Zhang, Y., Bodvarsson, G. S., 2007. Field-scale effective matrix diffusion coefficient for fractured rock: Results from literature survey. *J. Contam. Hydrol.* 93(1-4), 161–187, doi:10.1016/j.jconhyd.2007.02.002.